Molecular MRI and PET methods for detection of transplanted stem cells and cancer

By

Christina L. Brunnquell

A dissertation submitted in partial fulfillment of

the requirements for the degree of

Doctor of Philosophy

(Medical Physics)

at the

UNIVERSITY OF WISCONSIN-MADISON

2016

Date of final oral examination: 5/3/2016

The dissertation is approved by the following members of the Final Oral Committee:
Weibo Cai, Professor, Medical Physics
Marina Emborg, Professor, Medical Physics
Edward Jackson, Professor, Medical Physics
Mary Elizabeth Meyerand, Professor, Medical Physics
Masatoshi Suzuki, Professor, Comparative Biosciences

Dedicated to my family

“The pursuit of truth and beauty is a sphere of activity in which we are permitted to remain children all our lives.” –Albert Einstein

Acknowledgements

Countless mentors and friends have made this work possible. I feel eternally grateful to have been shaped as a scientist by my primary advisors, Dr. Beth Meyerand and Dr. Masatoshi Suzuki. Their dedication, encouragement, support, thoughtful feedback, and trust helped me grow in so many ways and made my experience in graduate school an incredibly rewarding one.

I would also like to thank my committee members Dr. Weibo Cai, Dr. Marina Emborg, and Dr. Ed Jackson for their advice, time, and dedication – not just in overseeing my research progress, but also in providing helpful feedback, support, and collaborative opportunities to help me advance my career and explore my interests. It was an honor to work with each of you.

I would not be where I am without the mentoring of Dr. Ksenija Bernau. She dedicated incalculable time, energy, patience, and kindness as I embarked on this research path. She has been a wonderful mentor and role model, has become a great friend, and I am truly grateful.

Much of my work has been collaborative, and I have been incredibly lucky to work with and learn from a variety of fantastic researchers here at the UW-Madison. Although many have contributed, I would like to explicitly thank Dr. Jerry Nickles, Dr. Jamey Weichert, Dr. Cheng Guan Koay, Stephen Graves, Reinier Hernandez, Dr. Samuel Hurley, Ivy Smit-Oistad, Ray Zhang, Dr. Jonathan Van Dyke, Justin Jeffery, and Beth Rauch. They have provided time, support, and invaluable expertise to this research.

Abstract

Molecular MRI and PET methods for detection of transplanted stem cells and cancer

Christina Lewis Brunnquell, under the supervision of M. Elizabeth Meyerand, Ph.D., and Masatoshi Suzuki, Ph.D., D.V.M.

Stem cell therapies hold great potential for treatment of neurodegenerative diseases. In this setting, the inability to monitor grafted cell dynamics in the central nervous system limits understanding of cell fates underlying therapeutic response, making therapy design and optimization significantly more challenging. To address this limitation, we aim to design, evaluate, and develop new imaging approaches for detection of human stem cells *in vivo*. Over-expression of the manganese transporter protein DMT1 in human neural progenitor cells (hNPC) significantly increases intracellular accumulation of the T_1-shortening agent Mn^{2+} and the novel positron emitter $^{52}Mn^{2+}$. This work addresses three specific hypotheses: (1) hNPC over-expressing DMT1 are suitable for *in vivo* cellular imaging, (2) *in vivo* ^{52}Mn PET and manganese-enhanced MRI are applicable for cell tracking in the rat brain, and (3) Mn-based imaging can be used to detect grafted stem cells *in vivo*. In addition, we apply the techniques and knowledge developed for stem cell tracking to the characterization and initial *in vivo* testing of a novel cancer-targeted MRI contrast agent, Gd-DO3A-404. The results of this work establish both the potential and limitations of this approach for *in vivo* cell tracking. In particular, we find that hNPC transiently over-expressing DMT1 are

most suitable for *in vivo* detection following transplantation. Additionally, the methods for quantitative MRI, ^{52}Mn PET, and cancer-targeted contrast-enhanced MRI developed in this work contribute more broadly to the fields of molecular MRI and multi-modality imaging.

Table of Contents

List of figures

List of tables

Chapter 1: Introduction

1.1 Motivation

Despite the prevalence and devastating consequences of neurodegenerative diseases, no available treatments fully halt or reverse disease progression. Stem cell therapies have been intensely investigated as novel treatment approaches with potential benefits for diseases such as amyotrophic lateral sclerosis (ALS), Parkinson's disease, and Huntington's disease. In these settings, transplanted cells may replace missing cell types, provide supportive growth factors, or modulate the immune system [1]. In current preclinical research and ongoing clinical trials, stem cell graft survival is essential to maximize therapeutic efficacy and accurately interpret functional and clinical observations [2]. The inability to monitor the survival and migration of grafted cells in the central nervous system (CNS) results in limited understanding of the *in vivo* cell dynamics underlying a subject's clinical response, making therapy design and optimization significantly more challenging. The lack of an adequate *in vivo* transplanted cell imaging approach is therefore a major roadblock to rapid therapy development [3, 4]. The objective of the studies described in Chapters 3-6 is to design, evaluate, and develop new imaging approaches for a method for imaging human stem cells *in vivo*.

An additional aim of the work described herein is to apply the technology, imaging techniques, and knowledge developed from stem cell imaging work to cancer imaging. Early diagnosis and targeted treatment of a variety of solid tumor types can improve disease-free survival and patient outcomes. Cancer screening

and treatment would benefit greatly from broad-spectrum tumor-specific theranostic agents for sensitive detection and targeted treatment. In particular, the lack of a clinically available cancer-targeted MR contrast agent makes high-resolution tumor detection and delineation challenging and subject to non-specific uptake effects. The objective of the study described in Chapter 7 is to characterize the relaxation characteristics and cancer-targeting capabilities of a novel MR contrast, Gd-DO3A-404, as part of a suite of tumor-specific multi-modal imaging and therapy agents.

1.2 General hypotheses

The objective of Chapters 3-6 of this work is to develop an imaging approach to monitor engrafted human neural progenitor cells (hNPC) in the rat CNS. To reach this objective, the cells are labeled prior to transplantation by inducing both transient and stable over-expression of the divalent metal transporter 1 (DMT1), a cell surface transporter protein for manganese (Mn) and other divalent metals. Next, protocols for manganese-enhanced magnetic resonance imaging (MEMRI) and manganese-based positron emission tomography (^{52}Mn PET) specifically designed for cell detection in the rat brain are tested and optimized for this application. Using these protocols, the ability of MEMRI and ^{52}Mn PET to detect the location and survival of grafted hNPC after transplantation into the striatum of wild-type rats is tested. Our overarching hypothesis is that viable hNPC over-expressing DMT1 will take up higher levels of Mn^{2+} and ^{52}Mn than controls and thus be selectively enhanced on MRI and PET images for *in vivo* detection. In order to test this general hypothesis, three

specific hypotheses are tested herein: (1) hNPC over-expressing DMT1 are suitable for *in vivo* cellular imaging, (2) *in vivo* ^{52}Mn PET and MEMRI are applicable for cell tracking in the rat brain, and (3) Mn-based imaging can be used to detect grafted stem cell location and survival *in vivo*.

The objective of Chapter 7 of this work is to characterize a novel MR contrast agent, Gd-DO3A-404. This agent has been synthesized as part of a library of alkylphosphocholine analogs (APCs) for multi-modal imaging and radionuclide therapy. In previous work, ^{124}I-labeled APCs have been shown to specifically target a variety of human and rodent cancer cell lines, and successful PET imaging of several tumor types and metastases has been performed in human subjects [5]. Additionally, APC analogs labeled with ^{131}I for therapy and optical agents were successfully delivered to flank and orthotopic xenografts in rodents [5]. Due to the analogous structure of Gd-DO3A-404 to other APC analogs, along with high tumor specificity and contrast agent uptake levels, we expect to observe similar broad-spectrum tumor specificity of this novel MR agent. Our hypothesis in testing Gd-DO3A-404 is that it will show favorable relaxation characteristics *in vitro* along with sustained, tumor-specific uptake in rodent xenografts of multiple human cancer cell lines.

1.3 Chapters summary

Chapter 2 provides a background to the work described herein. Previously published studies relating to this work are reviewed and essential points are summarized. The topics covered include clinical motivation, optimal design of cellular imaging approaches, previously developed cellular imaging approaches

(largely focused on stem cells), roles of the human DMT1 protein, manganese-based PET and MRI, and the objectives of this work.

Chapter 3 describes a proof-of-concept study laying the foundation for this imaging technique. In it, hNPC are transfected to transiently over-express DMT1, and the suitability of this imaging technique is tested with *in vitro* cell dynamics assays, *in vitro* imaging, and *in vivo* imaging of grafted cells.

In chapter 4, MEMRI and ^{52}Mn PET protocols are developed for the specific application of imaging cells transplanted into the rat striatum. Contrast agent doses, contrast delivery methods, and imaging time points are tested to determine the optimal experimental approach in this specific setting.

In chapter 5, a data-driven method to select optimal MR imaging parameters is described and evaluated. This approach can be generalized to select an optimal approach to quantitative T_1 mapping in any setting, and in this context is used to maximize reproducibility, accuracy, and precision of *in vivo* MEMRI for cell detection in the rat brain.

In chapter 6, the knowledge gained and protocols developed in the experiments described in chapters 3-5 are combined to test a method for long-term tracking of transplanted stem cells. A line of hNPC stably over-expressing DMT1 is established ($hNPC^{DMT1}$) and the capabilities and limitations of *in vitro* and *in vivo* Mn-based imaging of $hNPC^{DMT1}$ are tested.

In chapter 7, we further apply the knowledge and tools developed in this work to characterize the novel MRI contrast agent Gd-DO3A-404. In it, we quantitatively evaluate the relaxation properties of the agent and test whether

sustained, tumor-specific uptake of Gd-DO3A-404 is observed *in vivo* in multiple rodent xenografts of human tumor cell lines.

Chapter 8 provides a summary of this dissertation and perspectives on the future of this work, particularly as it relates other ongoing efforts in the field.

Chapter 2: Background

2.1 Clinical Motivation

2.1.1 Stem cell therapy in neurodegenerative disease

The growing field of stem cell therapy is moving toward clinical trials in a variety of applications, particularly cardiac and neurological diseases [6-8]. In the context of neurodegenerative and neurological diseases, these trials have been prompted by preclinical evidence of the efficacy of stem cells to functionally replace missing and diseased cell types such as neurons and astrocytes [9-11]. Furthermore, they have been shown to exert positive effects as supportive cells to play key roles in the health of the cells impacted by disease [1, 12-15].

Human neural progenitor cells (hNPC) are of particular interest for cell therapy in neurodegenerative diseases such as Parkinson's disease (PD), Huntington's disease (HD), and amyotrophic lateral sclerosis (ALS). These cells can be isolated and grown long-term *in vitro*, have the potency to differentiate into neuronal and glial sub-types, and can be modified to stably express neuroprotective growth/trophic factors [16, 17]. In these ways, hNPCs can play a variety of roles after transplantation and may be able to respond to the diseased microenvironment in a patient-specific manner. For example, grafted hNPCs have been shown to migrate toward lesions [18, 19], replace cells [9], and provide essential support for diseased cell types [13]. Human NPCs have previously been shown to exert therapeutic effects in preclinical models of a variety of neurodegenerative and neurological diseases [12, 13, 18, 20]. In

several current clinical trials, the safety and efficacy of intraspinal hNPC transplantation is under investigation for the treatment of ALS [7, 8].

2.1.2 Stem cell imaging

In recent reports of first-in-human stem cell therapy trials for ALS, variable impacts on disease severity and progression have been observed between patients [7, 8]. This variability could be due to a variety of factors, including patient age, disease state, therapeutic design, and cell survival. To account for the observed results, it is essential to understand whether the transplanted cells survive and integrate. Entire publications have been devoted to analysis of the survival of cell transplants in humans, using histology to detect transplanted cells [2]. Evidently, knowledge of transplanted cell fates is essential for meaningful and accurate evaluation of these therapeutic approaches. Due to the invasive nature of histology for cell detection, timely *in vivo* analysis of cell survival, and accordingly treatment adjustment, is not currently possible. In some cell therapy clinical trials, *in vivo* imaging of the anatomy of interest [6, 8] and of labeled cells [21, 22] has been incorporated, but these imaging approaches have yet been unable to address whether transplanted cells survive long-term following transplantation.

A similar challenge is faced in preclinical stem cell therapy development. In order to thoroughly understand the longitudinal dynamics of transplanted cells over the course of disease, multiple study subject groups must be experimented on and sacrificed at various time points [23]. This increases research costs and the number of animals used for preclinical therapy development. The preclinical

study and clinical translation of cell therapies has clearly highlighted the need for an *in vivo* imaging tool to assess the location, survival, and dynamics of transplanted cells non-invasively and longitudinally.

2.1.3 Manganese-based dual-modality imaging

Mn^{2+} is a T_1-weighted signal-enhancing MRI contrast agent with a variety of potential applications. It has been studied and applied in preclinical animal models and human subjects for imaging liver disease, cancer, cardiac viability, and brain function and structure [24-27]. To avoid the toxic effects of this metal when using the large doses required for MR signal enhancement, only the chelated form Mn-DPDP (Magnafodipir, Teslascan®) and an oral $MnCl_2$ agent (LumenHance®) have been approved for use in human patients [28]. Because unchelated Mn^{2+} can be transported via calcium (Ca^{2+}) channels, uptake and resulting T_1 enhancement can indicate function and highlight structure in the heart and brain. Therefore, it has been applied in a variety of preclinical functional imaging studies, primarily in rodents [29-31]. Mn^{2+} enhancement in the myocardium reflects viability, while uptake in the brain can reflect functional activation, connected neuronal tracts, or can be used for general tissue enhancement and cytoarchitecture visualization [30, 32].

Recently, the positron-emitting isotope ^{52}Mn ($t_{1/2}$ = 5.59 days) has been produced for PET imaging by several groups, including our own [33-38]. Two factors have played a role in recent development of ^{52}Mn as a PET contrast agent: First, the general interest in and investigation of longer-lived radiometals for antibody-based PET imaging [39, 40], and second, the development of

simultaneous PET/MRI systems [41], with $^{52}Mn^{2+}$ having potential as a dual-modality signal-enhancing contrast agent. Because PET imaging typically requires tracer doses, the availability of ^{52}Mn could facilitate the clinical investigation and application of Mn^{2+}-based imaging of function and viability that have been developed in preclinical models with manganese-enhanced MRI (MEMRI). In the context of stem cell imaging, Mn^{2+} has been shown to be a useful MRI contrast agent for detecting cells and their functional effects [27, 42-44]. The investigation of ^{52}Mn for dual-modality Mn-based imaging of transplanted cells could further strengthen this technology and expand its potential applications.

2.1.4 Targeted MRI for cancer theranostics

Along with applications in stem cell imaging and neurodegenerative disease, molecular imaging with MRI is of great interest for diagnosis and staging of cancer. MRI is often used for early tumor detection, surgical planning, and monitoring of therapy response or tumor progression. MRI is uniquely applicable in imaging soft tissue lesions, particularly in the brain, where lesions are more challenging to detect with other clinical modalities such as computed tomography and ultrasound. Dynamic contrast-enhanced MRI is performed with T_1-shortening Gd-based imaging agents, and is commonly applied to visualize lesions and can be used to derive quantitative biomarkers [45]. However, tumor uptake of most Gd^{3+}-based MR contrast agents is a result of the enhanced permeability and retention (EPR) effect, reflective of vascular permeability, and is not specific to molecular signatures of progressive cancer [46].

More commonly, PET and single photon emission computed tomography (SPECT) are used to probe molecular characteristics in cancer imaging. In these modalities, uptake and binding of radiolabeled biologically active molecules can indicate epigenetic, proteomic, and physiological changes [47]. Molecular MRI of cancer is more challenging due to reduced sensitivity, which leads to challenges in safely delivering sufficient concentrations of MR contrast agents. Nevertheless, in recent years researchers have worked to develop novel approaches to contrast agent chemistry for targeted MRI of cancer, mostly seeking to address the challenges of high contrast agent dose required for *in vivo* detectability [48-51]. None of these approaches have yet withstood the challenges of translation and FDA approval to make their way into clinical practice.

A safe and tumor-specific targeted MR contrast agent could be incredibly valuable for clinical oncology, providing the advantages of the spatial resolution and soft tissue contrast of MRI with molecular information typically not achievable with this modality. In addition, the agent we characterize in this work, Gd-DO3A-404, is one of a library of tumor-targeting molecules that can labeled with positron emitters, gamma emitters, beta emitters, and optical probes for both imaging and radionuclide therapy [5]. Therefore, the confirmation of the tumor-targeting potential of this agent could also contribute to preclinical development of simultaneous PET/MR imaging applications and cancer theranostics.

2.2 Stem Cell Imaging Techniques

2.2.1 Ideal characteristics of stem cell imaging techniques

The ideal stem cell imaging technique would have a variety of characteristics relating to the effect on cells, the label type, and the imaging modality used. At this point in the development of cell tracking techniques, it is rare to have all these characteristics met simultaneously. Nevertheless, they must be carefully considered in the design and application of a stem cell tracking method.

The first important characteristic of the ideal cell tracking approach is that the labeling and imaging of cells would not perturb cell dynamics or reduce the efficacy of the stem cell therapy. Specifically, it would not influence cell viability, motility, or output of supportive factors. Furthermore, it would not affect the differentiation or proliferation of transplanted cells. Additionally, any contrast agent introduced for imaging, whether systemically delivered or used to label the cells prior to transplantation, would not negatively affect the cells, the surrounding microenvironment, the diseased tissues, or the organism as a whole. A potential exception could be made if the cell tracking method does indeed affect cell dynamics but this effect is shown to positively impact the efficacy of therapy in a safe manner.

The second characteristic of the ideal cellular imaging technique is that it could provide functional information regarding the cells. In almost all recent studies proposing or developing cellular imaging approaches, the technique meets the baseline requirement of being useful for detecting cell location.

However, the ability to measure migration and death/survival is also essential in order to evaluate cell state with *in vivo* imaging. Finally, a non-essential but interesting goal that some researchers are pursuing is to develop cell imaging techniques that can be used to monitor gene expression [52]. Depending on the design of the approach, this method could be used to reflect proliferation, differentiation, tumor formation, or a variety of other functional measures.

Third, the ideal imaging technique would use clinically available imaging modalities and labeling contrast agents that are applicable in humans and could fit efficiently into clinical workflow. For example, the use of a modality with which the patient might typically be monitored post-surgery, such as MRI to observe tumor progression or anatomical effects of surgery, would be a great strength. More specifically, the ideal imaging modality or modalities would provide high spatial resolution, soft tissue contrast, and sensitivity along with low cost and the potential to provide functional information. Rarely are all of these met by a single imaging modality (see section 2.2.3). Furthermore, to fit into clinical workflow, the ideal process of labeling cells prior to transplantation would be relatively straightforward, scalable, and clinically feasible.

2.2.2 Labeling techniques

There are two primary approaches to labeling cells that are often used in cell tracking techniques: direct labeling and reporter genes [53]. Direct labels typically involve incubating the cells of interest with an imaging contrast agent that is readily internalized by cells prior to cell transplantation. Reporter genes are genes whose product(s) (often transporters, receptors, enzymes, or storage

proteins) interact with an endogenous or systemically delivered contrast agent. The expression or over-expression of a reporter gene is typically induced prior to transplantation, and then the gene product interacts with a contrast agent *in vivo* to provide cell-specific contrast.

The direct labeling approach for cell tracking is relatively straightforward, clinically applicable, and typically exerts minimal effects on cell dynamics [21, 54]. Some direct label approaches use probes that are already approved for clinical use in other applications [55]. Other direct label approaches incorporate more advanced technologies such as contrast sources for multi-modality imaging [56, 57]. However, the potential for long-term cell tracking with direct labels can be compromised by several factors. If cells proliferate, the label can be diluted among cell progeny, reducing the image contrast associated with each individual cell. If the cells are tagged with a radiolabeled molecule, radioactive decay limits the duration of time after transplantation during which cells can be detected [58, 59]. However, the recent production of longer-lived isotopes has extended this time frame to at least a week [60, 61]. Furthermore, direct labels could leave the cell and be taken up by microglia or macrophages following transplantation, leading to non-specific contrast and false positives in cell detection efforts [62]. Last, most direct labels are not capable of indicating cell state, particularly related to survival [63, 64]. For these reasons, direct labels are better suited for short-term studies to investigate the initial distribution of cells [53]. However, their low cost, ease of use, and safety make them quite applicable in the short-term clinically.

Reporter genes present an alternative approach to stem cell tracking that can offer greater depth of functional information regarding cell survival and differentiation [19, 65]. Cells can be engineered to stably over-express reporter genes, making longitudinal cell monitoring more feasible and meaningful [19, 66]. Although reporter gene silencing can cause false negatives, false positives are unlikely to occur [53]. In the case of cell death, reduced activity of the reporter gene product of that cell (whether it be a transporter, enzyme, receptor, or storage protein) typically, but not always, results in a reduction of reporter gene-associated image contrast accumulation [19]. Reporters also have great functional imaging potential because their expression can be engineered for specific cell states [52, 65], or inducible systems can be designed [67]. However, because they involve genetic manipulation of cells prior to transplantation, there are more significant regulatory hurdles associated with incorporating reporter gene-based imaging methods into human studies [53]. To maximize the potential of regulatory approval, reporter genes that are endogenous, ubiquitous human genes are typically the best candidates [53, 68]. The use of more advanced genetic manipulation tools, such as CRISPR/Cas9, for engineering of cells can also increase the safety of reporter genes by reducing chances of insertional mutagenesis [69].

2.2.3 Imaging modalities

There are a variety of pre-clinical and clinical imaging modalities that have been used to detect transplanted cells. These include well-established clinical modalities such as ultrasound, computed tomography, single-photon emission

computed tomography (SPECT), PET, and MRI. They also include modalities that are used more often in a preclinical setting, such as fluorescence, bioluminescence, photo-acoustic imaging, and magnetic particle imaging. Each of these modalities has strengths and weaknesses in terms of spatial resolution, soft tissue contrast, limits of contrast detectability, cost, depth penetration, clinical applicability, sensitivity, and ability to provide functional information. These characteristics are thoroughly described and approximately quantified in **Table 2.1**. Of course, given the recent translation of cell therapies into clinical trials, it would be most impactful to develop a technique that can be applied in humans. Furthermore, if developing a dual-modality cell imaging technique, selecting modalities with complementary strengths could maximize the flexibility and potential for utility of the designed technique.

Table 2.1: Comparison of imaging techniques for cell therapies. Reproduced with permission from Nguyen *et al.*, Cell Stem Cell 2014 [68].

Imaging Modality	Spatial Resolution	Acquisition Time	Detection Limit: Cells	Labeling Strategy	Advantages	Disadvantages
Bioluminescence imaging (BLI) (preclinical only)	5–20 mm depending on depth of signal	seconds	$\sim 10^3$	reporter gene	cheap, simple, high throughput	small animals only, low resolution, only 2D images
Fluorescence tomography (FMT) (preclinical only)	2–3 mm	seconds to minutes	$\sim 10^6$	reporter gene, fluorescent dye	cheap, simple	low resolution, cells need to be close to surface
Ultrasound (US) (preclinical and clinical)	150 μm; –2 mm depending on depth	seconds to minutes	not well characterized	reporter gene, antibody with microbubble	cheap, relatively simple	limited 3D capabilities, low signal to noise ratio
Single-photon emission computed tomography (SPECT) (preclinical and *clinical*)	1–2 mm; *8–12 mm*	minutes	$\sim 10^5$	reporter gene, incubation with radiotracer	3D imaging	anatomic reference required, radioactive tracer required
Positron emission tomography (PET) (preclinical and *clinical*)	~1 mm; *4–6 mm*	seconds to minutes	$\sim 10^4$	reporter gene, incubation with radiotracer	3D imaging, high sensitivity	anatomic reference required, radioactive tracer required
Magnetic resonance tomography (MRI) (preclinical and *clinical*)	25–500 μm; *0.5–5 mm*	minutes to hours	$\sim 10^4$	internalization or surface labeling with nanoparticles or specific ions	3D imaging, good soft tissue contrast, no radiation, high resolution	very expensive, complicated
Computed tomography (CT) (preclinical and *clinical*)	<50 μm; *<1 mm*	seconds to minutes	not well characterized	internalization or surface labeling with nanoparticles	3D imaging, relatively cheap, high resolution	uses ionizing radiation

Fields in italics indicate parameters specific to clinical systems if they are different from preclinical systems.

2.3 Current Stem Cell Imaging Approaches

2.3.1 Direct labeling approaches

In recent years, a variety of *in vivo* cell tracking methods have been developed and applied in animals and humans. The majority of these methods have used direct labeling of cells. Although direct labeling approaches have been investigated and developed for almost all available clinical imaging modalities [70-72], the majority of these efforts have focused on MRI- and PET-based cell tracking due to their superior soft tissue contrast and sensitivity, respectively.

One of the most common labels employed is superparamagentic iron oxide (SPIO) nanoparticles for negative T_2* contrast with MRI [22, 55]. These nanoparticles provide striking signal dropout in the vicinity of labeled cells, and the use of MRI provides high spatial resolution and soft tissue contrast for clear anatomical context. However, due to the widespread use of this approach, it has been carefully scrutinized regarding the potential weaknesses of direct labeling approaches. Researchers have observed false positives due to extracellular contrast agent, cell death, and non-specific endogenous iron deposition [62-64, 73]. These results suggest that although SPIO-based cell tracking is useful for initial cell localization following transplantation, it is unreliable for assessing long-term cell location and survival. However, the clinical applicability of SPIO due to its approval for other applications has led to it being one of the first cell imaging techniques applied in humans [22, 54]. Signal-enhancing MRI contrast agents, including manganese (Mn^{2+}) and ^{19}F, have also been investigated as direct labels for cell tracking [44, 74]. These methods tend to suffer from a relatively

small amount of signal and/or contrast with respect to background tissue [74, 75]. However, with a dedicated surface coil and superficial cell transplantation, successful detection of ^{19}F-labeled dendritic cells has been demonstrated in human patients [21].

Several radiolabelled molecules, most notably ^{111}In-oxine for SPECT and ^{18}F-fluorodeoxyglucose (FDG) for PET, are readily taken up in a variety of cell types *in vitro*. These approaches have been shown to be useful to sensitively assess initial biodistribution of transplanted or systemically delivered cells [58, 59, 76]. Recently, longer-lived radioisotopes, such as ^{89}Zr for PET ($t_{1/2}$ = 78.4 hr), have been produced and investigated for cell tracking. Direct labeling of cells with ^{89}Zr-labeled molecules has been shown to extend the period of time over which cells can be tracked following transplantation compared to other PET and SPECT-based methods [60, 61, 77]. However, reliable detection of cells beyond 7 days has not been shown, indicating that this approach remains unfeasible for long-term assessment of cell location and survival.

2.3.2 Reporter gene-based approaches

To increase long-term imaging capabilities and provide greater functional information in cell tracking, a variety of reporter genes have been proposed and investigated for this purpose. These reporter genes interact with contrast-providing agents and molecules to make cells detectable with respect to background tissue on a variety of preclinical and clinical imaging modalities. The most common types of reporter genes are enzymes, transporters, and cell surface receptors [68].

In the field of optical imaging, firefly luciferase (fLuc) for bioluminescence imaging (BLI) has been extensively studied and has been shown to clearly reflect the location and survival of transplanted cells over an extended period of several months [19, 78]. Due to this clear association between BLI signal presence and gene expression, this reporter has been used to detect the expression of specific genes by putting the fLuc gene under a promoter for another gene of interest [52, 65, 79]. Due to these capabilities and characteristics, BLI is highly useful for preclinical therapy development. However, is has relatively poor resolution, lacks tomographic anatomical information, and is not widely applicable in humans due to depth penetration and contrast agent safety issues. Using another optical imaging modality, several groups have applied fluorescent proteins in reporter gene-based cell tracking [80-82]. However, due to high background signal in fluorescence imaging and the challenge of detecting cells at depth, these fluorescent reporters typically serve as a supplement to a reporter gene for another modality and are used for *ex vivo* confirmation of cell location with histology.

In the effort to develop a reporter gene platform for a clinical imaging modality, a variety of MRI reporter genes have also been studied for cell tracking. Several of these reporters, including ferritin, the transferrin receptor, MagA, and Timd2, are designed to increase iron accumulation in the cells of interest, causing accelerated T2* relaxation and corresponding hypointense signal on T2*-weighted MR images. Most researchers studying these types of reporters have had initial success with detecting cells after transplantation and, in some

cases, over an extended period of several months [83-87]. However, in our recent work, we found that ferritin-induced signal dropout was not reflective of long-term cell survival due to persistent iron accumulation in the vicinity of transplanted cells after cell death [73].

To avoid potentially confounding sources of signal drop-out, signal-enhancing MRI reporter genes have also been investigated. Most notably, Bartelle and colleagues have investigated the divalent metal transporter 1 (DMT1) to increase intracellular Mn^{2+} concentration following systemic manganese delivery and have further developed a Mn^{2+} binding protein, MntR, to induce intracellular Mn accumulation [88, 89]. DMT1 over-expression in tumor cells of interest caused striking T_1-weighted signal enhancement following systemic manganese delivery, even when cells were transplanted in the brain. These initial studies into DMT1 did not, however, address whether it was an appropriate reporter for stem cell tracking over a long period of time.

A final category of MRI reporter genes that has recently been under development is reporters for chemical exchange saturation transfer (CEST) MRI. These reporters provide signal without the use of an exogenous contrast agent based on an exchange of magnetization between solute protons (protons associated with the reporter gene product) and nearby water protons [90]. Proof-of-concept of a variety of CEST-based reporters has been established, primarily in tumor and bacterial cells [91-94]. However, challenges remain in CEST-based cell detection due to the low magnitude of detectable signal change. As of yet, no long-term studies or stem cell detection studies have been performed with CEST-

based reporters. Finally, in reference to all MRI-based reporter genes discussed here, it should be noted that MagA, MntR, and most heretofore developed CEST reporter genes are synthetic or bacterial genes whose approval for use in humans would be much more challenging compared to that of endogenous human genes.

Due to the ability to detect tracer doses of contrast agents with PET and SPECT, a variety of reporter genes for these modalities have been developed in preclinical models, and some have even been applied in humans. The sodium iodide symporter (NIS) transports iodine, its positron-emitting isotopes, and its analogs (including ^{99m}Tc-labeled sodium pertechnetate) into cells. Therefore, it can be used for a reporter for either PET or SPECT, and has been used for monitoring cell therapies in several preclinical studies [80, 95]. The herpes virus type 1 thymidine kinase, HSV1-tk, phosphorylates intracellular nucleosides, and therefore can be used as a reporter gene for cell tracking with radiolabeled nucleoside analogs, such as ^{18}F-FEAU [66]. HSV1-tk has even been applied for therapeutic T-cell tracking in a human patient [96]. Additional PET reporter genes that have been developed for cell therapy include the estrogen receptor ligand binding domain, detected with ^{18}F-FES [97], and the dopamine receptor D2R, detected with ^{18}F-fallypride [98].

With the goal of combining the strengths of MRI and SPECT imaging with those of reporter gene-based cell labeling, one group has investigated the dual MRI/SPECT reporter gene Oatp1 [99]. This reporter has the ability to transport small molecules into cells, including the MRI contrast agent Gd-EOB-DTPA and

the SPECT agent ^{111}In-EOB-DTPA (developed for this application). However, the chelator molecule does not cross the blood-brain barrier, limiting the applicability of this reporter in the intact CNS.

2.3.3 Other approaches

Direct labels and reporter genes are by far the most commonly investigated methods for labeling cells for cell tracking and *in vivo* detection. However, one recently proposed method aims to more directly detect cell death with MRI via interaction of the enzymes activated during apoptosis with a cleverly designed injectable Gd-based contrast agent [100]. In the vicinity of dying cells, the contrast agent is cleaved into molecules with hydrophobic heads (containing chelated Gd) and hydrophilic tails. This causes increased MRI signal due to aggregation of contrast agent into micelle-like nanoparticles and altered Gd relaxation characteristics related to this new structure. In the model tested in this initial study, apoptotic cells transplanted into joints could be detected via increased T_1-weighted signal after direct injection of the imaging probe into the cartilage [100]. Although this approach may not be applicable for cell tracking in many anatomical settings, including the brain, it provides an example of an interesting new approach to cell tracking that does not require pre-transplantation alteration of the cells under investigation.

2.3.4 Current barriers

Despite the wide variety of cell tracking techniques that have been proposed and tested in both preclinical and human trials, no currently available technique has been shown to meet all of the previously described criteria for the

ideal cell tracking technique. Although direct labels are relatively straightforward and their use for establishing initial cell location is well established, they are not useful for long-term cell tracking [62, 63]. Although there are challenging regulatory hurdles associated with clinical translation of reporter genes, the accumulating evidence indicates that reporter genes have great potential to convey essential information regarding long-term survival, location, and even differentiation dynamics and gene expression. Several PET reporter genes have proven effective for long-term monitoring of cell location and survival in preclinical models. However, none have been shown to be applicable in the brain if the blood-brain barrier is intact.

For these reasons, and due to the increased flexibility and applicability of a dual-modality reporter gene, in this work we investigate DMT1 for long-term tracking of stem cell location and survival. We test its capabilities as a dual-modality reporter gene for PET and MRI-based tracking with ^{52}Mn and Mn, respectively.

2.4 DMT1

In this work, we investigate the divalent metal transporter 1 as a reporter gene for cell tracking in the central nervous system. DMT1 transports divalent metals such as, in order of decreasing metal ion selectivity, Cd^{2+}, Fe^{2+}, Co^{2+}, Mn^{2+}, Ni^{2+}, and Zn^{2+} [101]. This protein is ubiquitously expressed in humans, rats, and a variety of other organisms and is highly conserved across species [29]. In mammals, it is expressed in the brain, olfactory epithelium, and gut, with relatively lower expression levels in the brain [29]. In the brain, DMT1 has varied

expression levels across species, but consistently plays important roles in maintaining metal homeostasis. DMT1 expression in the brain has been observed in the hippocampus, striatum, substantia nigra, neocortex, and subcortical white matter [29]. The causes for and biological impact of specific DMT1 localization in different brain regions is not well-established [102].

There are two predominant theories regarding the conditions under which DMT1 transports metals. First, there is evidence that DMT1 is a proton symporter stimulated at low pH to increase metal uptake [103]. Second, the commonly observed co-localization of DMT1 with the transferrin receptor, TfR, leads to the theory that DMT1 transports metals in response to TfR binding status [104]. However, the important role of iron in DMT1 function is generally agreed upon due to the existence of iron-responsive elements in some DMT1 isoforms, resulting in stabilization of the transporter in response to cellular iron levels [105]. DMT1 expression levels have also been shown to be regulated by Mn^{2+} [106].

As a reporter gene, DMT1 over-expression increases intracellular manganese (Mn^{2+}), resulting in selective signal enhancement and detectability in T_1-weighted MRI [88]. Several groups of researchers have previously investigated Mn-based MRI for cellular imaging, both with and without DMT1 over-expression in the cells of interest [44, 88]. In these studies, cancer cells and mononuclear cells internalized sufficient Mn^{2+} for T_1 signal enhancement and *in vivo* detection, indicating that Mn^{2+} holds promise as a cell imaging contrast agent. For imaging most transplanted cell types, we hypothesize that DMT1 over-expression is necessary for specific *in situ* labeling of live cells after systemic

Mn^{2+} delivery. Additionally, we hypothesize that DMT1 may also act as a PET imaging reporter. ^{52}Mn-based PET of DMT1 over-expressing cells could offer increased sensitivity, reduced bulk manganese dose, and provide valuable complementary information when paired with manganese-enhanced MRI (MEMRI).

In considering DMT1 as a reporter, it is essential to consider the potential effects of over-expression and increased metal transport, particularly on hNPCs. Even without DMT1 over-expression, toxic effects of Mn on rodent neural stem cells have been shown in cases of extended exposure [107]. The direct link between increased intracellular Mn and toxic effects on downstream targets such as mitochondria is unknown, though clear evidence exists for Mn-induced oxidative stress [102, 107, 108]. It is even more unclear whether cells have compensatory Mn export mechanisms after accumulation [102]. DMT1 over-expression also leads to increased potential for accumulation of other divalent metals including Cd, Co, Ni, Zn, and, most importantly, Fe. In general, studies investigating the implications of DMT1 upregulation in neuropathogenesis focus primarily on the resulting iron accumulation. For example, a study in PD model mice showed that iron accumulation corresponding to DMT1 expression resulted in oxidative stress and cell death [109]. In any case, it will be essential to study the functional effects of DMT1 expression on cells prior to implementing stable expression for Mn-based imaging.

2.5 Manganese-based PET/MRI

Divalent manganese (Mn^{2+}) is a T1-shortening contrast agent; in regions of high Mn^{2+} concentration, bright signal is observed in T1 weighted images. As a result, manganese-enhanced MRI (MEMRI) techniques and applications have been developed in rodent studies for over two decades. Rodent neuroimaging was an early application of MEMRI, and a large number of studies have been published developing and using this method. Neuroimaging applications of interest include cytoarchitecture enhancement [110], studies of brain region activation [111], neuronal tract tracing [112], tumor detection [26], and evaluation of neurodegenerative disease [113]. MEMRI has also been applied to evaluate myocardial viability and assess therapeutic efficacy [27]. A chelated form of Mn, mangafodipir trisodium (Mn-DPDP), is the only version of this contrast agent to have been successfully applied in humans. Mangafodipir has been used to image liver disease, where a lack of uptake (lower signal with respect to the rest of the liver) can aid in lesion localization [24]. However, the majority of MEMRI applications that have been developed and applied in rodents and other animal models are not applicable in humans due to the high doses of non-chelated metal required.

Although researchers using MEMRI in rodent studies have found techniques to minimize the negative health effects of contrast agent administration on subjects, the biological effects of high Mn doses should be carefully considered in any new imaging application. Acute toxicity of Mn administration primarily arises out of cardiac arrest, likely due to competition of

Mn^{2+} with Ca^{2+} for myocardial uptake through slow Ca^{2+} channels [30, 31, 114, 115]. In the brain, exposure to Mn leads to decreased metabolism, free radical production, abnormal dopamine and GABA signaling, neuroinflammation, and cell death [102, 116]. In the human brain, chronic Mn exposure results in accumulation in the gray matter regions [117]. The resulting progressive damage has symptoms similar to Parkinson's disease, such as headache, insomnia, hyper-myotonia, memory loss, emotional instability, tremors, and speech difficulty [118]. Toxicity in other organs and bodily systems, such as the heart, liver, and reproductive organs, has also been observed [118].

PET imaging with Mn-based contrast agents has also been investigated, but much less thoroughly. Two Mn isotopes, ^{51}Mn ($t_{1/2}$= 46.2 min) and ^{52m}Mn ($t_{1/2}$= 21.1 min), were first produced and used to measure myocardial perfusion by Daube and Nickles in the University of Wisconsin-Madison cyclotron group [37]. Recently, due to the increased interest in and production capabilities of longer-lived radiometals [39, 40], ^{52}Mn ($t_{1/2}$= 5.591 d, β^+= 29.6%, $E(\beta^+)_{max}$= 0.576 MeV) has been produced, separated, and investigated by several groups as a potential PET imaging tracer [33, 35, 36, 38]. The first paper testing ^{52}Mn for PET/CT in rodents showed good imaging resolution with uptake primarily in the gastrointestinal tract and bones over several days after administration, but observed very low brain uptake [33]. Recent efforts by the cyclotron group at the University of Wisconsin-Madison have focused on developing efficient methods of ^{52}Mn and ^{51}Mn separation along with chelation studies for targeted antibody-based PET imaging of cancer [35].

Due to the recent production of ^{52}Mn for PET, the increasing availability of PET/MR scanner technology [41], and the variety of previously developed MEMRI approaches, the potential for dual-modality Mn-based imaging is high. In preclinical studies, the complementary strengths of MRI (soft tissue contrast, high spatial resolution) and PET (sensitivity, functional information, low contrast agent dose) could be a great advantage (**Table 2.1**). Additionally, with ^{52}Mn PET, many MEMRI applications previously developed in animal models could be safely applied in humans using tracer doses of ^{52}Mn (for example, in rodents, <20 ng/kg rather than 60 mg/kg). These lower bulk Mn doses would alleviate many of the previously discussed concerns regarding the toxicity of this metal. In preclinical and clinical PET/MR applications, ^{52}Mn could either be supplemented with or substituted in place of natural Mn [33, 111, 112]. Prior to investigating MEMRI applications with ^{52}Mn PET, it will be essential to characterize the biodistribution and uptake dynamics of ^{52}Mn.

2.6 Targeted MRI for cancer imaging

All modalities used for molecular imaging, both for cell tracking and cancer detection, have strengths and weaknesses. MRI has relatively high spatial resolution and superb soft tissue contrast, which can be advantageous for detecting transplanted cells, imaging solid tumors, detecting metastases, and delineating tumor boundaries [119]. However, MRI has much lower sensitivity than other molecular imaging modalities such as SPECT and PET. Specifically, much higher concentrations of MRI contrast agent are required for observable changes in signal intensity (μM-mM for MRI compared to pM-nM for PET and

SPECT) [47]. This low sensitivity presents a barrier in targeted MR imaging of molecular and cellular processes due to the challenge of delivering sufficient dose of a contrast agent with molecular specificity.

Most clinically applicable MRI contrast agents are biologically inert and distribute in the extracellular space and vascularized tissues [120]. These agents aid in detection, staging, and monitoring of pathologies such as brain tumors, vascular abnormalities, soft tissue lesions, and musculoskeletal injury [120-123]. A limited number of clinically and commercially available agents are biologically active. For example, gadoxetic acid (Promovist®, Eovist®) shows specific hepatocyte uptake, making it well-suited for detecting liver lesions and cirrhosis [124].

In recent years, a large body of work has emerged from the fields of chemistry and materials science aiming to synthesize new MRI contrast agents with specific molecular activity [125]. Cancer-targeted MR contrast agents are of great interest for high-resolution tumor detection and delineation. Signal-enhancing contrast agents, such as gadolinium (Gd^{3+}), may be better suited to these tasks than iron-based agents, which cause signal dropout attributable to a variety of sources [126]. A great number of proposed cancer-targeting MRI contrast agents have been produced and characterized *in vitro* [125, 127-130]. However, few of these have been convincingly translated to *in vivo* animal models at reasonable agent doses to produce observable signal enhancement [131-136].

As observed for many of the above-cited novel agents, MR contrast agents are often subject to a tradeoff between detectability and patient safety. This is due to the low sensitivity of MR and therefore relatively high concentrations required for detection [137]. Dissociation of Gd^{3+} from chelating complexes can cause deposition in the dentate nucleus and contributes to the development of nephrogenic systemic fibrosis in patients with renal failure [138, 139]. For this reason, circulation time and *in vivo* stability of contrast agents are important considerations [140, 141]. In general, macrocyclic agents are the most stable Gd-based contrast agents with the lowest risk of safety concerns [120, 140, 141]. This increased stability indicates that macrocyclic agents may be the most appropriate for cancer-targeted MR imaging, as greater doses may be safely administered for detectable signal enhancement.

2.7 Alkylphosphocholine (APC) analogs

In research aimed at developing novel methods for cancer detection and treatment, investigators commonly aim to target characteristics of cancer cells that differentiate them from normal, healthy tissues. In a variety of cancer cell types, phospholipid ethers (PLEs) have been shown to accumulate to a much greater degree in neoplastic tissues compared to normal tissue [142-144]. Alkylphospholipids, including alkylphosphocholine (APC), are taken up in cellular and intracellular membranes and at high doses can interfere with a variety of lipid processing pathways [145, 146]. Alkylphospholipid analogs have been shown to selectively enter cancer cells via abundant lipid rafts [147]. The cancer-specificity

and potential therapeutic effects of APC analogs has led to interest in their application for cancer imaging and therapy.

With the goal of using this tumor-specific characteristic for imaging and/or therapy, Pinchuk and colleagues synthesized and tested a variety of PLE analogs labeled with ^{131}I for gamma scintigraphy [148]. Tumor avidity, pharmacokinetics, and clearance were investigated to find the best agent for imaging and radionuclide therapy applications, aiming to maximize tumor uptake while minimizing off-target dose. Notably, their results indicated that increasing APC analog alkyl chain length, related to agent hydrophobicity, delayed plasma clearance through the kidney and liver and increased tumor uptake. Based on these studies, the analog NM-404 was selected for further imaging studies. Due to observation that longer plasma circulation led to increased tumor uptake, NM-404/CLR1404 was labeled with ^{124}I ($t_{1/2}$ = 4.2 days) to allow for PET imaging at later time points.

The potential for PET imaging, optical imaging, and targeted radionuclide therapy with labeled CLR1404 was thoroughly investigated in a 2014 publication by Weichert and colleagues [5]. APC analog imaging and therapy agents were resoundingly successful, displaying specific targeting for PET/CT imaging of 57 tumor cell types (spontaneous, transgenic, human, and rodent) and therapeutic efficacy in four cancer models in rodents [5]. In addition, proof-of-concept imaging of human brain tumors and metastases was established. Related studies have shown the utility of fluorescently-labeled CLR1502 for *in vivo* fluorescence imaging and optical surgical navigation [149, 150]. In all, these studies have

prompted the clinical investigation of APC analogs for cancer imaging and targeted therapy. Multiple clinical trials are currently in progress to investigate imaging glioma, non-small cell lung cancer, multiple solid tumor types, and glioblastoma multiforme, as well as radionuclide therapy for multiple myeloma and multiple solid tumor types.

2.8 Objectives

The work described in this dissertation aims to address current barriers in molecular MRI and dual-modality detection of stem cells and cancer. The objectives of this work are (1) to investigate and evaluate DMT1 as a dual-modality reporter gene for long-term *in vivo* imaging of transplanted hNPC location and survival, (2) to develop methods for Mn-based PET and quantitative MRI in rodent neurological applications, and (3) to test the tumor-targeting capabilities of the APC analog Gd-DO3A-404 for molecular MRI of cancer.

For objectives (1) and (2) together, with the complementary strengths of PET and MRI available, our approach to stem cell tracking may offer increased flexibility for *in vivo* cell tracking compared to other cell tracking approaches. No clinically viable imaging technique that communicates long-term information about both cell location and survival currently exists. Our rationale for developing this technique is that we expect it to provide this important information over the course of a cell therapy trial. For this reason, such technology could have a significant impact on both preclinical and clinical research in the development of cell therapies for neurodegenerative diseases. This work aims to establish a new technique for tracking grafted stem cells in the CNS. Our goal is that this method

for acquiring functional information about cell fates will advance the field of cell therapy development for neurodegenerative disease and CNS injury. The accumulating results will also indicate whether this technique could be further applied to tracking of non-neural stem cell therapy, immune cell therapy, or cancer cells. This *in vivo* imaging tool could reduce the use of research animals and provide invaluable longitudinal information regarding the course of therapy in individuals. In the future, this technology may extend to cell tracking in other brain diseases as well as in the heart and skeletal muscle. This type of technology will become an essential tool in the application of cell therapies in humans, as the ability to track cells in ongoing clinical trials would expedite researchers' ability to assess the safety, feasibility, and efficacy of treatment. With this work, we aim to bring *in vivo* progenitor cell imaging markedly closer to the gold standard of histological analysis, utilizing currently available and well-established methods for cell modification and medical imaging [13, 151].

For objective (3), the characterization and validation of a tumor-targeting Gd-conjugated APC analog could markedly advance multi-modal cancer theranostics. Along with existing APC analogs labeled with PET radionuclides and therapeutic agents such as ^{124}I and ^{131}I, respectively, Gd-DO3A-404 has further applicability in MR imaging and neutron capture therapy. To date, very limited numbers of signal-enhancing targeted MRI contrast agents for broad-spectrum cancer imaging have been reported in the literature. Gd-DO3A-404 may represent one of the first tumor-targeted MRI agents that can demonstrate signal-enhancing uptake and retention in multiple cancer types. This may allow

the detection, characterization, and staging of cancer and metastases with high spatial resolution. Furthermore, new applications such as simultaneous PET/MRI with PET-labeled APC analogs can be investigated using this new agent. In the development of this imaging agent, we aim to bridge the current mismatch between scanner resolution and detectability of a molecular imaging agent active at the subcellular level. In all, the studies described in this dissertation are designed to advance the fields of molecular imaging and specific detection of stem and cancer cells by exploring new approaches to reporter gene imaging and novel PET and MRI contrast agents.

Chapter 3: PET/MRI of hNPC transiently over-expressing DMT1

3.1 Preface/Abstract

In this chapter, we investigate the application of divalent metal transporter 1 (DMT1) as a reporter protein for stem cell tracking in the rat brain. In initial investigations of DMT1, we induce transient over-expression of the protein in human neural progenitor cells (hNPC) and observe the functional and imaging results. *In vitro* uptake of Mn-based PET and MRI contrast agents (^{52}Mn and Mn^{2+}, respectively) was enhanced in DMT1 over-expressing human neural progenitor cells (hNPC-DMT1) compared to wild-type control cells (hNPC-WT). After cell transplantation in the rat striatum, increased uptake of Mn-based contrast agents in grafted hNPC-DMT1 was detected in *in vivo* manganese-enhanced MRI (MEMRI) and *ex vivo* PET and autoradiography. These initial studies indicate that this approach holds promise for dual-modality PET and MRI tracking of transplanted stem cells in the central nervous system (CNS) and prompt further investigation into and development of this technique. The work described in this chapter was published in the peer-reviewed journal *Theranostics* in 2015 and reprinted with permission from the publisher [34].

3.2 Introduction

Although the DMT1 protein is well characterized, ubiquitous, and highly conserved across species, its potential as an MRI reporter has only recently been investigated. In 2012, Bartelle and colleagues published a study describing the application of DMT1 for cell detection with MEMRI [88]. *In vivo* studies

showed clear enhancement of DMT1 over-expressing melanoma cells in the mouse hindlimb and glioma cells in the mouse brain. Furthermore, after introducing a DMT1 expression construct *in utero* via electroporation, these researchers also observed signal enhancement in endogenous tissues over-expressing DMT1 in the mouse cortex. Based on these studies, we were interested in several additional applications of this promising reporter gene.

A variety of reporter gene approaches to stem cell tracking in the CNS have been previously investigated, as described in Chapter 2 of this work. However, there does not yet exist an appropriate reporter gene for stem cell tracking in the intact CNS that has the potential for clinical translation. The study by Bartelle and colleagues indicated that DMT1 might hold particular potential as a reporter gene for CNS applications due to the ability of Mn to cross the blood-brain-barrier (BBB), unlike many imaging contrast agents. Despite this potential, the detection of transplanted hNPCs over-expressing DMT1 could be more challenging than that of DMT1-positive glioma cells due to (1) the relatively small number of transplanted hNPCs and (2) the reduced disruption of the BBB by a stem cell transplant when compared with a large tumor, reducing the ease of Mn delivery to the brain parenchyma.

Along with the application of DMT1 to hNPC detection with MEMRI, this reporter also has potential applications in PET imaging. Imaging of DMT1 over-expressing cells with the positron-emitting isotope ^{52}Mn could be more sensitive and clinically applicable than MEMRI-based imaging, since only a tracer dose of Mn would be required. Furthermore, these investigations could facilitate dual-

modality imaging with newly available PET/MRI systems. The recent production of ^{52}Mn at this institution (along with several others) made PET imaging of DMT1 possible [33, 152]. However, prior to the work described in this chapter, ^{52}Mn had not yet been applied either as a direct or chelated tracer in any *in vivo* studies at our institution.

Due to our interest in two new applications of DMT1 as a reporter gene, we performed a set of proof-of-concept experiments exploring MEMRI and PET imaging of hNPC transiently over-expressing DMT1, described in this chapter. To achieve transient over-expression of the DMT1 protein, an expression vector was introduced into the cytoplasm and nucleus (but not integrated into the genome) of hNPC using nucleofection, a combination of electroporation and lipofection. The objectives of the experiments described in this chapter were to test the hypotheses that hNPC can over-express DMT1 after nucleofection, that this expression does not have significant consequences on cell dynamics, and that this over-expression facilitates (1) increased uptake of Mn and ^{52}Mn in vitro and (2) increased uptake of Mn and ^{52}Mn in transplanted hNPC-DMT1 *in vivo*, providing contrast with respect to surrounding tissues and hNPC-WT.

Although the studies described in this chapter were essential to lay the foundation for the work done in the remainder of this dissertation, they do not address the optimal MEMRI and PET methods for detecting transplanted hNPC over-expressing DMT1. Furthermore, they do not address whether this cell labeling and imaging approach is appropriate for long-term *in vivo* tracking of cell

location and viability. These questions are addressed in detail in chapters 4-6 of this dissertation.

3.3 Methods

3.3.1 Cell preparation

A line of human neural progenitor cells (hNPC; G010) has been established from fetal cortical tissue and expanded as previously described [16, 19]. For these experiments, frozen cell aggregates (passage 18-25) were thawed, slowly re-suspended in Dulbecco's modified Eagle's medium (DMEM, Sigma-Aldrich, St. Louis, MO, USA) and 10% DNase, transferred to cell maintenance medium, and maintained for at least two weeks before experiments were performed. Cell maintenance medium consisted of DMEM and Ham's F12 (Sigma-Aldrich) at a ratio of 7:3, supplemented with 1% penicillin/streptomycin/amphotericin (PSA, Life Technologies, Carlsbad, CA, USA), 1% N2 (Life Technologies), 100 ng/ml epidermal growth factor (EGF, Millipore, Billerica, MA, USA), 20 ng/ml fibroblast growth factor 2 (FGF-2, WiCell, Madison, WI, USA), 10 ng/ml leukemia inhibitory factor (LIF, Millipore), and 5 ng/ml heparin (Sigma-Aldrich) [19]. Approximately one-half of the conditioned cell media was removed and replaced with fresh pre-warmed maintenance media every 3-4 days. The cells were passaged by chopping every 10-14 days using a McIlwain automated tissue chopper (Mickle Laboratory Engineering Co. Ltd., Surrey, UK).

To induce transient expression of DMT1 in hNPC, an expression vector encoding the DMT1 protein under the cytomegalovirus promoter (SLC11A2

HaloTag Fusion FlexiVector) was acquired from the Promega Kazusa cDNA clone library (Promega, Madison, WI, USA) and used for cell transfection. The expression vector was introduced into hNPC using the Basic Primary Neurons Nucleofection system (Lonza Group, Basel, Switzerland). The nucleofection method was selected to deliver large amounts of cDNA while maintaining cell viability. Cells were dissociated in DMEM after a 15-minute TrypLE treatment (Life Technologies). For each nucleofection reaction, five million cells were resuspended in nucleofection solution containing 4μg of the DMT1 expression vector, pulsed in the nucleofector device using program C-30, and returned to pre-warmed maintenance media. After transfection, some cells were plated on pre-coated cover slips for immunochemical analysis. Coverslips were treated with poly-L-ornathine and laminin (both from Sigma-Aldrich) to promote cell adherence, and 30,000 cells were plated per cover slip. The remaining cells were returned to suspension culture in a 6-well plate coated with poly-2-hydroxyethyl methacrylate (polyHEMA) to prevent cell adherence. For cell transplantation experiments, hNPC-DMT1 and hNPC-WT were separately collected and resuspended at a concentration of 150,000 cells/μl in transplantation media two days following transfection. Transplantation media consisted of Leibovitz L15 medium (Life Technologies) and phosphate-buffered saline (PBS) at a ratio of 1:1 supplemented with 2% B27 (Life Technologies) and 0.6% glucose [18, 19, 23].

3.3.2 *In vitro* assays

Immunocytochemistry was used to examine expression of several proteins in hNPC, including human DMT1, human glial fibrillary acidic protein (GFAP), and human β-III tubulin. Cover slips were fixed with 4% paraformaldehyde (PFA) and washed with PBS before incubation in blocking buffer (PBS, 5% normal donkey serum (NDS), 0.2% Triton X-100 (Sigma-Aldrich)) for 30 minutes. The appropriate primary antibody was diluted in blocking buffer (detailed antibody information noted in **Table 3.1**). Cells were incubated in primary antibody for 1 hour at room temperature then washed with PBS. Secondary antibody (donkey anti-mouse IgG Alexa Fluor 488; Jackson ImmunoResearch Laboratories, West Grove, PA, USA) was diluted 1:1,000 in blocking buffer and then applied to cells for 30 minutes. After another PBS wash, coverslips were incubated in Hoescht 33258 nuclear stain (Sigma-Aldrich) for 3 minutes before mounting coverslips on glass slides with Fluoromount (Southern Biotech, Birmingham, AL, USA). Images were collected using a Nikon Eclipse fluorescence microscope, a Nikon Intensilight camera, and NIS Element D software (Nikon, Tokyo, Japan). ImageJ software was used for image processing and cell counting (National Institutes of Health, Bethesda, MD, USA). For each expression time point, at least six fields of view on each of three coverslips were analyzed for percent of cells over-expressing DMT1 or expressing GFAP or βIII-tubulin.

To examine whether DMT1 expression and Mn supplementation result in acute toxicity to hNPC, a trypan blue cell viability assay was performed. Cells were transfected to express DMT1, and a control group of cells were subject to

the transfection procedure without introducing the DMT1 expression vector. Cells were then returned to floating culture in maintenance media. One day later, cell samples were supplemented with 0, 100, or 1000 μM $MnCl_2$ and incubated for 24 hours. After collection and dissociation in DMEM, a small amount of the cell suspension was diluted in an equal volume of trypan blue (Sigma-Aldrich). Live and dead cells in each sample were counted, where dead cells were characterized by blue dye infiltration. For each Mn dose and cell type, three individual samples were treated and analyzed. An unpaired two-tailed Student's t-test was used to compare the fraction of dead cells between cell types and Mn supplementation levels.

Table 3.1: Primary antibodies used for immunocytochemistry (ICC) and immunohistochemistry (IHC).

Antibody target	Antibody source	ICC dilution	IHC dilution	Provider	Catalog number
DMT1	Mouse monoclonal	1:500	1:200	Sigma-Aldrich, St. Louis, MO	4891M1
GFAP	Mouse monoclonal	1:500	1:200	StemCells, Inc., Caimbridge, UK	STEM123
βIII-tubulin	Mouse monoclonal	1:500	N/A	Sigma-Aldrich	T8578

Differentiation of hNPC transiently over-expressing DMT1 was examined to probe the potential of DMT1 to alter cell differentiation dynamics. For this experiment, cells were transfected to over-express DMT1 then plated, and a group of non-transfected dissociated control cells was also plated. Cells were grown for two weeks and fed every three to four days with differentiation media, consisting of DMEM and Ham's F12 (Sigma-Aldrich) at a ratio of 7:3, supplemented with 1% PSA and 1% B27 supplement (Life Technologies). After

fixation, cells were stained for differentiation markers using the immunocytochemistry procedure described above.

3.3.3 Animal experiments and tissue analyses

All animal studies were performed in accordance with protocols approved by the University of Wisconsin Institutional Animal Care and Use Committee. Adult wild-type male and female Sprague-Dawley rats (age 80-240 days) were used for cell transplantation and imaging experiments. Rats were housed under controlled temperature and illumination conditions, with unrestricted access to food and water. Cyclosporine (10 mg/kg body weight, Novartis, Basel, Switzerland) was administered to rats intraperitoneally (i.p.) beginning one day prior to cell transplantation until sacrifice.

For transplantation procedures, rats were anesthetized with isoflurane and secured in a stereotaxic frame. Cells were injected bilaterally in two striatal sites (AP +0.5 mm and -0.1 mm; ML ±3.3 mm and ±2.8 mm; DV -4.5 mm) with 2-3 µl cells (150,000 cells/µl) per site. A 10 µl Hamilton Syringe with a 30-gauge sharp tip needle was secured to the stereotaxic frame before needle insertion and cell injection. For each injection site, the needle was slowly lowered into the striatum, maintained at that location for 2 minutes, cells were injected at a rate of 1 µl/min, and the needle was left for 2 additional minutes and then slowly removed [18, 19]. Transfected hNPC-DMT1 were transplanted in the right striatum, while hNPC-WT were transplanted in the left striatum.

At the end of imaging studies, rats were anesthetized with 5% isoflurane, administered 0.2 mL pentobarbital i.p., and transcardially perfused with chilled

0.9% NaCl followed by 4% PFA. After perfusion, brains were submerged in PFA for an additional 24 hours before being switched to 30% sucrose. Thirty-micron slices were sectioned with a frozen stage microtome. Immunohistochemistry was performed using primaries against GFAP to detect transplanted neural progenitors and human DMT1 to observe DMT1 over-expression in transplanted cells. Brain sections were washed in PBS (3×5 minutes) then blocked in blocking buffer (PBS, 3% NDS, 0.25% Triton X-100) for 1 hour at RT. Sections were then transferred to primary antibody diluted 1:200 in blocking buffer and incubated overnight at RT. PBS washes (3×5 minutes) were performed before secondary antibody incubation (donkey anti-mouse AF488 antibody 1:500 in blocking buffer) for one hour. Sections were mounted on glass slides with DAPI mounting medium and examined with a Nikon fluorescence microscope.

3.3.4 MR imaging

In preparation for *in vitro* MRI, hNPC-DMT1 and hNPC-WT were supplemented with 0-400 μM $MnCl_2$ for one hour. Cell samples were then collected, allowed to settle, and rinsed several times to remove extracellular Mn^{2+}. They were then transferred to 0.25 ml microcentrifuge tubes and spun down to form cell pellets. Samples were stabilized in 1.5 ml microcentrifuge tubes filled with 4% agar gel. MR imaging was performed on a 4.7 T preclinical MRI scanner (Agilent Technologies, Santa Clara, CA, USA). To observe the T_1 shortening effects of Mn^{2+}, T_1 mapping was performed using a 3D variable flip angle spoiled gradient echo (VFA SPGR) sequence [153]. Pulse sequence parameters were: TR=8.4ms, TE=3.48ms, flip angles (in degrees) = 5, 10, 15,

20, 30, 45, with gradient and RF spoiling. T_1 times were approximated with nonlinear least squares fitting of the signal data as a function of flip angle, and R_1 maps were calculated ($R_1 = 1/T_1$). This *in vitro* cell imaging procedure was subsequently repeated to confirm the results.

Three animals underwent MR imaging after transplantation of hNPC-DMT1 and hNPC-WT. One day following surgeries, animals were injected with 50 mg/kg of $MnCl_2$ (dissolved in 100mM bicine buffer to a concentration of 100 mM). Fourty-eight and 72 hours later, the animals were anesthetized with isoflurane and scanned with the same 3D VFA SPGR scan for T_1 mapping as was used for *in vitro* imaging. T_1 mapping was performed and R_1 maps were calculated as described above.

3.3.5 Gamma counting, PET, and autoradiography

To observe ^{52}Mn uptake in hNPC, cells were supplemented with 0-0.8 μCi (0-2.3 μCi/μL) of ^{52}Mn in DMEM for one hour. In each cell sample, approximately equal numbers of either hNPC-DMT1 or hNPC-WT were used. After one hour, cells were spun down at 1000 rpm (62 g) for 4 minutes, and the supernatant was removed and replaced. This spin-down and removal step was repeated 3 times. ^{52}Mn uptake was measured by automatic gamma counting on a PerkinElmer Wizard 2480 (Waltham, MA, USA). Counts were measured for 300 seconds with gating centered on the 744 keV gamma peak. During the gamma counting procedure, remaining cell samples were re-counted using trypan blue to verify viable cell numbers and to correct results based on respective cell numbers per sample. The final activity uptake in each sample was corrected by a known ^{52}Mn

calibration factor (units activity per count rate), by a no-activity control, and based on number of cells per sample. The uncertainty of the Poisson-distributed counting data was propagated through each of these correction calculations. To confirm results, this experiment was repeated in a separate trial.

Two animals underwent PET/CT imaging after cell transplantation. One day following cell transplantation, animals were systemically injected with approximately 0.85 mCi ^{52}Mn. One of these subjects (subject 1) received no-carrier-added ^{52}Mn in saline, while the other (subject 2) received ^{52}Mn in 100mM $MnCl_2$ in bicine to mimic the contrast agent delivered for MR imaging. Twenty-four hours after contrast administration, animals were anesthetized with isoflurane and scanned on a Siemens Inveon microPET/CT (Siemens Medical Solutions, Erlangen, Germany). PET images were reconstructed as a single static segment using scatter-corrected OSEM reconstruction. The brain of subject 2 was resected for *ex vivo* brain PET/CT. Sections of 1 mm thickness were cut with a razor and a rat brain matrix slicer, and autoradiographs of these brain sections were collected.

3.4 Results

3.4.1 Cell preparation

In order to use Mn-based contrast agents for cell tracking applications, we first induced over-expression of DMT1 in hNPC to increase the uptake of Mn^{2+} in these cells. The Lonza Nucleofection system was used for this purpose. This is a relatively straightforward and efficient method to induce transient protein expression, which we have previously used for initial investigations of cell

tracking methods [19, 73]. To identify altered protein expression, transfected and wild-type cells (hNPC-DMT1 and hNPC-WT) were plated immediately after transfection, fixed over the course of 10 days after plating, and stained with an antibody against human DMT1. Reporter gene expression was detected in the transfected cell population, with up to 42% of cells over-expressing DMT1 one day following transfection (**Figure 3.1A**). Over the course of 10 days after plating, the percentage of cells over-expressing DMT1 decreased steadily (**Figure 3.1B**). All further experiments were carried out using unsorted hNPC-DMT1 as soon after nucleofection as possible to maximize the portion of hNPC over-expressing the reporter.

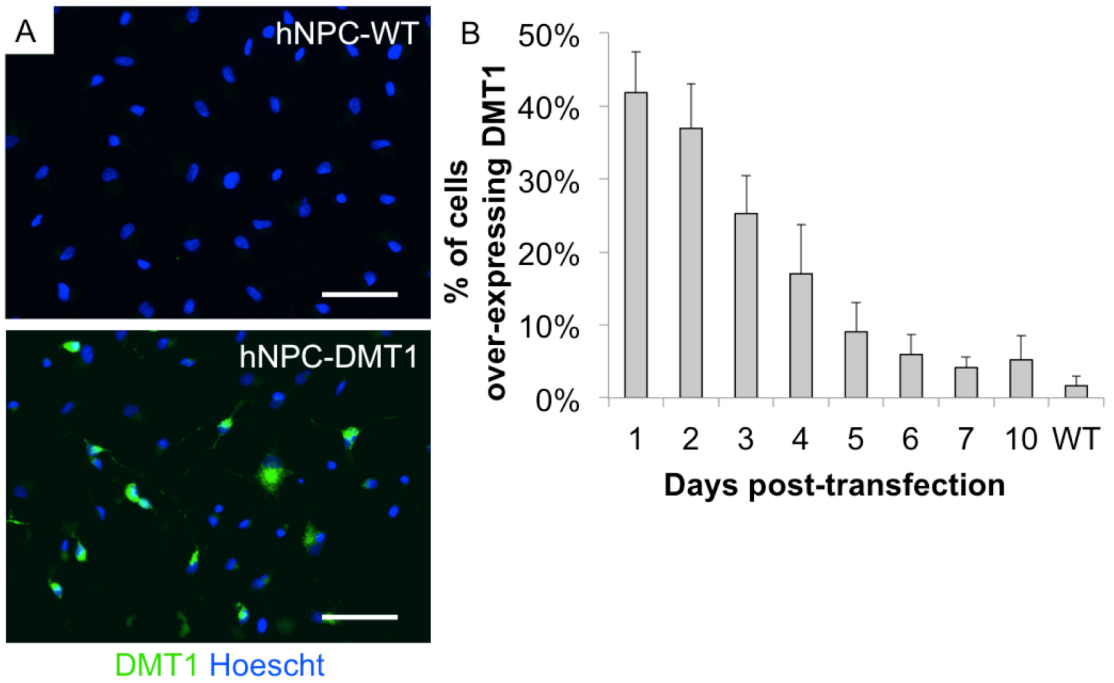

Figure 3.1: Transient DMT1 over-expression following transfection. (A) Immunocytochemistry of hNPC one day following transfection shows that transfected cells express high levels of the DMT1 protein when compared to wild-type cells. (B) After plating transfected and wild-type cells and fixing each day for 10 days, counts of DMT1 over-expressing cells reveal that DMT1 expression decreases toward background (wild-type) levels over the course of 10 days. Scale bar = 50 μm.

3.4.2 *In vitro* assays

The potential toxic effects of Mn^{2+} on both research subjects and neural progenitor cells must be understood before application of this imaging technique in preclinical cell therapy experiments [107, 154]. An *in vitro* toxicity assay was performed to determine whether DMT1-expressing cells exhibit increased sensitivity and cell death in response to manganese exposure. Cells were supplemented with $MnCl_2$ at concentrations of 0, 100, or 1000 μM for 24 hours. The concentration of 100 μM was selected to reflect the approximate expected Mn^{2+} concentration in the rat brain after a systemic injection of $MnCl_2$ at typical doses used for MEMRI [155], whereas the concentration of 1000 μM was used as a positive control. The results of the trypan blue cell viability assay are shown in **Figure 3.2**. Approximately 20% of cells were found to be unviable even in samples not supplemented with Mn^{2+} due to the detrimental effects of the nucleofection solution and transfection procedure on hNPC. For this reason, hNPC-WT subjected to the nucleofection procedure without the introduction of the DMT1 expression plasmid were used as a control in this study. After 100 μM $MnCl_2$ supplementation, neither hNPC-DMT1 nor hNPC-WT showed significantly decreased cell viability, and they did not differ significantly from one another. However, at a Mn^{2+} concentration of 1000 μM, these differences became significant. This concentration is far greater than that required for imaging experiments, either *in vitro* or *in vivo*. This study confirmed that the Mn^{2+} concentration use for this imaging approach would not be a significant contributor

to acute cell toxicity in this application and prompted further *in vitro* and *in vivo* imaging experiments.

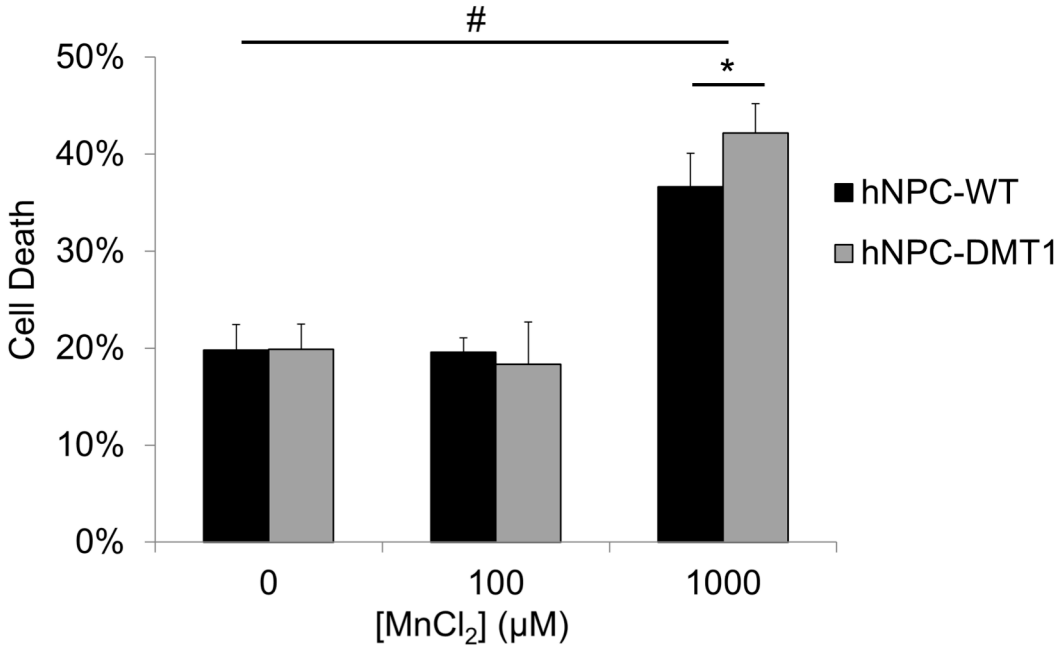

Figure 3.2: Cell viability following DMT1 transfection. Trypan blue cell exclusion assay results reveal no significant increase in hNPC death after 24 hour exposure to 100 μM $MnCl_2$, a concentration on the order of that expected in the brain after systemic $MnCl_2$ delivery. At this concentration, consistent results are observed for hNPC-WT and hNPC-DMT1. Cell death is observed at 0 μM due to the potentially toxic effects of the transfection solution and procedure on cells. The positive control dose of 1000 μM resulted in a significant increase in cell death for both cell types as well as a significant increase of hNPC-DMT1 death compared to hNPC-WT. #: $p<0.05$ compared to corresponding cell type supplemented with 0 μM $MnCl_2$; *: $p<0.05$ compared to hNPC-WT supplemented with same dose. $N=3$ samples per treatment. Error bars represent standard deviation between samples.

Not only is it essential that a cellular imaging method not reduce the viability of the cells of interest, but it must not have significant effects on cell dynamics such as differentiation or proliferation, particularly if these dynamics play a role in the efficacy of therapy. In order to study the effects of transient DMT1 over-expression on hNPC differentiation, transfected cells were plated and grown in differentiation media for two weeks. After differentiation, fixed cells were

immunostained with primary antibodies against human GFAP, to reflect astrocyte differentiation, and human βIII-tubulin, to reflect neuronal differentiation. It was found that both hNPC-DMT1 and hNPC-WT differentiated largely into GFAP-expressing astrocytes, with a small percentage of cells differentiating into βIII-tubulin-expressing neurons (**Figure 3.3A**). These differentiation dynamics are in agreement with previous studies regarding differentiation of late-passage hNPC. We also observed that DMT1 over-expressing hNPC samples had a slightly but significantly reduced percentage of cells expressing βIII-tubulin (**Figure 3.3B**). However, after two weeks of differentiation, a negligible number of transfected hNPCs still over-expressed DMT1, so the specific differentiation characteristics of this subset of cells could not be studied in this experiment.

3.4.3 MR imaging

To investigate whether DMT1 over-expressing cells internalize sufficient Mn^{2+} for T_1-weighted MRI contrast, Mn^{2+} uptake was compared in hNPC-DMT1 and hNPC-WT. Cells were supplemented with 0-400 μM $MnCl_2$ for one hour. The cells were rinsed, spun down into pellets, and imaged with a 3D VFA SPGR sequence for T_1 mapping. The R_1 relaxation rate, which is the inverse of T_1 relaxation time, was calculated from T_1 maps. The resulting R_1 maps of hNPC-WT and hNPC-DMT1 are shown in **Figure 3.4**. At all $MnCl_2$ concentrations, clear contrast was observed between hNPC-DMT1 and hNPC-WT. Importantly, this difference was easily discernable at biologically relevant concentrations of 50-100 μM. A slight increase in R_1 of hNPC-DMT1 is observed even without $MnCl_2$

(0 μM). This may be due to low levels of iron in the cell maintenance media, which is transported by DMT1 and is a weak T_1-shortening agent.

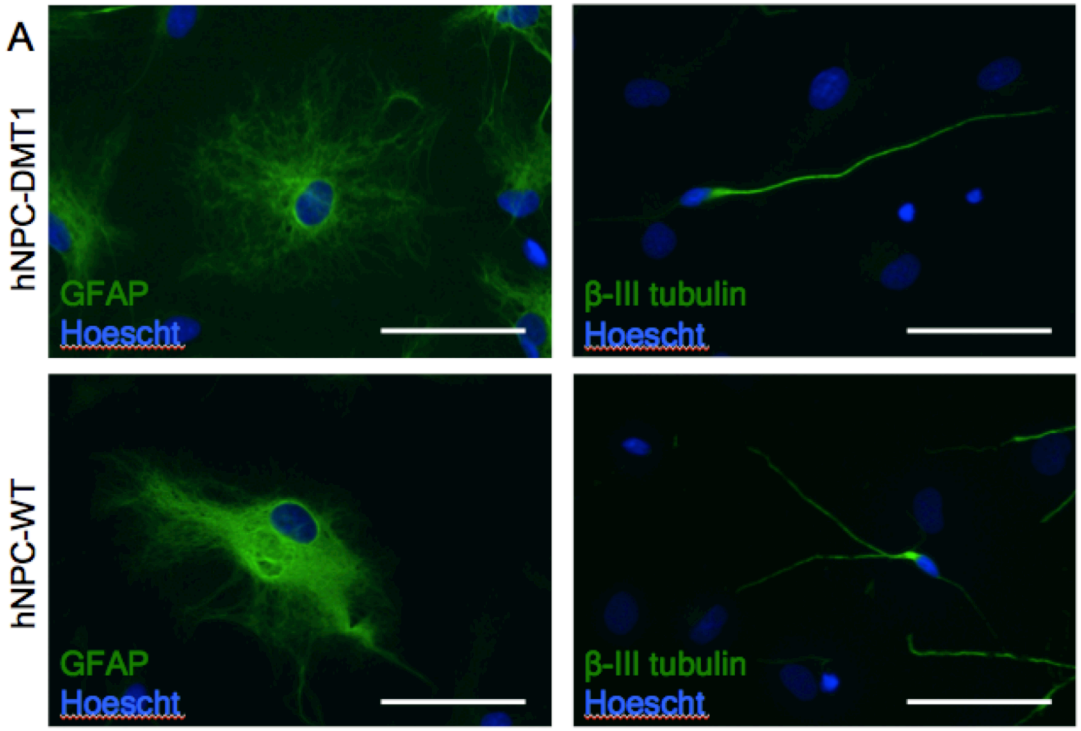

Figure 3.3: (A) Immunocytochemistry of hNPC following transfection and differentiation shows that both WT and DMT1 transfected hNPC differentiate into GFAP-expressing astrocytes and βIII-tubulin-expressing neurons. Scale bar = 50 μm. (B) Counting of GFAP- and βIII-tubulin-stained cells reveals that although both cell types follow typical differentiation patterns for this cell line, there is a significant decrease in βIII-tubulin-marked neuronal differentiation in cells transiently transfected with DMT1. *$p < 0.05$. N=3 coverslips per sample; Error bars represent standard deviation.

For proof of concept *in vivo* cell detection with MRI, three rats were transplanted with hNPC-DMT1 in the right striatum and hNPC-WT in the left. Two days later, $MnCl_2$ was delivered systemically in preparation for MR imaging. At

48 and 72 hours later, the animals were imaged with a T_1 mapping sequence to observe the T_1 shortening effects of Mn^{2+}. After imaging and perfusion, histological evaluation was performed to verify cell survival through the transplantation and imaging procedure. In two of the three MRI subjects, a region of increased R_1 was observed in the right striatum (**Figure 3.5**). This contrast corresponds to the location of transplanted hNPC-DMT1, detected histologically with antibodies against human GFAP (used to detect human cells) and human DMT1 (**Figure 3.6**). Wild-type cells transplanted on the contralateral side were also detected histologically, ruling out the possibility that hNPC-WT were undetectable in MRI simply due to cell death. These preliminary *in vivo* results, along with the Mn^{2+} uptake measured *in vitro*, support our hypothesis that high levels of manganese are taken up in DMT1 over-expressing hNPC, permitting *in vivo* visualization with MRI.

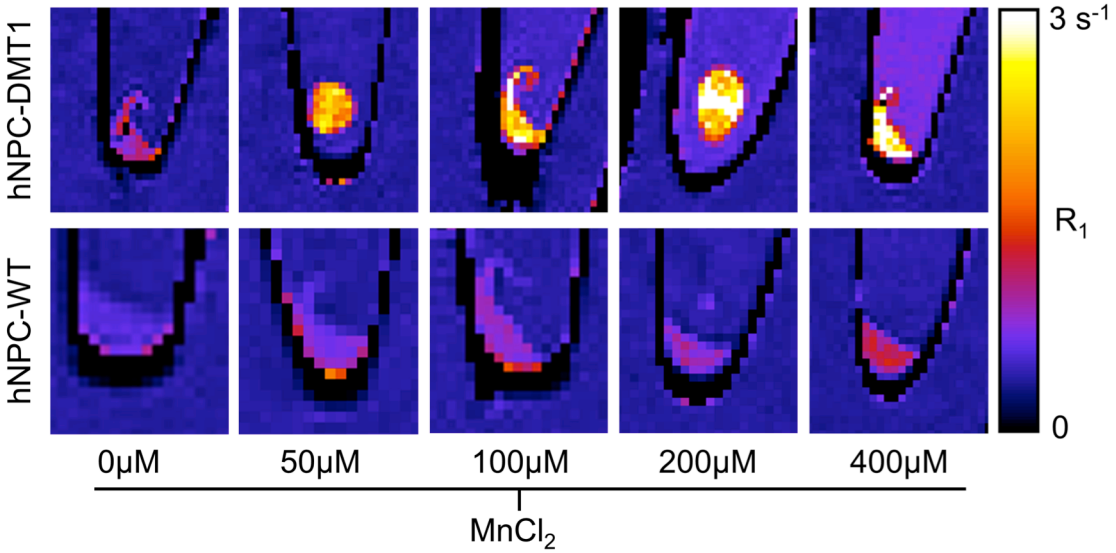

Figure 3.4: Mn^{2+} uptake in hNPC-DMT1 and hNPC-WT with MRI. Representative R_1 relaxation rate maps of hNPC-DMT1 (top row) and hNPC-WT (bottom row) after 1-hour supplementation with $MnCl_2$ at a range of concentrations. Clear contrast is observed between hNPC-WT and hNPC-DMT1 at all $MnCl_2$ concentrations tested.

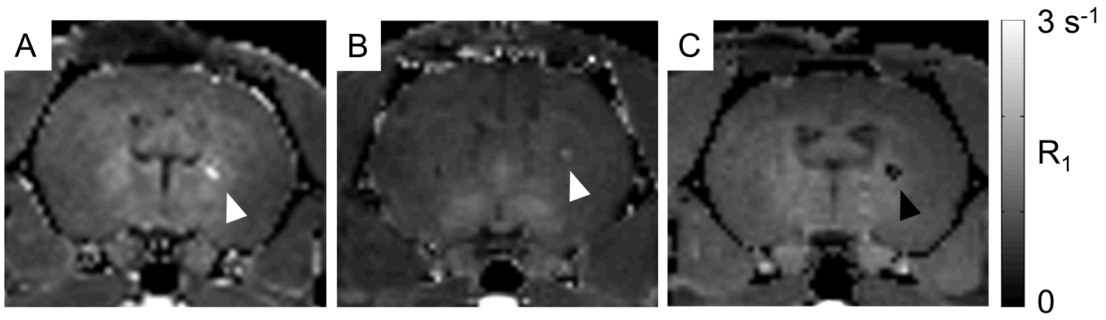

Figure 3.5: *In vivo* manganese-enhanced MRI of rats after hNPC-DMT1 transplantation. (A and B) In two of three subjects, hNPC-DMT1 were detectable on R_1 maps (white arrowheads). (C) In one subject, T_1 mapping failed in the vicinity of hNPC-DMT1, possibly due to hemorrhage-related iron accumulation (black arrowhead).

However, in one of the three subjects, a decrease in R_1 was observed in the vicinity of hNPC-DMT1 (**Figure 3.5C**). In this same region, T_2-weighted imaging showed a hypointense region corresponding to cell location (**Figure 3.7A**). This is likely due to surgery-induced hemorrhage in the brain, which we have found to be a challenging confounding factor in MRI of transplanted hNPC [73]. Iron accumulation was detected with Prussian blue staining and could wipe out MR signal, making T_1 calculation impossible (**Figure 3.7B**).

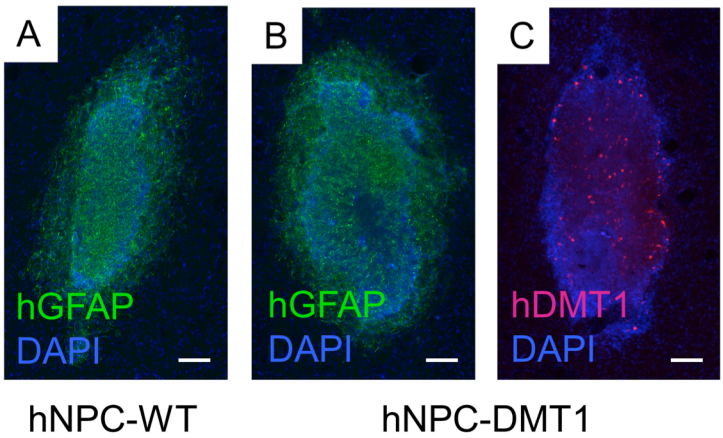

Figure 3.6: Confirmation of cell survival and protein expression following transplantation. Immunofluorescence against human GFAP confirmed that both hNPC-WT (A) and hNPC-DMT1 (B) survived after transplantation and imaging. (C) Transfected cells continued to over-express the human DMT1 protein after transplantation. hNPC-WT staining for hDMT1 is negative (data not shown). Scale bar = 100 μm.

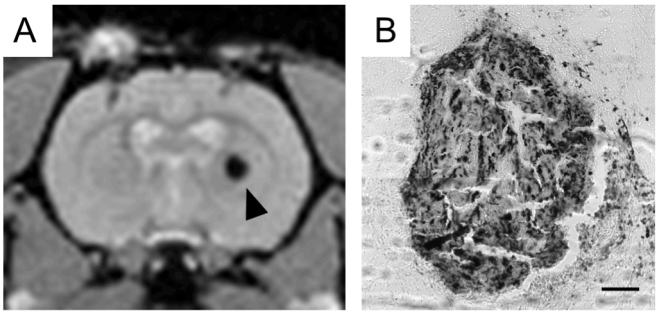

Figure 3.7: Iron accumulation near cells leads to MR signal dropout. (A) The solitary subject that showed no increase in R_1 relaxation rate in the vicinity of hNPC-DMT1 showed hypointense contrast in a T_2-weighted image (black arrowhead). (B) This contrast corresponds to positive Prussian Blue staining, indicating that the signal drop-out could be due to hemorrhage-induced iron accumulation in the vicinity of the cell transplant. Scale bar = 100 μm.

3.5.4 Gamma counting, PET, and autoradiography

Using ^{52}Mn, we could both directly measure Mn uptake in hNPC-DMT1 and further assess whether enhanced uptake compared to hNPC-WT was achieved. The cell preparation procedure outlined above for *in vitro* MRI was mirrored for gamma counting of cellular ^{52}Mn uptake. After a 1-hour incubation with 0-0.8 μCi of no-carrier-added ^{52}Mn, cells were spun down and rinsed to remove extracellular manganese. Gamma counting was used to compare the relative uptake of ^{52}Mn in hNPC-DMT1 and hNPC-WT. Manganese uptake increased linearly with supplemented activity for both cell types, and hNPC-DMT1 showed strikingly increased retained activity when compared with hNPC-WT (**Figure 3.8**). In a parallel study, cells were supplemented with 0-0.8 μCi of ^{52}Mn in 50 μM $MnCl_2$, and identical gamma counting results were obtained (data not shown). These results demonstrate that DMT1 over-expressing cells show increased uptake of manganese-based contrast agents, even at tracer levels of supplemented ^{52}Mn. These *in vitro* results prompted studies of cell detectability with *in vivo* PET.

For initial observation of ^{52}Mn uptake in the brain and in transplanted hNPC, PET/CT (combined PET and computed tomography) imaging was performed in two rats. Rats were systemically delivered 0.85mCi ^{52}Mn two days after cell transplantation and imaged 24 hours later. One rat received ^{52}Mn in saline, while another received ^{52}Mn supplemented with 100μM $MnCl_2$ in bicine to mimic the MRI contrast administration and bulk manganese dynamics. ^{52}Mn was taken up in the gastrointestinal system, bone, and areas of inflammation, but low

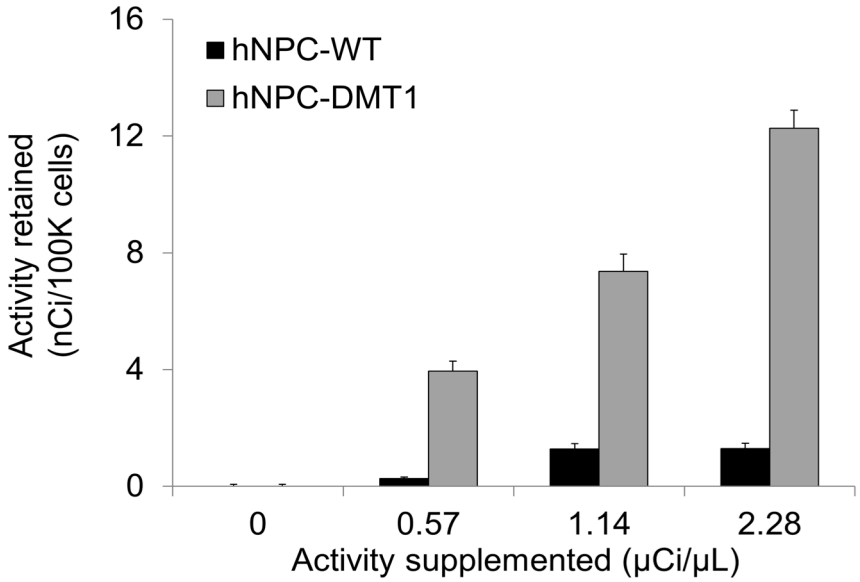

Figure 3.8: *In vitro* uptake of ^{52}Mn in hNPC. hNPC-DMT1 show increased ^{52}Mn uptake compared to hNPC-WT after a one-hour incubation as measured by gamma counting (representative results from one trial shown). Error bars represent propagated error from Poisson-distributed counting data.

brain uptake was detected *in vivo* in both subjects (**Figure 3.9A**). *Ex vivo* PET/CT showed low levels of brain uptake, with slightly increased ^{52}Mn levels in the right striatum, corresponding to the location of hNPC-DMT1 (**Figure 3.9B**). Autoradiographs also indicated low but detectable levels of ^{52}Mn in the brain, with increased activity in the vicinity of transplanted hNPC-DMT1 (**Figure 3.9C**).

These initial results indicate that although ^{52}Mn-based PET imaging in the brain does not directly mirror MEMRI results, DMT1 shows potential for ^{52}Mn PET-based cell detection in the brain.

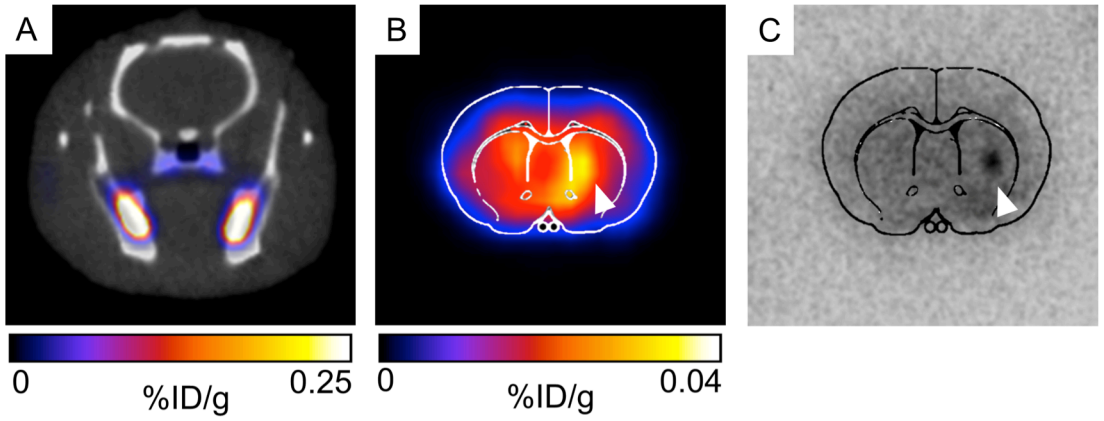

Figure 3.9: PET/CT and autoradiography of transplanted hNPC-DMT1. (A) Very low brain uptake is observed in ^{52}Mn-based PET/CT imaging *in vivo*. (B) When the brain is excised and imaged *ex vivo*, low levels of brain uptake are detectable. Both *ex vivo* imaging and autoradiography indicated that increased levels of ^{52}Mn are retained in the vicinity of hNPC-DMT1 (white arrowhead, B and C).

3.5 Discussion

In the work presented in this chapter, we have performed preliminary *in vitro* and *in vivo* imaging studies to lay the foundation for a new dual-modality approach for stem cell imaging in the central nervous system. To investigate the potential of DMT1 as a reporter gene for *in vivo* stem cell tracking with manganese-based PET and MRI, we induced transient over-expression of DMT1 in hNPC. *In vitro* supplementation of $^{52}MnCl_2$ and $^{nat}MnCl_2$ was used to compare manganese uptake in hNPC-DMT1 and hNPC-WT with gamma counting and T1 relaxation measurements, and we observed enhanced Mn uptake in hNPC-DMT1. Finally, in proof-of-concept studies for *in vivo* cell tracking, hNPC-DMT1

were transplanted into the striatum of adult wild-type rats. Contrast due to increased Mn uptake in transplanted hNPC-DMT1 was detected with *in vivo* MEMRI and *ex vivo* PET and autoradiography.

In vitro assays were used to confirm DMT1 expression by transfected cells and to test the potential toxicity of combined DMT1 expression and manganese supplementation. The observation of slowly decreasing DMT1 over-expression is acceptable for these proof-of-concept studies and has been previously observed following nucleofection in our other reporter gene studies [19]. However, a line of cells stably expressing DMT1 needs to be developed for long-term cell tracking, detecting cell graft rejection, and more thoroughly characterizing the effect of this imaging technique on hNPC dynamics. The cell viability study showed that transient DMT1 over-expression and Mn supplementation did not have significant effects on cell viability at relevant concentrations for *in vivo* MRI, in agreement with previous studies investigating combined DMT1 expression and Mn supplementation on cells [88]. However, investigations of the effects of Mn on hNPC by other researchers show more significant toxicity and indicate that trypan blue may not be a sufficiently sensitive method for detecting effects on cell viability [107]. The cell viability study further showed that extremely high concentrations of Mn have significant detrimental effects on cells. This result supports the goal of minimizing the supplemented Mn concentration, which a ^{52}Mn PET tracer may help accomplish. The toxicity at high concentrations also indicates that combined DMT1 expression and Mn supplementation does indeed

harm cells and prompts future studies into the variety of mechanisms by which viability is affected.

Our studies into the effect of transient DMT1 over-expression showed that although both hNPC-WT and hNPC-DMT1 showed typical differentiation dynamics for the G010 line at this late-passage stage, there was a significant difference in neuronal differentiation between the two cell types. Due to the transient nature of DMT1 over-expression in these experiments, the specific differentiation dynamics in the sub-population of cells over-expressing DMT1 cannot be easily elucidated. Furthermore, because the control cell population did not go through the nucleofection process, which further introduces stress and toxins to cells, the source of the difference in differentiation is not entirely clear. In further work, a line of stably expressing $hNPC^{DMT1}$ will allow more flexibility and longevity in studies of toxicity and cell dynamics. Studies with stable DMT1 over-expressing cells, presented in chapter 6 of this dissertation, will more thoroughly investigate the effects of DMT1 expression and manganese supplementation on cell differentiation, proliferation, and viability over a longer period of time. However, for the purposes of this proof of concept work, the lack of significant toxicity at imaging-relevant concentrations encouraged the initiation of imaging studies.

Both *in vitro* MRI and ^{52}Mn gamma-counting experiments confirmed our hypothesis that hNPC-DMT1 take up higher levels of manganese than their wild-type counterparts. These studies indicated that this technique may be sufficiently sensitive for *in vivo* applications, and were in agreement with a previous study of

DMT1 as an MEMRI reporter gene [88]. Indeed, *in vivo* MEMRI of hNPC-DMT1 confirmed that in the absence of confounding signal dropout, manganese uptake was sufficient to increase the R_1 relaxation rate. This permitted visualization of hNPC-DMT1, but not hNPC-WT, on R_1 maps. Histological confirmation of survival of both cell types confirmed that T_1 contrast specific to DMT1-expressing cells is observed. However, one subject did not show R_1 increase, likely because of iron deposition as a result of the surgery procedure. Iron is a potent T_2*-shortening contrast agent and can cause regions of signal dropout. It is also possible that the manganese concentration was high enough to significantly reduce T_2 relaxation time, muting signal from the region of high Mn^{2+} uptake. Other researchers have observed similar effects when mononuclear cells were pre-labeled with Mn before transplantation and MRI [44].

On the other hand, *in vivo* ^{52}Mn PET studies revealed very low brain Mn uptake. This was a surprising result, because notable brain uptake of Mn over the course of 24 hours has been observed in a variety of MEMRI studies [155]. Upon further investigation with *ex vivo* PET and autoradiography, low levels of activity in the brain were detected, on the order of 0.1 %ID/g with higher activity in the vicinity of hNPC-DMT1. Though encouraging, these results prompt further investigations into the biodistribution and temporal dynamics of ^{52}Mn after systemic delivery, which will be essential to establish the applicability of this imaging technique in the brain. These results also indicate that careful examination of the cellular and brain uptake of natural Mn and ^{52}Mn both in the presence and absence of one another is essential.

The work in this chapter demonstrates several of the potential strengths of DMT1, particularly in comparison with other reporter genes previously investigated in our lab, such as ferritin and luciferase [19, 73]. Firstly, the MR signal enhancement (positive contrast) resulting from increased Mn^{2+} uptake in DMT1 over-expressing cells allows more specific detection of cell location. This is clearly demonstrated in **Figures 3.5** and **3.7**, in which iron deposition could be easily distinguished from enhanced signal due to Mn^{2+} accumulation. In comparison with iron-dependent cell labeling techniques such as ferritin or SPIO nanoparticles, the DMT1/Mn^{2+} approach limits the confounding factors in identifying cell-specific contrast [62, 64, 73]. Second, the increased uptake of Mn^{2+} contrast agents for two imaging modalities in hNPC-DMT1 indicates that this method has potential for dual-modality cell tracking with both MRI and PET. If the PET detectability of transplanted cells can be improved by further development of ^{52}Mn imaging protocols, this approach could offer a variety of complementary strengths of two clinical imaging modalities. In comparison, most previously developed reporter gene approaches are limited to one imaging modality [73, 79, 80, 83, 94, 97].

The results of this work indicate several avenues of future investigation, several of which are addressed in the following chapters of this work. Most importantly, a stable DMT1-expressing cell line will open doors for a variety of future studies. These studies will probe the long-term potential of this cell tracking technique, the ability to detect cell death or differentiation, and the long-term effects of DMT1 expression and manganese supplementation on cell

dynamics. Furthermore, this approach could also be explored for direct labeling of cells. Cells transiently or stably over-expressing DMT1 could be incubated with Mn-based contrast agents prior to cell transplantation. PET and MRI could then be performed for an estimated 2-3 weeks after surgery to detect cell location and graft integrity. Although this approach would suffer the same weaknesses as other direct labeling methods, it could be used for dual-modality cell detection and would eliminate the need for systemic manganese delivery. Last, it is essential to study and establish the baseline dynamics of Mn uptake and efflux into and out of the rat brain at systemic dose levels relevant to both PET and MRI, so that changes from baseline can be detected more faithfully.

3.6 Conclusion

In conclusion, in this chapter we have established proof-of-concept for a novel dual-modality imaging approach. $^{52}Mn^{2+}$ PET and MEMRI were used to establish the potential of DMT1 as a reporter gene for neural stem cell tracking in the rat brain. We have confirmed that DMT1 is a compelling reporter gene candidate for stem cell detection with both MRI and PET. This work supports our further investigations into the potential of DMT1 for providing functional information regarding cell fates, which will be discussed in Chapter 6. It further indicates that prior to these studies, it is essential to develop, test, and optimize quantitative MEMRI and ^{52}Mn PET brain imaging protocols to maximize the likelihood of cell detection and the potential for translation of this cell tracking approach.

Chapter 4: Uptake and retention of manganese contrast agents for PET/MRI in neurological applications

4.1 Preface/Abstract

In this chapter, we investigate and develop protocols for manganese-enhanced MRI (MEMRI) and $^{52}Mn^{2+}$ PET for neuroimaging and stem cell detection in the brain. MEMRI is an established neuroimaging method for signal enhancement, tract tracing, and functional studies in rodents [25, 32, 156]. Along with the increasing availability of simultaneous PET/MRI scanners, the recent development of the positron-emitting isotope ^{52}Mn has prompted interest in the use of Mn^{2+} as a dual-modality contrast agent. In this work, we characterize and compare the uptake of systemically delivered Mn^{2+} and radioactive $^{52}Mn^{2+}$ in the rat brain for MRI and PET, respectively. Additionally, we examine the biodistribution of two formulations of $^{52}Mn^{2+}$ in the rat. In MRI, maximum uptake was observed one day following delivery of the highest $MnCl_2$ dose tested (60 mg/kg), with some brain regions showing delayed maximum enhancement 2-4 days following delivery. In PET, we observed low brain uptake after systemic delivery, with a maximum of approximately 0.2 %ID/g. We also studied the effect of final formulation vehicle (saline compared to $MnCl_2$) on $^{52}Mn^{2+}$ organ biodistribution and brain uptake. We observed that the addition of bulk Mn^{2+} carrier to $^{52}Mn^{2+}$ in solution resulted in significantly reduced $^{52}Mn^{2+}$ uptake in the majority of organs, including the brain. These results lay the groundwork for further development of ^{52}Mn PET or dual Mn-enhanced PET/MR neuroimaging in

rodents and indicate several possibly valuable applications of ^{52}Mn PET in other organs and systems.

4.2 Introduction

In initial proof-of-concept studies, we observed promising results using DMT1 as a PET/MRI reporter for stem cell tracking (described in Chapter 3). However, we encountered several challenges due to our lack of prior experience with *in vivo* Mn-based imaging. In MRI studies, we observed great variability in both brain Mn^{2+} uptake and in the effects of $MnCl_2$ administration on rat health and behavior. Additionally, we observed low brain uptake of ^{52}Mn with PET/CT, *ex vivo* imaging, and autoradiography. Before proceeding with hNPC^{DMT1} tracking studies, more thorough evaluation and development of MEMRI and ^{52}Mn PET imaging protocols were essential.

In the setting of neuroimaging, methods for MEMRI in the rodent have been developed for a variety of applications, including generalized cytoarchitecture enhancement, activation studies, and neuronal tract tracing [25, 32]. Along with determining the best way to deliver Mn^{2+} for appropriate contrast uptake and enhancement, several methods have already been proposed to minimize toxicity while delivering the maximum dose for sufficient imaging contrast [32, 157]. For instance, intrathecal injection and osmotic pumps provide intriguing alternative methods for Mn^{2+} administration [158, 159]. Several other works also assert that slow systemic delivery via tail vein infusion can sufficiently reduce toxicity without the need for more specialized delivery techniques [155, 160]. Specifically, one such study examined the effect of varying the time between contrast

administration and imaging, and confirmed a correlation between R_1 relaxation rate ($R_1=1/T_1$) and *ex vivo* elemental analysis of Mn^{2+} uptake [155]. This work showed maximum T_1 change at one day following contrast administration, but did not address slightly later time points between 2-4 days, which are of interest to further reduce the potential combined effects of Mn^{2+} and isoflurane anesthesia on animal health. An additional motivation in this work is to observe the uptake of Mn^{2+} in specific brain regions where stem cells are grafted for therapy, such as the striatum [34]. $MnCl_2$ biodistribution studies in rats have also indicated high uptake of Mn^{2+} in a variety of other organs and glands including the liver, kidney, salivary glands, and pancreas [161].

Compared to MEMRI, ^{52}Mn PET has been much less thoroughly investigated in terms of contrast agent delivery, ^{52}Mn biodistribution, PET image acquisition, and image reconstruction and analysis techniques. Few published studies address ^{52}Mn PET, with the majority of these works focusing on production and separation of the isotope rather than *in vivo* imaging applications [33, 36, 37]. As demonstrated by Topping and colleagues [33] and confirmed in our work in Chapter 3, relatively low brain uptake of $^{52}Mn^{2+}$ (less than 1% ID/g) is observed *in vivo*. To improve brain uptake, $^{52}Mn^{2+}$ supplementation with bulk $MnCl_2$ may potentially increase circulation time and therefore allow more $^{52}Mn^{2+}$ to be transported or diffuse into the brain, both of which are mechanisms of brain Mn^{2+} uptake [33, 162-165]. The supplementation of $^{52}Mn^{2+}$ with $MnCl_2$ could also be of interest for simultaneous PET/MRI studies, further prompting more thorough investigation of this contrast agent preparation.

In this chapter, we characterize and compare the uptake of $^{52}Mn^{2+}$ and non-radioactive Mn^{2+} in the rat brain using MRI and PET imaging, using similar contrast delivery and image time course protocols for both modalities. With these experiments, we aim to provide new knowledge regarding the contrast agent composition, dose, delivery method, and imaging time point to maximize contrast enhancement and ^{52}Mn uptake for future detection of transplanted stem cells in the rat brain. By testing the uptake characteristics of both no-carrier-added (NCA) and carrier-added (CA) $^{52}Mn^{2+}$, we further hope to elucidate whether Mn^{2+} could be used as a dual-modality signal-enhancing contrast agent for PET/MR. For our further pursuit of manganese-based imaging of transplanted stem cells described in Chapter 3, the goal of these studies is to select the best contrast agent dose, formulation, delivery method, and imaging time point to facilitate sufficient Mn^{2+} supplementation for uptake and detection of cells over-expressing DMT1, a manganese transporter protein.

4.3 Methods

4.3.1 Animal experimentation

All animal experimentation was performed following NIH guidelines and in accordance with protocols approved by the University of Wisconsin Institutional Animal Care and Use Committee. Adult female Sprague Dawley rats were used for experiments. Rats were housed under controlled temperature and light conditions and had free access to food and water. Upon completion of experimentation, rats were euthanized by slowly introducing CO_2 to the rat in an enclosed chamber.

4.3.2 Systemic delivery of Mn

In preparation for imaging, rats were delivered Mn^{2+} in the form of $MnCl_2$ solution and/or $^{52}Mn^{2+}$. Animals were anesthetized with light isoflurane (0.5-2% in oxygen) and placed on a warming pad to maintain body temperature. Contrast agent, prepared as described below, was delivered via tail vein with an infusion pump at a rate of 2 mL/hr. Following infusion, the infusion line was flushed with heparinized saline and animals were delivered 5 mL pre-warmed saline subcutaneously.

Prior to MRI, doses of 30, 45, and 60 mg/kg $MnCl_2$ at a concentration of 66.7 mM in bicine-buffered saline were delivered to 9 animals (N=3 per group). ^{52}Mn was prepared as described previously, with an average specific activity of 0.8 GBq/μmol [35]. No-carrier-added (NCA) $^{52}Mn^{2+}$ was prepared by diluting $^{52}Mn^{2+}$ in saline to 1.5 mCi/mL (55.5 MBq/mL) then delivered at a dose of 2 mCi/kg (74 MBq/kg, N=6 for *ex vivo* gamma counting and N=4 for *in vivo* PET/CT). Alternatively, $^{52}Mn^{2+}$ was diluted in 66.7 mM buffered $MnCl_2$ solution at a concentration of 0.37 mCi/mL (13.7 MBq/mL). In this preparation, animals were delivered 2 mCi/kg (74 MBq/kg) $^{52}Mn^{2+}$ in approximately 45 mg/kg $MnCl_2$, which corresponds to the average dose used for MEMRI studies (N=6 for *ex vivo* gamma counting and N=1 for *in vivo* PET/CT). This contrast agent preparation is herein referred to as carrier-added (CA) $^{52}Mn^{2+}$.

4.3.3 MEMRI

To observe brain manganese uptake with MRI, *in vivo* R_1 mapping was performed using a 4.7 T preclinical MRI scanner (Agilent Technologies, Santa

Clara, CA, USA). At each imaging time point, a series of 3D SPGR images were acquired using the following pulse sequence parameters: TR = 5.96 ms; TE = 2.25 ms; flip angles (in degrees) = 3, 7, 12, 18, 25; matrix size = 64×128×128; field of view = 35×35×35 mm^3; scan time = 4:54 min:sec per flip angle. Additionally, an actual flip-angle imaging (AFI) SPGR scan was acquired for flip angle mapping using the following parameters: TR1/TR2 = 5.9/29.5 ms; TE = 2.22 ms; flip angle = 55°; matrix size = 64×64×64; field of view = 35×35×35 mm^3 [166]. R_1 times were estimated using weighted linear least squares estimation with flip angle correction [167]. Images were acquired and R_1 maps were calculated pre-contrast and at days 1, 2, 4, 7, and 14 following $MnCl_2$ administration in order to analyze the *in vivo* dynamics of Mn^{2+} uptake and efflux.

To measure and quantify Mn^{2+} uptake in the whole brain and individual brain regions, brains were manually segmented from surrounding tissue at all imaging time points. Using FMRIB's Linear Image Registration Tool, FLIRT, manually segmented images were registered to a Waxholm Space atlas of the Sprague Dawley rat brain [168-172]. Following registration, the atlas was used to segment the following sub-regions for further quantification and analysis: striatum, neocortex, olfactory bulb, corpus callosum, basal forebrain, globus pallidus, thalamus, hippocampus, hypothalamus, brain stem, cerebellum, and trigeminal tract. T_1 mapping, segmentation, registration, and image processing were performed in Matlab R2014b (The MathWorks, Natick, MA).

4.3.4 ^{52}Mn gamma counting of brain uptake

To observe the whole brain uptake of $^{52}Mn^{2+}$ following administration of NCA and CA $^{52}Mn^{2+}$, subjects were sacrificed either 24 hours (N=3 per contrast agent group) or 48 hours (N=3 per contrast agent group) following intravenous infusion of $^{52}Mn^{2+}$. The brain was immediately excised and rinsed once in distilled water, the olfactory bulb (and trigeminal nerves, if still intact) were removed, and the brain mass was measured. Brain-average $^{52}Mn^{2+}$ uptake was measured by gamma counting using the average of three 2-minute counts with gating centered on the 744 keV gamma peak. Counting data was corrected for gamma counter efficiency and decay-corrected to injection time to calculate the percent injected dose per gram (%ID/g) of brain tissue. A two-tailed Student's t-test was used to compare the brain uptake of $^{52}Mn^{2+}$ based on contrast agent form and measurement time point.

4.3.5 ^{52}Mn PET

In vivo ^{52}Mn PET/CT was performed in five subjects (N=4 with NCA $^{52}Mn^{2+}$, N=1 with CA $^{52}Mn^{2+}$) on a Siemens Inveon microPET/CT (Siemens Medical Solutions, Erlangen, Germany). PET acquisition time points varied between subjects, as an essential aspect of this experiment was to guide the design of a consistent ^{52}Mn PET imaging protocol. In the first PET/CT experiment, two subjects were administered 2 mCi/kg $^{52}Mn^{2+}$ (one CA, one NCA) and 30-60 minute full-body PET/CT scans were acquired 1, 2, 4, and 7 days later with a single static time frame. Additionally, the subject delivered NCA $^{52}Mn^{2+}$ in this experiment was scanned 2 hours following delivery. This scan time point was

not feasible for the other subject due to the negative combined effects of isoflurane and bulk $MnCl_2$ immediately after delivery. In a second experiment, three subjects delivered 2 mCi/kg NCA $^{52}Mn^{2+}$ were scanned for 30-60 minutes at 0.5, 1.5, 3.5, 7.5, 24, 48, and 72 hours following contrast delivery. Two of these subjects were additionally scanned at 7 days following delivery. For all full-body PET scans, continuous bed motion with 5 passes was used for PET acquisition due to the relative size of the rat compared to the PET scanner field of view.

For PET/CT reconstruction, attenuation maps were calculated using manual registration of full-body PET and CT images. Attenuation-corrected PET images were then reconstructed using a vendor-provided 2-dimensional ordered subset expectation maximization (OSEM) reconstruction algorithm. Scatter correction was not applied during reconstruction due to the tendency of this correction to reduce detectable signal in low-count brain imaging protocols, as has been observed in $^{15}O[H_2O]$ brain activation studies and was expected in this setting [173]. For each subject and time point, the brain-average %ID/g was calculated by comparing the uptake in the manually delineated whole brain to the total delivered activity and normalizing by the mass of the brain, assuming tissue density equal to that of water.

4.3.6 ^{52}Mn biodistribution

Biodistribution of $^{52}Mn^{2+}$ was measured with *ex vivo* organ gamma counting in order to examine the uptake of both NCA and CA $^{52}Mn^{2+}$ in major organs of the rat. $^{52}Mn^{2+}$ was prepared either at a concentration of 0.33 mCi/mL

(12.2 MBq/mL) in saline (NCA) or at an activity concentration of 0.37 mCi/mL (13.7 MBq/mL) in 66.7 mM $MnCl_2$. A target injection dose of 100 uCi was delivered to rats (*N* = 3 per time point and per contrast agent formulation) via tail vein infusion at a rate of 2 mL/hr for an average of 8-10 minutes. For CA $^{52}Mn^{2+}$, the added carrier dose corresponded to approximately 4.5 mg/kg $MnCl_2$. Animals were sacrificed and organs were harvested at 4 or 48 hours initiation of contrast delivery. For each organ, the sample was weighed and activity was measured by gamma counting with a PerkinElmer Wizard 2480 (Waltham, MA, USA) to calculate %ID/g. For statistical analysis, a two-tailed Student's t-test was used to compare the uptake of $^{52}Mn^{2+}$ at 4 and 48 hours and for the two contrast agent formulations.

4.4 Results

4.4.1 Systemic delivery of Mn

The bulk doses of Mn^{2+} systemically delivered for MEMRI in the rodent brain have been known to cause somnolence and side effects in the liver, heart, and brain [116, 118]. Different methods of manganese delivery have been proposed and tested to minimize these harmful effects while providing sufficient Mn^{2+} for brain signal enhancement [32, 158-160]. In this study, we employed a contrast delivery protocol using a 15-45 minute intravenous (i.v.) infusion based on suggestions by other researchers to determine whether this approach sufficiently reduced harmful effects for *in vivo* imaging [110, 155]. We observed that by delivering manganese via slow i.v. infusion, while additionally keeping the subject warm and hydrated, we were able to reduce somnolence and eliminate

observable toxicity. In the subjects that received larger bulk doses of $MnCl_2$, we observed a qualitative correlation between total dose and both intensity and duration of somnolence. However, even in the subjects delivered the highest dose tested (60 mg $MnCl_2$ per kg body weight), the rats recovered to normal demeanor and activity levels within 24 hours.

4.4.2 Brain uptake and efflux measured by MEMRI

To observe the effect of $MnCl_2$ dose and imaging time point on signal enhancement in the brain, we administered three doses of $MnCl_2$ to rats (30, 45, and 60 mg/kg, N=3 per dose group) using slow i.v. infusion as described above. We then performed T_1 mapping with MRI over the course of two weeks following Mn administration. R_1 relaxation rate ($R_1 = 1/T_1$) in the whole brain and in specific brain sub-regions was estimated from a set of variable flip angle spoiled gradient echo (SPGR) acquisitions at each time point.

After T_1 mapping and manual segmentation, whole-brain R_1 enhancement was measured at all time points and doses. Representative R_1 maps in a single subject for each dose group over the course of 2 weeks are shown in **Figure 4.1**. General T_1 shortening was observed in the whole brain, with greatest enhancement near the ventricles and diffusing throughout the whole brain over time. The greatest whole-brain R_1 enhancement was observed one day following contrast administration for all doses tested (**Figure 4.2A**). Due to a high level of inter-subject variability of uptake, significant differences were not observed between dose groups, although there was a clear trend toward increased signal

enhancement in the rats from the higher dose groups compared to the 30 mg/kg dose group (**Figures 4.1 and 4.2A**).

Quantification of R_1 relaxation rate in specific brain regions was performed via manual segmentation of the brain prior to registration to a Sprague Dawley rat brain atlas for regional delineation. We then determined R_1 enhancement in the striatum, relevant for stem cell tracking, along with a variety of other brain

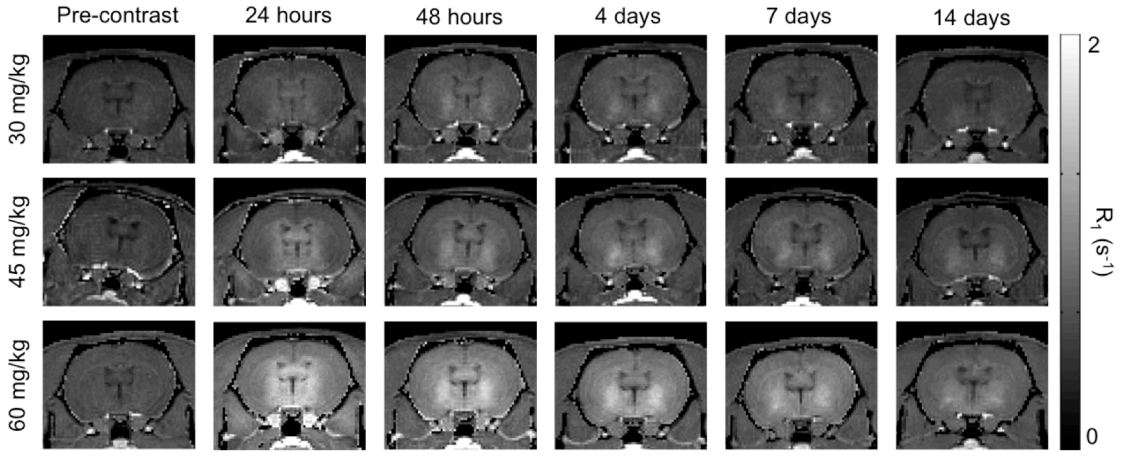

Figure 4.1: Representative coronal R_1 maps of three subjects delivered different doses of $MnCl_2$ (30, 45, and 60 mg/kg). Imaging was performed and R_1 maps were calculated prior to contrast administration and at five imaging time points over two weeks following administration. Higher contrast dose increases signal enhancement, particularly near the ventricles. Two weeks following contrast administration, signal enhancement remains, particularly in the vicinity of the striatum and globus pallidus.

regions of interest. Median R_1 rates were determined in the striatum, neocortex, olfactory bulb, corpus callosum, basal forebrain, globus pallidus, thalamus, hippocampus, hypothalamus, brain stem, cerebellum, and trigeminal tract. The maximum R_1 relaxation rate measured in each region for each dose level is shown in **Table 4.1**. Some regions, such as the neocortex, corpus callosum, basal forebrain, hippocampus, hypothalamus, and cerebellum, consistently reached maximum signal one day following contrast administration (**Table 4.1**

and **Figure 4.2**). Other regions, in particular the striatum, globus pallidus, thalamus, and brain stem, reached their maximum signal level at either 1, 2, or 4 days following contrast administration, depending on dose delivered. Together, these results indicate that up to 60 mg/kg $MnCl_2$ can be safely delivered for brain imaging between 1-4 days following contrast administration, depending on the enhancement level and brain structure(s) of interest.

$MnCl_2$ Dose	Striatum		Neocortex		Olfactory bulb		Corpus callosum		Basal forebrain		Globus pallidus	
30 mg/kg	0.711	41%	0.611	33%	0.685	54%	0.698	42%	0.697	40%	0.743	39%
45 mg/kg	0.825	70%	0.656	43%	0.736	76%	0.766	58%	0.851	65%	0.904	72%
60 mg/kg	0.899	84%	0.713	52%	0.815	121%	0.878	77%	0.939	85%	0.987	92%
	Thalamus		Hippocampus		Hypothalamus		Brain stem		Cerebellum		Trigeminal tract	
30 mg/kg	0.747	37%	0.702	49%	0.814	48%	0.800	41%	0.635	37%	0.659	48%
45 mg/kg	0.871	67%	0.768	65%	0.990	91%	0.911	59%	0.693	51%	0.732	53%
60 mg/kg	0.956	82%	0.830	74%	1.049	120%	1.088	85%	0.809	78%	0.929	90%

Table 4.1: Maximum R_1 relaxation rate (s^{-1}) reached by brain region and $MnCl_2$ dose delivered, along with corresponding percent increase in R_1 with respect to the pre-contrast measurement. Entries are color-coded by the imaging time point at which the maximum signal was reached; red = 24 hours, blue = 48 hours, green = 96 hours (4 days). No regions reached their maximum after the 96 hour imaging time point.

4.4.3 Brain uptake of ^{52}Mn measured by gamma counting

To observe brain uptake of no-carrier-added (NCA, formulated in saline) and carrier-added (CA, formulated in 66.7 mM $MnCl_2$ in saline) $^{52}Mn^{2+}$, gamma counting was performed on resected rat brains at 24 and 48 hours following contrast agent administration (N=3 per group, **Figure 4.3B**). Significant increases in $^{52}Mn^{2+}$ brain uptake were observed in subjects delivered NCA $^{52}Mn^{2+}$ compared to those delivered CA $^{52}Mn^{2+}$, by a factor of greater than 2.5 at both time points evaluated (**Figure 4.3A** and **B**, $p<0.01$). Additionally, a trend toward

approximately 30% increased uptake at 48 hours compared to 24 hours was observed for both contrast agent forms. The results of gamma counting indicate that significantly higher brain uptake of $^{52}Mn^{2+}$ is observed when administered in no-carrier-added form.

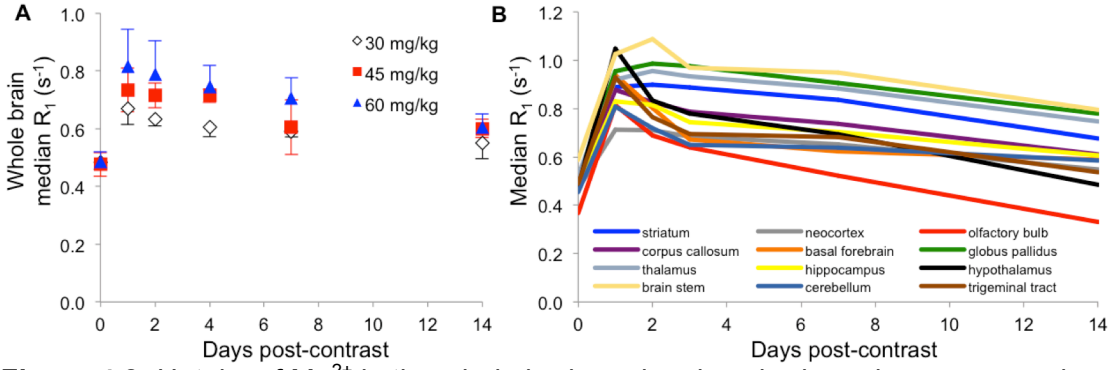

Figure 4.2: Uptake of Mn^{2+} in the whole brain and various brain regions measured with quantitative MRI. (A) Whole-brain average R_1 relaxation rate reached a maximum 24 hours following contrast administration regardless of contrast dose ranging from 30-60 mg/kg $MnCl_2$. Efflux from the brain was slow, with some enhancement remaining at the 14 day imaging time point. (B) Regional analysis of uptake of 60 mg/kg $MnCl_2$ based on registration and segmentation of brain volumes to a rat brain atlas. Some brain regions (neocortex, corpus callosum, basal forebrain, hippocampus, hypothalamus, and cerebellum) reached maximum enhancement one day following contrast administration, while others (striatum, globus pallidus, thalamus, and brain stem) in some cases reached maximum at two or four days post-

4.4.4 *In vivo* brain uptake of ^{52}Mn

In vivo full-body PET/CT was performed in five rats at various time points following administration of CA $^{52}Mn^{2+}$ (N=1) and NCA $^{52}Mn^{2+}$ (N=4). In order to examine brain uptake dynamics of the two formulations of $^{52}Mn^{2+}$, ROI-based analysis on full-body PET images was used to compare brain uptake between two subjects delivered CA and NCA $^{52}Mn^{2+}$, respectively, at multiple time points up to 7 days following administration. PET acquisition times ranged from 30-60 minutes due to the relatively long half-life of ^{52}Mn ($t_{1/2}$=5.59 days). In the subject

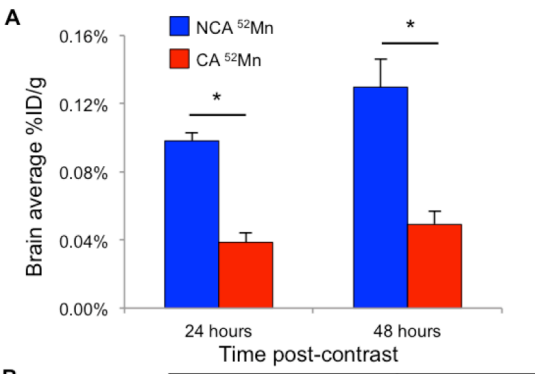

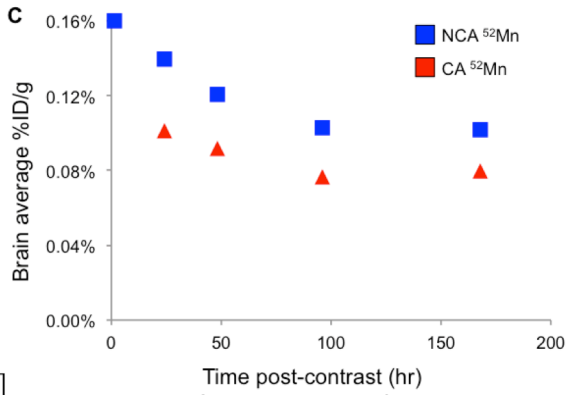

B

Brain average ^{52}Mn uptake	Average %ID/g		% increase 24 vs. 48 hr
	24 hr	48 hr	
CA ^{52}Mn	0.039	0.049	27.3%
NCA ^{52}Mn	0.098	0.130	32.1%
% increase NCA vs. CA	254% *	264% *	*p<0.01

Figure 4.3: Comparison of brain uptake of no-carrier-added (NCA) and carrier-added (CA) ^{52}Mn with *ex vivo* gamma counting and *in vivo* PET/CT. We observed higher activity uptake of NCA ^{52}Mn in both *ex vivo* gamma counting measurements of the excised brain at 24 and 48 hours (A, B) as well as *in vivo* with PET/CT for up to 7 days following contrast delivery (C). *Ex vivo* measurements are the average of 3 subjects per contrast agent formulation and time point, while *in vivo* PET/CT was performed on one subject per contrast agent formulation in this initial comparative imaging study.

delivered CA $^{52}Mn^{2+}$, brain uptake between 0.08-0.10 %ID/g was observed, with maximum uptake measured at the earliest time point (24 hours) post injection (**Figure 4.3C**). As expected, in the subject delivered NCA $^{52}Mn^{2+}$, higher brain uptake of 0.10-0.16 %ID/g was observed. Surprisingly, the maximum brain uptake was measured at 2 hours following contrast administration, rather than at 48 hours, as gamma-counting results would suggest. Notably, we observed several regions of high $^{52}Mn^{2+}$ uptake in the head and neck, including the pituitary and the submandibular gland (**Figure 4.4A**).

After observing maximum uptake of NCA $^{52}Mn^{2+}$ at the 2 hour imaging time point, we further investigated the uptake dynamics of NCA $^{52}Mn^{2+}$ in four additional subjects (**Figure 4.4**). PET/CT images were acquired at multiple time points over the course of 8 hours and at 24, 48, and 72 hours (N=3 at 72 hour

time point) following contrast administration. In these subjects, ROI-based time activity curves measurements indicated uptake of $^{52}Mn^{2+}$ in the first hour followed by a steady, slow decrease in retention over the course of 3 days (**Figure 4.4A** and **B**). In order to understand the source of the discrepancy between brain uptake dynamics with gamma counting and PET/CT imaging, ROI-based analysis of submandibular gland and pituitary uptake was also performed on all subjects. Due to high uptake in these regions, signal spillover could affect quantification of adjacent brain uptake measurements (**Figure 4.4A**). The submandibular gland exhibited an uptake over the course of 4 hours, reaching maximum uptake of 0.869 %ID/g at 4 hours following contrast administration and followed by a slow decrease over the next 72 hours (**Figure 4.4C**). Similarly, the pituitary showed maximum uptake at 4 hours, reaching 0.512 %ID/g. These signal levels corresponded to 5.3 and 3.1 times the whole-brain average uptake at that time point, respectively. Together, these results indicate that although maximum brain uptake of ^{52}Mn is measured in PET/CT 1-4 hours following administration, measurements may be skewed to higher than ground truth due to spillover effects from nearby high signal regions.

4.4.5 ^{52}Mn full-body biodistribution

Ex vivo measurements of NCA and CA $^{52}Mn^{2+}$ uptake in major organs were made at 4 and 48 hours following contrast delivery (**Figure 4.5A**). At four hours following ^{52}Mn delivery, the highest uptake of NCA $^{52}Mn^{2+}$ was observed in the kidney (3.02 %ID/g), liver (2.75 %ID/g), pancreas (1.74 %ID/g), stomach (1.50 %ID/g), and submandibular gland (1.36 %ID/g). Interestingly, unlike in

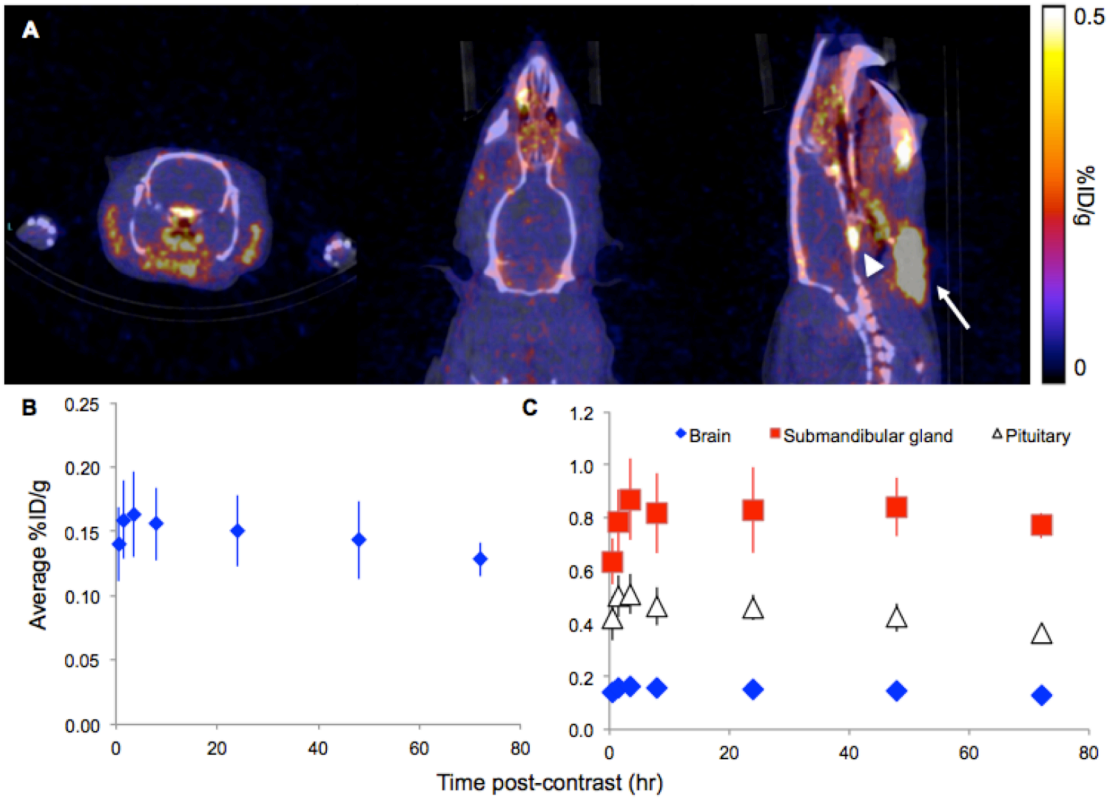

Figure 4.4: *In vivo* PET/CT of brain uptake of NCA ^{52}Mn in the rat. (A) Axial, coronal, and sagittal views of the brain (left to right, respectively) from *in vivo* PET/CT of a rat four hours following administration of no-carrier-added (NCA) ^{52}Mn. Submandibular gland = white arrow, pituitary = white arrowhead. (B) In four subjects, average brain uptake reached a maximum at four hours following contrast administration, after which a slow decrease in brain signal was observed. (C) High ^{52}Mn uptake in the submandibular glands and pituitary, up to 0.869 and 0.512 %ID/g respectively, were measured at all imaging time points.

other organs, high pancreas and submandibular gland uptake was maintained at the 48-hour time point (2.49 and 1.24 %ID/g, respectively). Intestine uptake also remained relatively consistent from 4 to 48 hours following delivery (1.00 and 0.75 %ID/g, respectively). After CA $^{52}Mn^{2+}$ delivery, the highest uptake was observed in the pancreas (1.94 %ID/g), which had approximately 2.5 times higher uptake than the next highest uptake observed in the submandibular gland (0.79 %ID/g). The uptake of CA $^{52}Mn^{2+}$ was significantly reduced compared to the uptake of NCA $^{52}Mn^{2+}$ at both time points in all organs tested with the

exception of the bone, tail blood, pancreas (significant difference at 4 hour time point only), and intestine (significant difference at 48 hour time point only) (p<0.05).

Qualitative observations of CA and NCA $^{52}Mn^{2+}$ biodistribution with *in vivo* PET/CT generally agreed with *ex vivo* biodistribution studies (**Figure 4.5B**). At 24 hours following NCA $^{52}Mn^{2+}$ delivery, high uptake was observed in the liver, kidneys, submandibular gland, gastrointestinal tract, pancreas, and spleen. At the same time point following CA $^{52}Mn^{2+}$ delivery, uptake was primarily observed in the contents of the intestinal tract and cecum as well as in the vicinity of intervertebral and synovial joints (**Figure 4.5C**). Signal persisted in the gastrointestinal tract (NCA) and joints (CA) at later imaging time points (data not shown). Increased uptake of CA $^{52}Mn^{2+}$ compared to NCA $^{52}Mn^{2+}$ was observed in synovial and intervertebral joints at all *in vivo* imaging time points. In all subjects imaged with full-body PET/CT, we observed activity pooling in the tail at the injection site to varying degrees. This was possibly caused by movement of the injection needle during the slow infusion, which lasted between 15-45 minutes depending on bulk $MnCl_2$ dose, and could be a contributor to the inter-subject variability of uptake measurements observed *in vivo*.

4.5 Discussion

In this chapter, we investigated the effects of contrast agent vehicle, dose, and acquisition time point on brain uptake and retention of Mn-based contrast agents for MRI and PET. The over-arching goal was to determine the ideal protocols for detecting $hNPC^{DMT1}$ in the rat striatum with MEMRI and ^{52}Mn PET.

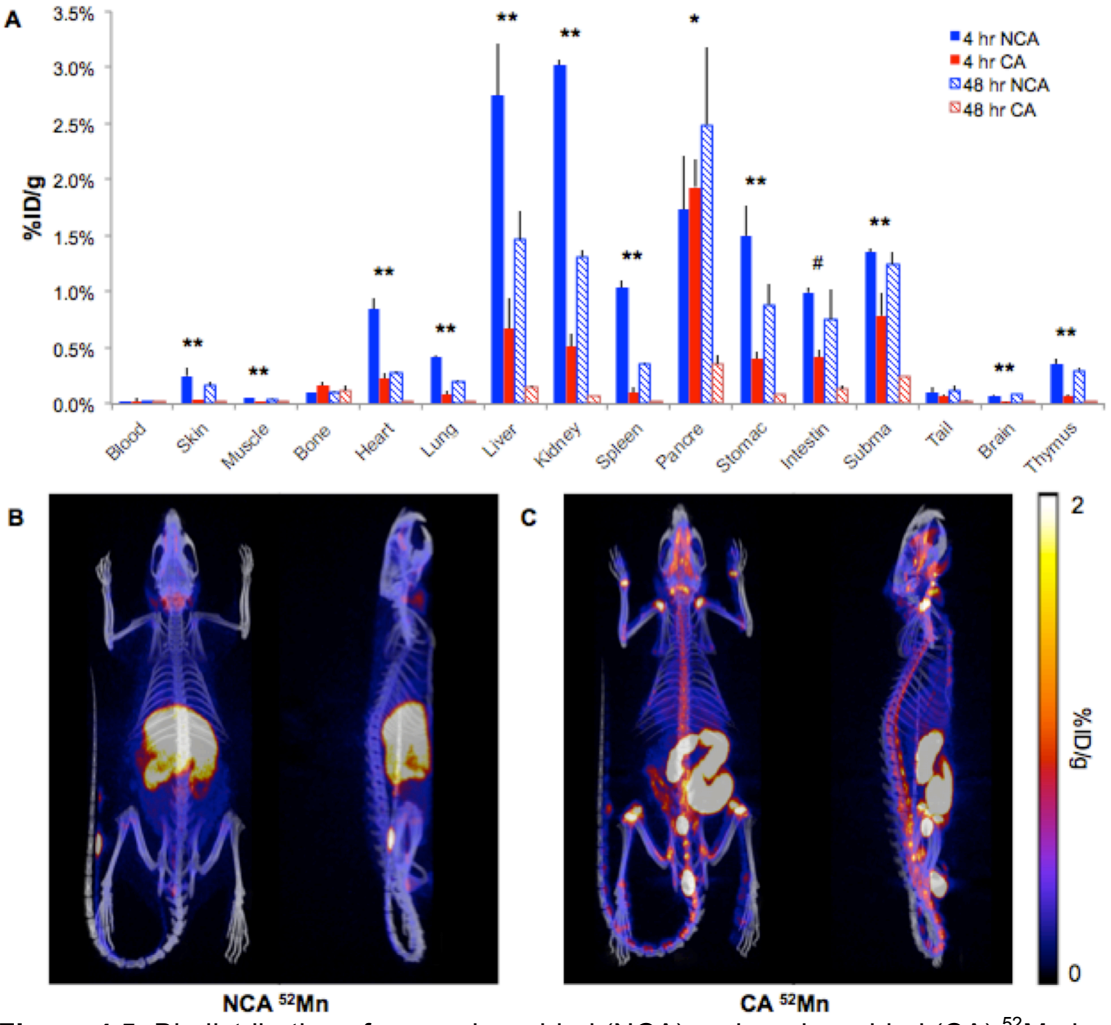

Figure 4.5: Biodistribution of no-carrier-added (NCA) and carrier-added (CA) ^{52}Mn in the rat. (A) *Ex vivo* biodistribution of NCA and CA ^{52}Mn in the rat at 4 and 48 hours following administration; N=3 per contrast agent preparation and time point. A significant increase in uptake of NCA ^{52}Mn compared to CA ^{52}Mn was observed at both time points in the majority of organs tested (**p<0.05). In the pancreas and intestine, this increase was only significant at one time point (*p<0.05 at four hours, $^{\#}p$<0.05 at 48 hours). No significant differences were observed in the blood, bone, or tail. (B-C) Representative PET/CT overlay MIPs of full-body ^{52}Mn uptake at 24 hours following contrast delivery from one subject per contrast agent formulation. (B) In the NCA subject, uptake is observed in the submandibular glands, nasal cavities, liver, kidneys, intestine, pancreas, and spleen. (C) In the CA subject, the majority of uptake is observed in the contents of the intestine and in the vicinity of the intervertebral and synovial joints.

By using a bulk $MnCl_2$ delivery protocol that utilized slow infusion while maintaining body temperature and hydration, we observed minimal behavior and health side effects, even at the highest dose tested (60 mg/kg). This result supports the methods used by other labs in rats, in which even higher total doses of 110-175 mg/kg $MnCl_2$ were delivered [110, 155]. In all measurements of Mn^{2+} uptake in this work, inter-subject variability was observed. With whole-body PET/CT, we noted activity pooled in the tail, most likely caused by the needle moving slightly during the slow 15-45 minute infusion of contrast agent. This likely occurred in all subjects to some extent, not just those imaged with PET/CT, and therefore could be one source of inter-subject variability (along with normal biological and physiological variations). For gamma counting and PET/CT studies that require trace amounts of $^{52}Mn^{2+}$, rather than large doses of bulk $MnCl_2$, a faster infusion of NCA $^{52}Mn^{2+}$ would likely be advisable. We hypothesize that this would minimize errors with needle placement, reducing the Mn^{2+} delivered to the tail rather than the blood pool and minimizing variability between subjects.

In MRI studies, we observed that greater $MnCl_2$ dose resulted in increased R_1 enhancement, in the whole brain and in a variety of individually analyzed brain regions. This maximum enhancement occurred at one day following contrast administration for the whole brain on average as well as for a majority of brain regions. The delayed maximum enhancement observed in some regions, most notably the striatum, thalamus, globus pallidus, and brain stem, may be a result of more prolonged uptake over greater than 24 hours and/or slower Mn^{2+} efflux from these brain regions. This indicates that neuroimaging studies focused on

these regions may perform favorably at these later time points due to both increased enhancement and reduced combined negative effects of bulk $MnCl_2$ administration and isoflurane anesthesia for imaging on study subjects.

The spatial pattern of R_1 enhancement observed was characterized by a small amount of generalized enhancement with increased enhancement near the ventricles. This pattern agreed with other studies that show saturable active transport of Mn^{2+} to the brain parenchyma across the BBB with additional uptake via diffusion through the blood-CSF barrier, linearly correlated with the blood concentration of Mn^{2+} [118, 162-165]. Furthermore, we observed slow reduction of Mn^{2+} in the brain, consistent with previous studies establishing diffusion as the primary efflux mechanism [118, 174].

In gamma counting studies we observed that supplementing $^{52}Mn^{2+}$ with bulk $MnCl_2$ (CA $^{52}Mn^{2+}$) resulted in reduced brain uptake by an average factor greater than two. This could be due to the fact that cold Mn^{2+} competed with $^{52}Mn^{2+}$ for Mn^{2+} transporters into the brain [118, 163]. In PET and full-body biodistribution studies, we further observed that the preparation of $^{52}Mn^{2+}$ in $MnCl_2$ solution caused reduced uptake in the majority of organs and kidney and liver excretion of much of the injected activity over the course of 4-48 hours following administration. At both 4 and 48 hours following contrast delivery, *ex vivo* biodistribution studies showed low plasma activity (<0.025 %ID/g) independent of contrast agent dose. These biodistribution results indicate that, at the contrast doses and measurement times used for biodistribution studies in this work, adding bulk $MnCl_2$ to $^{52}Mn^{2+}$ prior to delivery does not significantly increase

$^{52}Mn^{2+}$ circulation time, which was previously hypothesized as a potential method to increase overall ^{52}Mn brain uptake [33]. Interestingly, full-body PET/CT after administration of CA $^{52}Mn^{2+}$ showed increased uptake in intervertebral and synovial joints. Although this work does not focus on musculoskeletal applications of ^{52}Mn PET, this uptake pattern may be of interest to other researchers and warrants further investigation.

Regarding the timing window of maximum $^{52}Mn^{2+}$ uptake in the brain, there was a disagreement between *ex vivo* gamma counting and *in vivo* PET imaging. Gamma counting experiments of the excised brain indicated a non-significant increase in brain activity from 24 to 48 hours, while ROI-based analysis of *in vivo* PET/CT indicated maximum brain uptake within the first eight hours. Based on imaging studies in four subjects, observed maximum brain uptake 1-4 hours following NCA $^{52}Mn^{2+}$ administration. However, the ROI-based brain uptake measurements may be artificially high due to spillover from nearby high-signal regions such as the submandibular gland and pituitary. An additional source of timing discrepancy may be the inter-subject variability of ^{52}Mn delivery, which could affect the dynamics of ^{52}Mn brain uptake through saturable transporters or the blood-CSF barrier. Nevertheless, this maximum uptake of approximately 0.2% ID/g may be too low for many $^{52}Mn^{2+}$ neuroimaging applications, and alternate delivery methods such as blood-brain-barrier disruption or direct CSF delivery of $^{52}Mn^{2+}$ may be worthy of future investigation. However, in studies in which an accumulation of $^{52}Mn^{2+}$ is expected in a specific brain region of interest, such as in transplanted stem cells in the striatum,

systemic delivery may prove sufficient when the appropriate formulation and imaging time point are utilized [34].

4.6 Conclusion

MEMRI has been established as a useful preclinical neuroimaging method for observing brain tissue enhancement, neuron tract tracing, functional imaging, and stem cell detection. However, the doses required for T_1-weighted signal enhancement are prohibitive for translation of these applications. ^{52}Mn PET imaging may provide a complementary imaging method with reduced bulk Mn^{2+} dose, novel imaging characteristics, and potential applications in PET/MR. In these studies we have investigated several methods for preparation, delivery, and detection of Mn-based contrast agents with quantitative MEMRI and ^{52}Mn PET. We observed that while the whole brain and many brain regions reach maximum R_1 in MEMRI at 24 hours following $MnCl_2$ delivery, several specific sub-regions show maximum enhancement at later time points. Additionally, with PET/CT and *ex vivo* gamma counting, we observed that the supplementation of tracer doses of $^{52}Mn^{2+}$ with $MnCl_2$ reduced activity uptake in the brain and nearly all other organs, indicating that NCA $^{52}Mn^{2+}$ is the preferred vehicle for many imaging applications. These studies highlight several interesting areas of further study of ^{52}Mn PET, including investigating specific $^{52}Mn^{2+}$ uptake in the submandibular gland, pancreas, and joints as well as development of methods to increase $^{52}Mn^{2+}$ uptake in the brain. In all, these studies provide a solid foundation of knowledge regarding MEMRI and $^{52}Mn^{2+}$ PET neuroimaging protocols to aid in our effort to detect DMT1-expressing hNPC *in vivo*.

Chapter 5: Optimized flip angle selection for T_1 estimation from VFA SPGR acquisitions

5.1 Preface/Abstract

This chapter investigates and applies a method to determine optimal flip angle sets for T_1 estimation. In it, we select optimal flip angles for spoiled gradient echo (SPGR)-based T_1 mapping by minimizing propagated error in the T_1 estimate weighted by the joint density of M_0 and T_1 in an initial acquisition. The effect of optimized flip angle selection on T_1 estimate error was measured using simulations and experimental data in the human and rat brain. We found that for 2-point acquisitions, optimized angle sets were similar to those proposed by other groups, and therefore performed similarly. For multi-point acquisitions, optimal angle sets for T_1 mapping in the brain consisted of a repetition of two angles. In simulations, implementation of optimal angles reduced T_1 estimate error by up to 40% compared to a multi-point acquisition using a range of angles. Experimental data confirmed a reduction of inter-scan variance by 30%. This work shows that repetition of two carefully selected SPGR flip angles notably improves the precision of resulting T_1 estimates compared with acquisitions using a range of flip angles. This work provides a flexible and widely applicable optimization method of particular use for those who repetitively perform T_1 estimation. Therefore, for our future quantitative imaging studies in cell tracking and cancer imaging, this approach will be used for selection of optimal angles for T_1 mapping. The work described in this chapter was published in the peer-

reviewed journal *Magnetic Resonance in Medicine* in 2015 and reprinted with permission from the publisher [175].

5.2 Introduction

In the contexts of stem cell tracking and cancer imaging, along with a variety of other applications, quantitative imaging techniques are essential to maximize reproducibility and facilitate comparison between results from different subjects, experiments, and institutions. PET imaging directly measures the activity uptake in a given region, making it inherently quantitative. However, MRI contrast can vary between subjects, scanners, and on a day-to-day basis. T_1 estimation is a quantitative MRI tool with a variety of applications, including monitoring myelin-related disease, diagnosing Parkinson's disease, and studying tissue perfusion [176-178]. For stem cell tracking, T_1 mapping is particularly valuable in order to improve researchers' capabilities to detect and quantify small populations of viable cells in a small number of voxels. For targeted MR imaging of cancer, T_1 mapping can help to discern potentially small changes in tumor contrast due to the administration of a molecular targeted agent.

The gold standard for T_1 estimation is an inversion recovery sequence with multiple inversion times [179]. However, inversion recovery scans require repetition times (TRs) much longer than the longest T_1 of interest, rendering them impractical for use in clinical scans or *in vivo* research settings. For this reason, a multiple flip angle spoiled gradient echo (SPGR) approach is commonly employed to reduce scan time for T_1 mapping [180]. More recently, several researchers have proposed supplemental methods to correct for common

sources of error in resulting SPGR-based T_1 estimates, such as incomplete spoiling and imperfect RF pulses [166, 181, 182].

For SPGR-based T_1 mapping, a minimum number of flip angles must be carefully selected to maximize the accuracy and precision of the T_1 estimate and minimize scan time. Several works addressing angle selection criteria settle on the same optimal flip angles in a 2-point acquisition despite differences in selection approach. These approaches include variance minimization [183], definition of an efficiency function related to both the T_1 estimate variance and the scan time [184], and maximizing the product of the regression line dynamic range and the fractional signal with respect to the Ernst angle [153]. Another approach uses criteria of T_1-to-noise ratio maximization to select larger flip angle sets [185]. However, these approaches address T_1 estimation in the simplified setting of a single or average T_1 value. Tissues and pathologies of interest contain a continuous distribution of T_1 values, which can complicate the task of selecting optimal flip angles. Furthermore, most of these approaches address the optimized selection of just two flip angles and therefore do not develop approaches that can be generalized to the selection of larger angle sets.

The selection of flip angles for more realistic imaging tasks has also been addressed in several studies. Cheng and Wright propose selection of 3-point angle sets based on the minimum and maximum of the range of T_1 values to be estimated [186]. T_1 variance minimization has also been used to select 2-point sets for several different ranges of T_1 values to be estimated [187]. In another study, researchers selected 3-point angle sets to maximize T_1 mapping efficiency

over a realistic range of T_1 values [188]. Although useful, these approaches lack flexibility to select any number of flip angles, and they do not take into account the full shape and range of the T_1 and M_0 distributions of the anatomy being imaged.

In this study, we aim to address these missing components of flip angle selection schemes with the goal of providing a robust flip angle selection method that can be applied in almost any setting. To achieve this goal, we develop a data-driven approach based on T_1 variance minimization to determine the optimal set of any number of flip angles for T_1 estimation. The T_1 distribution in the imaging subject of interest is taken into account using an initial acquisition. We describe and apply a novel set of flip angle selection criteria, based on minimization of the variance in the T_1 estimates weighted by the joint density of M_0 and T_1. Using experimental data and simulations, we evaluate the effects of this optimized acquisition design on the precision and accuracy of T_1 estimates. The concepts behind the proposed method were previously described in abstract form [189].

5.3 Theory

In the general setting of nonlinear least squares-based (NLS) parameter estimation, as is used for T_1 and M_0 estimation in this work, the objective function can be represented by

$$f_{NLS}(\gamma) = \frac{1}{2}\sum_{i=1}^{n} r_i(\gamma)^2 \qquad [1]$$

where γ is the parameter vector to be estimated and $r_i(\gamma)$ are the error terms or the residual terms if r_i are evaluated at the NLS estimate. Defining $r = [r_1\ r_2\ \ldots\ r_n]^T$, the gradient vector and the Hessian matrix of $f_{NLS}(\gamma)$ can be expressed respectively as

$$\nabla_\gamma f_{NLS}(\gamma) = \boldsymbol{J}_\gamma^T(\boldsymbol{r}) \cdot \boldsymbol{r} \quad [2]$$

and

$$\nabla_\gamma^2 f_{NLS}(\gamma) = \boldsymbol{J}_\gamma^T(\boldsymbol{r}) \cdot \boldsymbol{J}_\gamma(\boldsymbol{r}) + \sum_{i=1}^{n} r_i \boldsymbol{T_i} \quad [3]$$

where $[\boldsymbol{T}_i]_{kl} = \partial^2 r_i / \partial\gamma_k \partial\gamma_l$ is the second order derivative of the residual term, and the Jacobian matrix is defined as $\left[\boldsymbol{J}_\gamma(\boldsymbol{r})\right]_{ij} \equiv \partial r_i / \partial\gamma_j$. According to the framework of error propagation [190], the covariance matrix of the estimated parameter can be written as

$$\boldsymbol{\Sigma}_\gamma = \sigma^2 \left[\nabla_\gamma^2 f_{NLS}(\gamma)\right]^{-1} \quad [4]$$

where σ^2 is the unknown noise variance. However, in a computational experimental design setting, the covariance matrix takes a much simpler form:

$$\boldsymbol{\Sigma}_\gamma = \sigma^2 \left[\boldsymbol{J}_\gamma^T(\boldsymbol{r}) \boldsymbol{J}_\gamma(\boldsymbol{r})\right]^{-1} \quad [5]$$

because the residual terms are assumed to be zero on the average. This assumption is based on that of Gaussian-distributed noise contributing to residuals that average to zero and are independent of the parameters of interest.

In the setting of T_1 estimation, the appropriate term of this covariance matrix can be used to define an objective function for minimization of variance in the NLS-based T_1 estimate. The NLS objective function for T_1 estimation from variable flip angle SPGR acquisitions can be written as

$$f_{NLS}(\gamma) = \frac{1}{2}\sum_{i=1}^{n}\left(s_i - M_0 \sin(\alpha_i)\frac{1 - e^{-TR/T_1}}{1 - \cos(\alpha_i)e^{-TR/T_1}}\right)^2 \quad [6]$$

where s_i are the observed signals, α_i are the flip angles, M_0 is the unknown equilibrium longitudinal magnetization, TR is the repetition time, and T_1 is the unknown longitudinal relaxation time. Therefore, $\gamma=[M_0\ T_1]^T$. We note here that repetition time is held constant and held close to the minimum allowable by the MR system, echo time (TE) is similarly held close to the practical minimum, and therefore differences in T_2* decay are assumed negligible for this specific setting.

Taking the derivative of the error with respect to both M_0 and T_1, we arrive at the expressions for the terms in the Jacobian matrix:

$$\frac{\partial r_i}{\partial \gamma_1} \equiv \frac{\partial r_i}{\partial M_0} = -\sin(\alpha_i)\frac{1 - e^{-TR/T_1}}{1 - \cos(\alpha_i)\, e^{-TR/T_1}} \quad [7]$$

and

$$\frac{\partial r_i}{\partial \gamma_2} \equiv \frac{\partial r_i}{\partial T_1} = \frac{M_0 TR}{T_1^2}\frac{(1 - \cos(\alpha_i))\sin(\alpha_i)e^{-TR/T_1}}{(1 - \cos(\alpha_i)\, e^{-TR/T_1})^2} \quad [8]$$

With some algebraic manipulation, as shown in Appendix 2, the determinant of $\boldsymbol{J}_\gamma^T(\boldsymbol{r})\boldsymbol{J}_\gamma(\boldsymbol{r})$ and the components of the covariance matrix $\boldsymbol{\Sigma}_\gamma$ can be expressed as

$$\det\left(\boldsymbol{J}_\gamma^T(\boldsymbol{r})\boldsymbol{J}_\gamma(\boldsymbol{r})\right) = \frac{E^2(E-1)^3 TR^2 M_0^2}{T_1^4}\sum_{i=1}^{n}\sum_{j=1}^{n} A_{ij} \quad [9]$$

$$\left[\boldsymbol{\Sigma}_\gamma\right]_{11} = \frac{\sigma^2}{(E-1)^3}\frac{\sum_{i=1}^{n}\frac{\sin^2(\alpha_i)(1-\cos(\alpha_i))^2}{(E-\cos(\alpha_i))^4}}{\sum_{i=1}^{n}\sum_{j=1}^{n} A_{ij}} \quad [10]$$

$$\left[\boldsymbol{\Sigma}_{\gamma}\right]_{22} = \frac{\sigma^2 T_1^4}{E^2(E-1)TR^2M_0^2} \frac{\sum_{i=1}^{n} \frac{\sin^2(\alpha_i)}{(E-\cos(\alpha_i))^2}}{\sum_{i=1}^{n}\sum_{j=1}^{n} A_{ij}} \quad [11]$$

$$\left[\boldsymbol{\Sigma}_{\gamma}\right]_{12} = \left[\boldsymbol{\Sigma}_{\gamma}\right]_{21} = \frac{\sigma^2 T_1^2}{E(E-1)^2 TRM_0} \frac{\sum_{i=1}^{n} \frac{\sin^2(\alpha_i)(1-\cos(\alpha_i))}{(E-\cos(\alpha_i))^3}}{\sum_{i=1}^{n}\sum_{j=1}^{n} A_{ij}} \quad [12]$$

where $A_{ij} = \frac{\sin^2(\alpha_i)\sin^2(\alpha_j)(1-\cos(\alpha_j))(\cos(\alpha_i)-\cos(\alpha_j))}{(E-\cos(\alpha_i))^3(E-\cos(\alpha_j))^4}$ and $E = \exp(TR/T_1)$. Note that $[\boldsymbol{\Sigma}_{\gamma}]_{11}$, $[\boldsymbol{\Sigma}_{\gamma}]_{22}$, and $[\boldsymbol{\Sigma}_{\gamma}]_{21}$ are the variance of M_0, the variance of T_1, and the covariance of M_0 and T_1, respectively. A similar derivation for the T_1 estimate variance, along with the analytical result for the two-angle T_1 estimate, has previously been published by Wood [191].

5.4 Methods

5.4.1 Study design

In order to test the described T_1 variance minimization criteria for SPGR flip angle selection, we pursued following approach. First, an objective function for flip angle selection was defined based on minimizing T_1 variance in the imaging volume of interest. Second, optimal flip angle sets and control flip angle sets were defined based on T_1 and M_0 maps calculated from an open-source IR data set in the human brain. Using these T_1 and M_0 maps as ground truth, simulations were performed to compare the relative performance of several flip angle sets for SPGR-based T_1 estimation. Third, the proposed flip angle selection technique was tested in the *ex vivo* rat brain both with simulations and experimentally. Using an initial IR acquisition and resulting T_1 and M_0 maps, optimal flip angle sets and alternate flip angle sets were defined. To compare the

performance of these flip angle sets, simulations were performed using IR-based T_1 and M_0 maps as ground truth. Last, experimental data was again acquired in the *ex vivo* rat brain using data-driven flip angle sets in order to compare the inter-scan variance when different angle sets were used.

5.4.2 Flip angle selection

In an NLS fitting problem, the covariance matrix of the parameters for estimation (in this case, M_0 and T_1) is given by the inverse of the Hessian matrix multiplied by the unknown noise variance, as described above. Therefore, assuming a constant noise variance σ^2 in the voxels of interest (i.e., those representing the tissue in which T_1 will be estimated), a single term from the inverse of the Hessian can be used to estimate the variance in the T_1 estimate at each voxel, given by $\sigma_{T_1}^2 \propto \left[\boldsymbol{\Sigma}_\gamma\right]_{22}$.

The selection of the two optimal flip angles for T_1 estimation was guided by the goal to minimize the variance in the T_1 estimate. Therefore, an objective function for flip angle selection, Ω, was defined according to the equation

$$\Omega = \sum_{All\ M_0,T_1} \sigma_{T_1}^2 P(M_0, T_1) \qquad [13]$$

where $P(M_0, T_1)$ is the smoothed joint probability density estimate of M_0 and T_1 over the imaging volume or region of interest. To select optimal flip angles for any imaging setting, this objective function was minimized using the user inputs of TR, number of desired flip angles (N_α), and $P(M_0, T_1)$. While TR and N_α can be selected based on the constraints of the imaging setting and time available, $P(M_0, T_1)$ is more complicated to provide. In this work, we pursue a data-driven approach in which $P(M_0, T_1)$ is estimated from an initial set of T_1 and M_0 maps

based on a non-optimized SPGR acquisition. For all optimized flip angle sets in this work, $P(M_0, T_1)$ was specified using the subset of image voxels in the brain tissue.

5.4.3 T_1 estimation

In both simulations and analysis of experimental data, an estimate for T_1 and M_0 in each voxel was obtained using the Levenberg-Marquardt approach for non-linear least squares fitting [192] with the goal of minimizing the objective function in Eq. 6. It should be noted that the above nonlinear least squares fitting problem can also be reformulated as a simple iterative linear fitting problem [167]. For experimental data, a calculated B_1 map was taken into account in the parameter estimation procedure [166]. This correction was used due to the variability of the relationship between nominal and actual flip angle and the potentially significant effect thereof on T_1 estimation. Iterations were continued until the step size between successive estimates was extremely small ($<10^{-15}$), the objective function was appropriately small ($<10^{-6}$), or after 500 iterations. All image processing, simulations, and computational work was performed in Matlab R2014b (The MathWorks, Natick, MA).

5.4.4 Simulations

Simulations were performed to evaluate the precision and accuracy of T_1 mapping with the flip angles selected as described above. They were also used to compare these results with those obtained using previously proposed flip angle sets and selection techniques [153, 185]. Using inversion recovery data from the Quantitative MRI Analysis Package (QMAP,

http://www.medphysics.wisc.edu/~samsonov/qmap/), FSL's Brain Extraction Tool [193], and FMRIB's Linear Image Registration Tool [168, 169], T_1 and M_0 maps in the human brain were calculated and used as ground truth. From these maps, optimal flip angles were determined as described above. For comparison of the 2-point angle set, flip angle sets were selected using Deoni and colleague's 2-point selection criteria based on the mean T_1 in the segmented human brain [153]. For comparison of the 10-point angle set, two other flip angle sets were selected. One of these sets was based on repetition of the 2-point set described above (referred to as "10-point repeat"). The other set of angles, referred to as "10-point range," is based on a previously proposed optimal 10-angle set for T_1 mapping in the human brain that covers a range of angles, which is a common approach to T_1 mapping with VFA SPGR [185, 194, 195]. The "10-point range" set was selected in order to determine the impact of using a repetition of two carefully selected flip angles compared to a range of flip angles. The flip angle sets used in simulations are shown in **Table 5.1**.

Table 5.1

Flip angle sets used in simulations and experiments of SPGR-based T_1 estimation

Optimal angle set	Human Simulation	Rat Simulation	Rat Experimental
$N_\alpha = 2$	4.7°, 27.2°	3.6°, 21.7°	Not tested
$N_\alpha = 10$	5×4.7°, 5×27.2°	5×3.6°, 5×21.7°	5×3.2°, 5×18.6°
Control angle set			
$N_\alpha = 2$	5.1°, 30.0°	4.8°, 27.1°	Not tested
$N_\alpha = 10$ repeat	5×5.1°, 5×30.0°	5×4.8°, 5×27.1°	5×3.5°, 5×19.8°
$N_\alpha = 10$ range	2°, 3°, 4°, 5°, 7°, 9°, 12°, 14°, 16°, 18°	2°, 3°, 4°, 5°, 7°, 9°, 12°, 14°, 16°, 18°	2°, 3°, 4°, 5°, 7°, 9°, 12°, 14°, 16°, 18°

In simulations of SPGR acquisition, the signal in each voxel was calculated according to the SPGR signal equation included in Eq. 6. Noisy MR signals were modeled to follow a Rician distribution. Noise was added according

to the model $S_N = \sqrt{(S + \varepsilon_1)^2 + {\varepsilon_2}^2}$, where S is the signal magnitude and ε_1 and ε_2 are random values from a normal distribution of mean zero and standard deviation dependent upon S and user-defined signal-to-noise ratio (SNR). Noisy signals were calculated in 500 realizations, and T_1 and M_0 were estimated as described above. Results were used to calculate the bias and variance of the SPGR-based T_1 estimates. The relative performance of optimal flip angles compared to other flip angle sets was measuring at 6 SNR values ranging from 5 to 40. Simulations were similarly performed using IR-based T_1 and M_0 maps in the *ex vivo* rat brain as the ground truth, using the flip angle sets shown in **Table 5.1**.

5.4.5 MR imaging

Imaging experiments were performed on a 4.7T small animal scanner (MRBR 4.7T/310, Agilent Technologies, Santa Clara, CA) with a quadrature volume RF coil for signal transmission and reception. An *ex vivo* rat brain was scanned because it has a continuous distribution of T_1 and M_0 values, as would be expected in a human subject. A 3D SPGR pulse sequence was performed using three individual flip angle sets, shown in **Table 5.1**. Each flip angle set was repeated three times to measure experimental variance in T_1 estimates. To minimize scan time and maximize the MR signal collected, the TR and TE were minimized and had values of 9.08 ms and 3.81 ms, respectively. Other scan parameters were as follows: matrix size = 128 × 128 × 128, slab size = 30 mm × 20 mm × 20 mm, total scan time = 2 min 31 s per FA. (For clarity, in experiments with more than one acquisition at each FA, each acquisition is referred to as an

individual FA rather than an additional average.) A flip angle map was acquired using an actual flip-angle imaging SPGR scan with scan parameters as follows: TR1/TR2 = 5.9/29.5 ms, TE = 2.22 ms, α = 55°, matrix size = 64 × 64 × 64 [166].

To calculate a T_1 map in the *ex vivo* rat brain for simulations, an IR acquisition was used. A set of 2D spin-echo scans was acquired at a range of 8 inversion times between 8 and 4000 ms. Other scan parameters were held constant and were as follows: TR = 6 s, TE = 13.82 ms, NEX = 4, matrix size = 128 × 128, in-plane FOV = 20 × 20 mm, with 50 slices of 0.5 mm thickness.

5.5 Results

5.5.1 Selection of optimal flip angles

It was found that the optimal flip angles for minimizing T_1 variance were, as expected, dependent upon the joint T_1 and M_0 distribution in the region of interest. Using the proposed flip angle selection approach, any number of optimal flip angles specific to reducing T_1 variance in the ROI used to define $P(M_0, T_1)$ could be determined. A representative set of parameter maps used for input to the flip angle selection algorithm is shown in **Figure 5.1A-B**. The resulting smoothed joint density function of T_1 and M_0 in the human brain is shown in **Figure 5.1C**. Finally, the objective function for selection of two flip angles is plotted in **Figure 5.1D**, and agrees well with the expected shape shown in previous works addressing selection of 2-angle sets [153, 183, 184, 187]. In the limit of a single T_1 value in the region used to define $P(M_0, T_1)$, the proposed flip angle selection approach resulted in the same two recommended angles as the approach proposed by Deoni and colleagues [153].

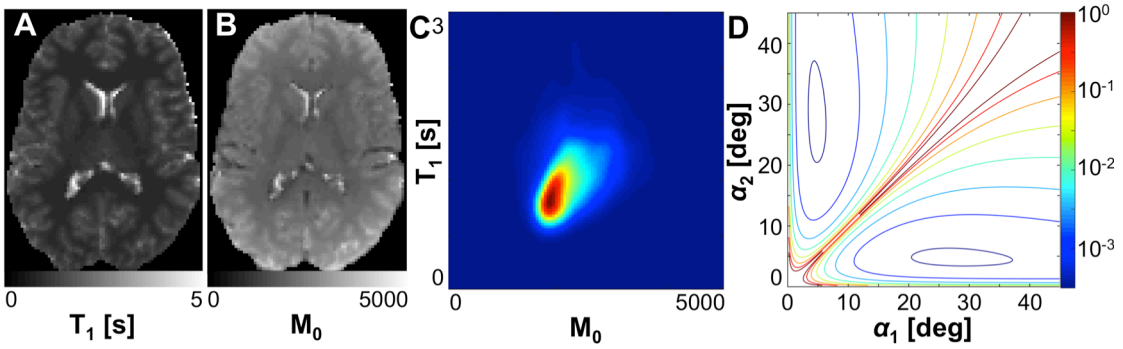

Figure 5.1: Representative input to flip angle selection algorithm. Initial estimates of (A) T_1 map and (B) M_0 map in the human brain based on IR acquisition. (C) Joint density distribution of T_1 and M_0 based on the maps in (A) and (B). (D) Flip angle minimization objective function, shown here for 2 flip angle selection for the purposes of visualization.

For even-numbered flip angle sets greater than two, it was found that the optimal flip angle sets were repetitions of the pair of two optimal flip angles. For odd-numbered flip angle sets greater than two, it was found that the optimal flip angle sets were repetitions of two angles. Interestingly, the specific angles varied based on the number of flip angles. **Table 5.2** shows the specific flip angle sets selected for different set sizes using the human brain to define the smoothed joint density of T_1 and M_0 as algorithm input. It is important to note that, particularly for selection of an odd number of flip angles, local minima were present in the objective function landscape. In these cases, optimal angles were selected based on inputting several different initial points for the minimum search and selecting optimal angles that corresponded to the minimum of the objective function that was found. For odd-numbered angle sets, two local minima with the same objective function values were found (see **Table 5.2**). Generally, the angle selection algorithm selected erroneous local minima in the case of an unreasonable search input.

Table 5.2
Representative optimal flip angle sets with varying flip angle set sizes. From this list, even-numbered sets were used in human simulations. Odd-numbered sets are included to illustrate typical results of the flip angle selection algorithm.

Flip angle set size	α_1	α_2	α_3	α_4	α_5	α_6	α_7	α_8	α_9	α_{10}
2	4.7°	27.2°								
3	4.9°	28.9°	28.9°							
3	4.0°	4.0°	24.1°							
4	4.7°	4.7°	27.2°	27.2°						
5	4.7°	4.7°	27.7°	27.7°	27.7°					
5	4.2°	4.2°	4.2°	24.9°	24.0°					
6	4.7°	4.7°	4.7°	27.2°	27.2°	27.2°				
8	4.7°	4.7°	4.7°	4.7°	27.2°	27.2°	27.2°	27.2°		
10	4.7°	4.7°	4.7°	4.7°	4.7°	27.2°	27.2°	27.2°	27.2°	27.2°

5.5.2 Simulations

To test the effect of using the proposed angle sets on the variance and bias in T_1 estimates, simulations were performed using IR-based T_1 and M_0 maps of a human brain and an *ex vivo* rat brain as digital phantoms. These parameter maps were also used as input to the angle selection algorithm for definition of $P(M_0, T_1)$. Simulation results were used to calculate the bias, variance, and root mean squared error (RMSE) of the SPGR-based T_1 estimate.

In human simulations using 2-angle estimates, it was found that optimized angles had very slightly improved performance compared to Deoni angles and greatly improved performance compared to arbitrarily selected angles. The improvement in performance at all SNR values, with the exception of SNR = 30, was measured by a root mean squared error (RMSE) reduction of 0.40 – 3.10%. The percent reduction in RMSE was greater at lower SNR values, indicating that the proposed method resulted in improved performance particularly for low SNR settings. In simulations using 10-angle acquisitions for T_1 estimation, it was found

that optimized angles had improved performance compared to the 10-point range set (**Figure 5.2**). This improvement was measured by a reduction in T_1 estimate RMSE of 42% at all SNR values. However, optimal angles had similar performance to the 10-point repeat set, again with relative performance independent of SNR. The RMSE in human brain T_1 estimates calculated for all SNR values and angle sets are shown in **Table 5.3**.

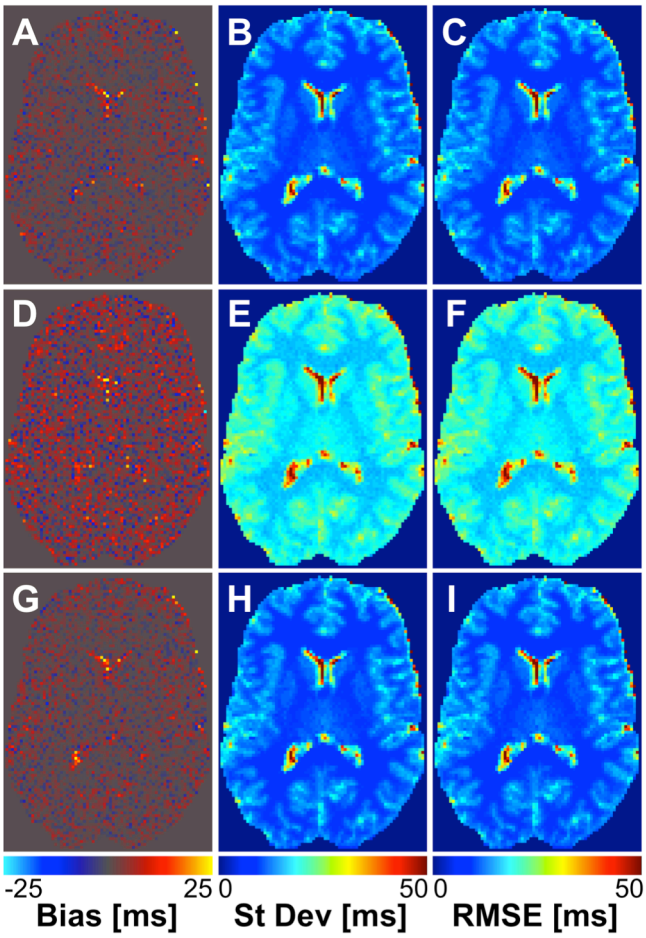

Figure 5.2: T_1 bias (A, D, G), standard deviation (B, E, H), and RMSE (C, F, I) maps based on simulations of T_1 mapping in the human brain using 10-angle acquisitions at SNR = 20. A-C correspond to simulation results using the 10 angles selected with our proposed method; D-F correspond to results using the 10-point range angle set; G-I correspond to results using a the 10-point repeat set. All measurements are in units of ms.

Simulations were also used to compare the relative performance of 2-, 4-, 6-, 8-, and 10-point acquisitions for T_1 estimation (angle sets listed in Table 2). As shown in **Figure 5.3**, increasing the number of flip angles used for acquisition

reduces the RMSE in the T_1 estimate primarily by reducing variance. It should be noted that this is equivalent to increasing the number of averages at 2 optimal flip angles. Variance was the primary contributor to RMSE, as evidenced by estimate standard deviation ranging from 20-50 times greater than estimate bias at the range of SNR used in these simulations (**Table 5.4**).

Table 5.3
Results of simulations in the human brain. The RMSE in T_1 estimates (units of s) are given for each angle set and SNR. RMSE % change is in comparison to optimal angle set for that same number of flip angles.

	N_α = 2			N_α = 10				
SNR	Optimal angle set	Control angle set		Optimal angle set	10-point repeat		10-point range	
	RMSE	RMSE	% change	RMSE	RMSE	% change	RMSE	% change
5	5.94E-1	6.13E-1	+3.20	2.15E-1	2.17E-1	+0.93	3.74E-1	+74.0
10	2.50E-1	2.51E-1	+0.40	1.07E-1	1.07E-1	--	1.87E-1	+74.8
15	1.62E-1	1.63E-1	+0.62	7.13E-2	7.13E-2	--	1.24E-1	+73.9
20	1.21E-1	1.21E-1	--	5.36E-2	5.36E-2	--	9.33E-2	+74.1
30	8.02E-2	8.00E-2	-0.25	3.57E-2	3.57E-2	--	6.21E-2	+73.9
40	6.00E-2	6.00E-2	--	2.68E-2	2.68E-2	--	4.66E-2	+73.9

Table 5.4
Effect of number of flip angles on bias, standard deviation, and RMSE of resulting T_1 estimates (all measures in units of s). Results are based on simulations in the human brain with an SNR of 20 and using flip angle sets listed in Table 2. Percent change in RMSE is compared to that of the N_α = 2 estimate.

	N_α = 2	N_α = 4	N_α = 6	N_α = 8	N_α = 10
Bias	5.77E-3	2.75E-3	1.92E-3	1.39E-3	1.13E-3
Standard Deviation	1.21E-1	8.52E-2	6.92E-2	5.98E-2	5.36E-2
RMSE	1.21E-1	8.52E-2	6.92E-2	5.98E-2	5.36E-2
RMSE % change		-29.4	-42.7	-50.5	-55.6

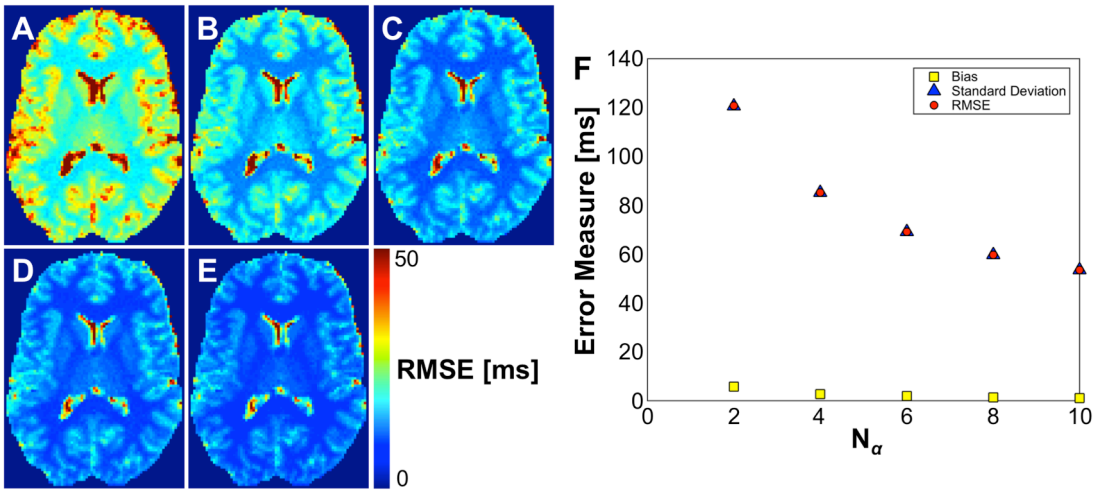

Figure 5.3: (A-E) RMSE in T_1 estimates from simulations of 2, 4, 6, 8, and 10-angle SPGR acquisitions, respectively. (F) Bias, standard deviation, and RMSE in T_1 estimates plotted versus number of acquisition flip angles. The estimate variance is the primary contributor to T_1 estimate error. All measurements are in units of ms.

In 2-point *ex vivo* rat brain simulations, it was found that optimized angles only slightly improved performance (RMSE reduction of 2.37%) at the lowest SNR value. At higher SNR values, Deoni angles out-performed optimized angles, with an RMSE reduction of 2.22 – 3.05%. These results confirm results in human simulations that our angle selection method performs most strongly in low-SNR scenarios. For 10-angle estimates, it was found that optimized angles had improved performance compared to the 10-point range angle set, reflected in an RMSE reduction of approximately 38% at all SNR values. Compared to the 10-point repeat angle set, optimized angles had slightly worse performance, independent of SNR. *Ex vivo* rat brain simulation results are shown in **Table 5.5**.

5.5.3 Experimental T_1 mapping

To test the impact of implementing optimal angles in an experimental scanning scenario, an *ex vivo* rat brain was scanned first using the 10-point range angle set. The resulting estimated T_1 and M_0 maps were used to define $P(M_0, T_1)$ in the

rat brain, and from this, optimal angle sets and control angle sets were selected (**Table 5.1**). The rat brain was then scanned again using these data-driven angle sets. To observe the effect of acquisition flip angles on the variance of T_1 estimates, scan protocols for T_1 mapping were repeated three times in order to calculate the experimental variance in the T_1 estimate. T_1 standard deviation maps for the three angle sets used (10-point range, optimal 10-point, and 10-point repeat) are shown in **Figure 5.4A-C**.

Table 5.5
Results of simulations in the rat brain. The RMSE in T_1 estimates (units of s) are given for each angle set and SNR. RMSE % change is in comparison to optimal angle set for that same number of flip angles.

	N_α = 2			N_α = 10				
SNR	Optimal angle set	Control angle set		Optimal angle set	10-point repeat		10-point range	
	RMSE	RMSE	% change	RMSE	RMSE	% change	RMSE	% change
5	1.93E-1	1.98E-1	+2.59	7.31E-2	7.16E-2	-2.05	1.20E-1	+64.2
10	8.47E-2	8.29E-2	-2.13	3.66E-2	3.56E-2	-2.73	5.94E-2	+62.3
15	5.54E-2	5.40E-2	-2.53	2.44E-2	2.37E-2	-2.87	3.96E-2	+62.3
20	4.13E-2	4.01E-2	-2.91	1.83E-2	1.77E-2	-3.28	2.97E-2	+62.3
30	2.74E-2	2.66E-2	-2.92	1.22E-2	1.18E-2	-3.28	1.99E-2	+63.1
40	2.05E-2	1.99E-2	-2.93	9.14E-3	8.87E-3	-2.95	1.49E-2	+63.0

The mean inter-scan standard deviation in the T_1 estimate was measured to be 73.3 ms when data were acquired using the 10-point range angle set. This standard deviation decreased to 61.2 ms when using the optimal flip angle set (N_α = 10). Interestingly, a slight additional decrease in inter-scan standard deviation, to 59.0 ms, was observed when data were acquired with the 10-point repeat angle set based on Deoni and colleagues' criteria for selection of two flip angles [153]. Therefore, use of flip angle sets in which two carefully selected flip angles were each repeated 5 times reduced inter-scan T_1 estimate standard

deviation in the rat brain by 16-20% when compared with the 10-point range angle set (variance reduction of 30-35%). Notably, the angle sets composed of a repeat of two angles selected using Deoni and colleagues' criteria out-performed those selected using our variance minimization objective function in terms of inter-scan variance reduction.

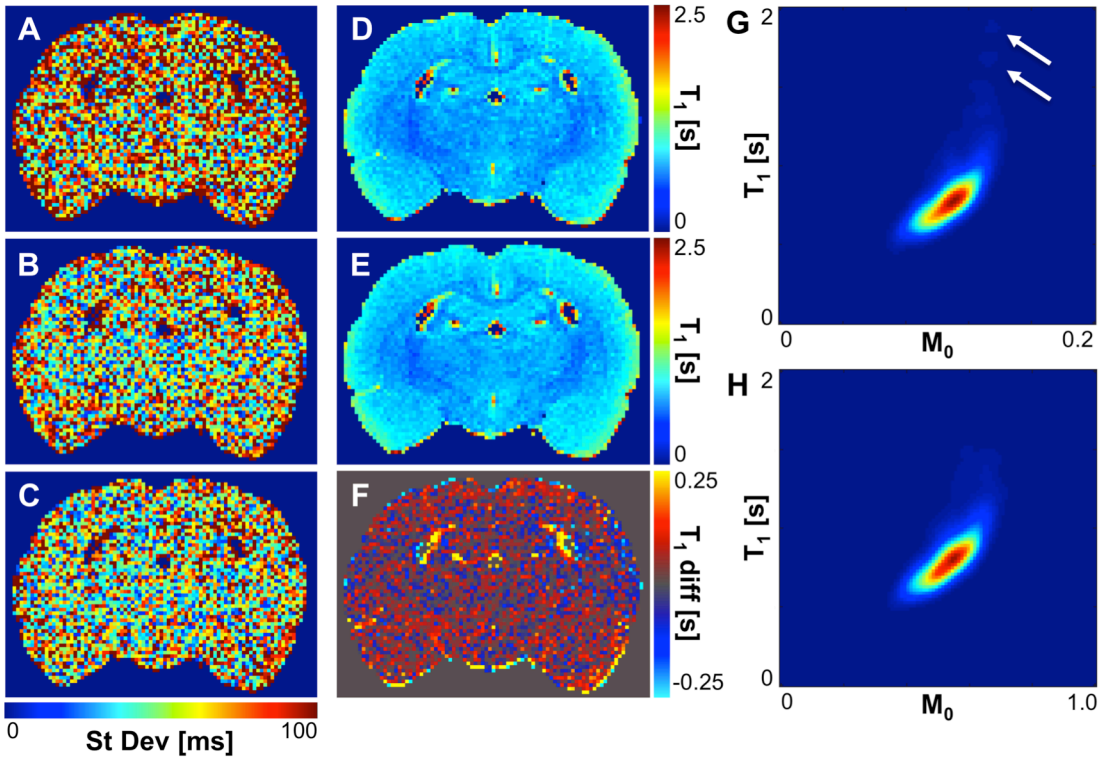

Figure 5.4: Effect of optimal flip angle selection in experimental T_1 mapping. Maps of inter-scan standard deviation in T_1 show reduced variation when the 10-point optimal angle set (b) or 10-point repeat angle set (c) is used compared to the 10-point range angle set (a). See Table 1 for specific angle sets used for acquisition. T_1 maps of the rat brain (c) prior to flip angle optimization and (d) after flip angle optimization (10-point optimal angle set) show an increase in the average T_1 estimate in the rat brain by 15.8 ms, more easily observable in (e) the T_1 difference map (difference = optimal – 10-point range). Smoothed joint density functions of T_1 and M_0 (f) prior to and (g) following flip angle optimization also show this slight shift, along with the elimination of a small population of voxels with high initial T_1 estimates (T_1 > 1.5 s, white arrows). (T_1 map, difference map, and $P(T_1, M_0)$ are not shown for the 10-point repeat angle set because results are nearly identical to those for the 10-point optimal angle set under visual inspection.)

T_1 mapping results showed that T_1 estimates in the rat brain were, on average, 15.8 ms higher when estimated using the optimized flip angles rather than the range of flip angles, as shown in **Figure 5.4D-F** ($P < 0.0001$). When estimated using the 10-angle repeat set, T_1 estimates were, on average, 24.3 ms higher than the range of flip angles ($P < 0.0001$). The difference of 8.5 ms between the 10 optimal angles and 10 angle repeat set was also found to be significant ($P < 0.0001$). Estimation of the smoothed joint density function of T_1 and M_0 from pre- and post-optimization acquisitions (**Figure 5.4G-H**) also showed a slight shift of the mean T_1 estimate in the rat brain toward higher T_1 values when optimized angles were used. Elimination of a small population of voxels with high, outlying T_1 estimates ($T_1 > 1.5$ s) was also observed.

5.6 Discussion

In this work, we have proposed and evaluated a new data-driven method for selection of SPGR flip angles for T_1 estimation. In the proposed angle selection method, we aimed to provide increased flexibility compared to previously developed approaches. This flexibility is particularly beneficial (1) to select any number of acquisition flip angles based on available scan time and (2) to select flip angles when the T_1 distribution of interest is non-Gaussian and is therefore not well-described by the mean of the distribution.

In selecting multi-point optimal flip angle sets in two settings, the human brain and the rat brain, we found that the optimal flip angle set consisted of the repetition of two optimal angles. This is in disagreement with the common practice of acquiring data at a range of flip angles to cover a wide range of the

SPGR signal curve [185, 194, 195]. Instead, it more strongly agrees with Deoni and colleagues' 2-point angle selection method, which maximizes the product of the dynamic range and the fractional signal of the acquired data [153, 191]. It is also in agreement with a previous study confirming improved T_1 mapping performance when using a small set of carefully selected flip angles over a larger set covering a range of angles [186].

Simulations testing these optimized angle sets showed very similar RMSE performance when comparing two optimized angles to two angles selected with Deoni and colleagues' criteria. For greater than two angles, simulations also show that a repetition of two carefully selected flip angles has significantly improved performance compared to using a range of angles. However, our simulations assumed perfect RF coil performance in which nominal and actual flip angle match exactly. In a true scanning scenario, the relationship between of nominal and actual flip angle can vary greatly, and system-specific RF performance should be considered when optimizing scan protocol [186]. This could be achieved by scaling the optimal flip angles according to the expected RF performance or by adjusting flip angle sets to cover a small range close to the optimal angles within the expected range of flip angle variation.

Simulations further elucidated the relative performance of different flip angle sets with respect to both bias and variance. As shown in Figure 3f, variance contributed relatively much more (20-50×) than bias to the RMSE of the T_1 estimate. This supports the work in our group and others in which flip angle selection is guided by an objective of T_1 variance minimization. When studying

the effect of using optimal flip angles experimentally, we indeed found that T_1 variance was reduced by 30% when compared to T_1 estimated from SPGR acquisitions at a range of angles. These simulations also agreed with previous work showing that T_1 estimates from VFA SPGR acquisitions tend to have positive bias when compared with the gold standard IR-based estimation approach [179].

Experimental measurement of inter-scan variance using three different 10-point acquisition angle sets showed that the use of a repetition of two thoughtfully selected flip angles indeed reduced estimate variability when compared to an acquisition using a more broad range of angles. The out-performance of our proposed optimal flip angle set by the 10-point repeat angle set could be due to imperfect RF performance, which in our scans caused actual flip angles to be approximately 80% of the nominal prescribed flip angles. This reduction would cause the two angles in the 10-point repeat set to be closer in magnitude to the intended optimal angles. The effects of this imperfect RF performance on the variability in T_1 estimates further emphasizes that it is an important consideration in the design of SPGR-based T_1 mapping experiments.

Based on these simulation and experimental results, the application of this flip angle selection technique to T_1 mapping in research and clinical settings could notably reduce variance in T_1 estimates if used in place of a set consisting of a range of flip angles. However, in many situations, the implementation of such an algorithm may be excessively complicated to incorporate into experimental design. In the imaging settings similar to those presented in this paper, in which

T_1 distributions approach a Gaussian shape, we suggest that it would be as effective and much simpler to use Deoni and colleagues' criteria for selection of two flip angles based on the mean T_1 in the volume of interest. If time allows for additional data collection or increased SNR is desired, these two angles should be repeated (multiple averages collected at each flip angle) as necessary. It should be noted, however, that the use of just two repeated flip angles might not be appropriate in some scenarios. When more than one T_1 component is present in a voxel, deviation from the SPGR signal equation cannot be identified unless a flip angle set containing more than two unique points is used. Researchers interested in detecting the presence of multiple T_1 times in individual voxels may find it useful and necessary to incorporate additional acquisition angles in addition to the two optimal angles for T_1 variance minimization.

Future extensions of this work will evaluate the performance of our proposed angle selection in situations with more distinctly non-Gaussian T_1 distributions. In this way, we hope to determine whether there are situations in which this more simplified angle selection approach using Deoni and colleagues' set of criteria is not appropriate. Furthermore, more specific definition of $P(M_0, T_1)$ based on the tissue of interest may be appropriate in some research and clinical settings. For example, specific flip angles could be selected for T_1 mapping in the white matter in the study of myelin-related disease by using only segmented white matter voxels to define $P(M_0, T_1)$.

6.7 Conclusion

In conclusion, this work demonstrates that the precision of T_1 estimates from SPGR acquisitions can be improved by using flip angles selected based on minimization of the T_1 variance weighted by the smoothed joint density of T_1 and M_0. Specifically, our proposed approach significantly out-performed T_1 estimation using a range of flip angles when the same total number of flip angles were used. Interestingly, when comparing the proposed angle selection method with previously proposed selection criteria, we found that Deoni and colleagues' 2-angle selection criteria can also be effectively used to determine the two angles to be repeated for a multi-point acquisition with nearly identically improved performance [153]. The proposed flip angle selection approach resulted in either equivalent or up to 42% reduced RMSE compared to other flip angle selection criteria in simulations. Experimentally, implementation of optimal angles reduced inter-scan variability in T_1 estimates by 30%. The application of this data-driven technique for optimal flip angle selection has applications in clinical and research settings where scans are performed repeatedly in the same anatomical region (e.g., the human brain) or on the same equipment (consistent scanner and coil). Within the work presented in this dissertation, this flip angle selection approach will be used for experimental design in future stem cell tracking and cancer imaging experiments (Chapters 6 and 7). In this way, we hope to minimize the variance of T_1 estimates and maximize the likelihood of detection of small changes in T_1 times reflective of contrast accumulation in transplanted cells of interest.

Chapter 6: PET and MRI of hNPC stably over-expressing DMT1

6.1 Preface/Abstract

In this chapter, the methods developed in Chapters 4 and 5 are combined with the approach initially investigated in Chapter 3. Here, we test whether human neural progenitor cells (hNPC) stably over-expressing divalent metal transporter 1 (DMT1) can take up sufficient Mn^{2+} and $^{52}Mn^{2+}$ for specific detectability with quantitative MEMRI and PET. To test this, two lines of hNPC stably over-expressing DMT1 ($hNPC^{DMT1}$) were established and tested *in vitro* for Mn^{2+} uptake, measured with MRI and gamma counting. We observed that although $hNPC^{DMT1}$ showed higher Mn^{2+} uptake than wild-type hNPC ($hNPC^{WT}$), the increase in uptake was much less dramatic and required higher Mn^{2+} supplementation doses than in hNPC transiently over-expressing DMT1, as tested in Chapter 3. Following *in vitro* imaging, $hNPC^{DMT1}$ and $hNPC^{WT}$ were transplanted into the right and left rat striatum, respectively, for *in vivo* MEMRI and ^{52}Mn PET. Despite transplanted cell survival and continued DMT1 over-expression in $hNPC^{DMT1}$, the Mn^{2+} and ^{52}Mn uptake in $hNPC^{DMT1}$ was insufficient for MRI or PET contrast with respect to background tissue. These results indicate that stable DMT1 over-expression may not be a suitable reporter gene approach for imaging of transplanted hNPC, although other variants of this cell imaging design hold promise.

6.2 Introduction

Long-term, *in vivo* imaging of transplanted cells is essential for the efficient translation of stem cell therapies and the interpretation of ongoing clinical trial results. An ideal technique for long-term imaging of transplanted hNPC would be safe for the subject/patient, would not perturb the cells, would be applicable over an extended period of time, would be quantitative for comparison within and amongst subjects, and would reflect the histological ground truth [53]. In previous imaging experiments with cells transiently over-expressing DMT1, we have established that this reporter has potential as a good candidate for *in vivo* imaging [34]. However, without a line of hNPC stably over-expressing DMT1 ($hNPC^{DMT1}$), this method for cell tracking is unlikely to be successful in a realistic therapeutic scenario. Stable expression of a reporter gene may allow monitoring of cell location, survival, and proliferation over the course of weeks or months, which is essential to match the time course of typical cell therapy experimentation or evaluation. Along with the methods for T_1 mapping and Mn-based MRI and PET neuroimaging developed in Chapters 4 and 5, the establishment of a line of cells stably over-expressing DMT1 is essential for evaluation of this technique. A line of $hNPC^{DMT1}$ would allow us to determine whether this technique can be used over a long period of time. Additionally, if effective for imaging, this tool would permit investigation of the effect of this imaging approach, which involved altered protein expression and manganese supplementation, on cell dynamics.

Lentiviruses (LVs) are useful for gene delivery to cells as they can infect non-dividing cells, such as our slow-growing hNPC, and introduce viral RNA directly into the cell DNA [17]. Due to the DNA insertion of viral RNA, all infected cells and their progeny would contain viral RNA, permitting sustained over-expression of the DMT1 reporter protein. Our lab has successfully used LVs for infection of several cell lines, including hNPC and mesenchymal stem cells [13-15, 19, 73]. After LV infection of multiple cell types with multiple expression vectors, we have observed significant and sustained over-expression of a variety of proteins for imaging and therapeutic delivery of trophic factors. Due to our past success using the LV expression vector design shown in **Figure 6.1**, in this work we apply this system to establish a line of $hNPC^{DMT1}$ for long-term *in vivo* imaging.

The objective of the work in this chapter is to prepare a line of cells stably over-expressing DMT1 and evaluate its efficacy for *in vivo* imaging of transplanted cells. To prepare this cell line, we aim to clone the DMT1 gene into a shuttle vector for packaging into a lentivirus. In addition, we test a cell line established using an alternate lentivirus design. After establishment of these two cell lines and verification of DMT1 over-expression, we test their ability to internalized Mn^{2+} for detectability with MRI and $^{52}Mn^{2+}$ for detectability with PET *in vitro* and *in vivo*.

6.3 Methods

6.3.1 Cloning and lentivirus preparation

In order to establish a line of cells stably over-expressing DMT1, the first step was preparation of a lentivirus (LV). This preparation required the cloning of the DMT1 sequence into a shuttle vector (SV) for packaging into a LV. We performed cloning in our lab, while a collaborating lab at Cedars-Sinai Medical Center prepared the virus. In this work, this prepared virus is referred to as LV-DMT1-CS. The cloning approach is described in the following paragraphs and illustrated in **Figure 6.1A**.

First, using PCR, the DMT1 insert was amplified from the Promega expression vector used in Chapter 3 (SLC11A2 FlexiVector, Kazusa cDNA clone library, Promega, Madison, WI, USA). The amplification was performed in order to add restriction enzyme digestion sites to the end of the gene insert for ligation with the shuttle vector. The primers used for amplification were: forward, 5'-T-AAC-**TGA-TCA**-*ATG-GTG-CTG-GGT-CCT-GAA-CA*-3'; reverse, 5'-A-TGT-**CTC-GAG**-*TTA-AAC-TTT-AAC-GTA-GCC-A*-3' (corresponds to **BclI restriction site**, **XhoI restriction site**, *DMT1 sequence*). For amplification, the DMT1 cDNA template and forward and reverse primers were combined with Promega PCR Master Mix to a final concentration of 1.6 ng primer per µL (Promega, Madison, WI, USA). The PCR amplification program used began with three minutes at 95°C for initial denaturing followed by 30 cycles of one minute at 95°C (denaturing), 30 seconds at 57°C (annealing), 2 minutes and 30 seconds at 72°C (enlongation), with a final elongation step of 10 minutes at 72°C after the final

cycle (Mastercycler, Eppendorf, Hamburg, Germany). The PCR product was run on a 2% agarose gel and extracted using a gel/PCR DNA fragment extraction kit (IBI Scientific, Peosta, IA, USA). The extracted PCR product was ligated into a T-vector for bacterial amplification using the pGEM®-T Vector system (Promega). The presence of the DMT1 insert was verified via digestion with the EcoRI restriction enzyme (Promega).

Bacterial transformation in dam and dcm negative (dam-/dcm-) competent E. coli was performed followed by isolation and verification of the presence of the DMT1 insert in the T-vector. An initial attempt transformation attempt into the dam+/dcm+ E. coli strain JM109 revealed that the BclI restriction enzyme site was sensitive to methylation, so required DNA fragments could not be cut out for subsequent subcloning into the shuttle vector. Therefore, unmethylated DNA amplified in dam-/dcm- E. coli was required. Following bacterial amplification, the T-vector plasmid with DMT1 cDNA was isolated using a QIAprep Spin Miniprep Kit (Qiagen, Hilden, Germany).

The T-vector plasmid was then digested with restriction enzymes XhoI and BclI to cut out the DMT1 insert. We carefully performed serial digestion due to the differing ideal digestion reaction conditions between XhoI and BclI. Specifically, cDNA was digested with XhoI for 1.5 hours at 37°C, the enzyme was deactivated with a 15 minute incubation at 65°C, then BclI was added followed by an overnight digest at 55°C. The shuttle vector, previously prepared and isolated in our lab, was digested simultaneously with restriction enzymes XhoI and BamHI, which has compatible overhangs with BclI (all restriction enzymes from

Promega). Following digestion, the digest products were run on a 2% agarose gel and isolated using a gel/PCR DNA fragment extraction kit (IBI Scientific).

In the final cloning step, the DMT1 insert was ligated into the shuttle vector using T4 DNA ligase (Promega). The shuttle vector subcloned DMT1 sequence, referred to herein as SV-DMT1, was amplified in JM109 E. coli, then a small amount of plasmid was isolated and sent to collaborators for lentivirus packaging (**Figure 6.1B**).

In addition to the LV prepared at Cedars-Sinai (LV-DMT1-CS), a virus prepared by a company was also tested, called LV-DMT1-Imanis (Imanis Life Sciences, Rochester, MN, USA). This LV was pursued due to the relatively poor imaging performance of the line of cells prepared from LV-DMT1-CS in comparison with cells transiently over-expressing DMT1, as described in the results section. Imanis is focused on developing viruses and cell lines for reporter gene imaging and use SV components, in particular the spleen focus-forming virus promoter (SFFV), that they have found work best for *in vivo* cell imaging (**Figure 6.1C**) [95, 196].

6.3.2 Cell line preparation

A line of hNPC previously used in cell imaging experiments, G010, was utilized in this work [19, 34, 73]. Cells were maintained in a culture of floating spheres using an identical liquid media to that used in chapter 3 of this work. Media contained DMEM and Ham's F12 (both from Sigma-Aldrich, St. Louis, MO, USA) at a ratio of 7:3 and was supplemented with 1% PSA (Life Technologies, Carlsbad, CA, USA), 1% N2 (Life Technologies), 100 ng/ml EGF (Millipore,

Billerica, MA, USA), 20 ng/ml FGF2 (WiCell, Madison, WI, USA), 10 ng/ml LIF (Millipore), and 5 ng/ml heparin (Sigma-Aldrich). Every 3-4 days, one-half of conditioned media was removed and replaced with fresh media. Cells were passaged by mechanical chopping every 10-21 days, depending on cell growth, with a McIlwain automated tissue chopper (Mickle Laboratory Engineering, Surrey, UK).

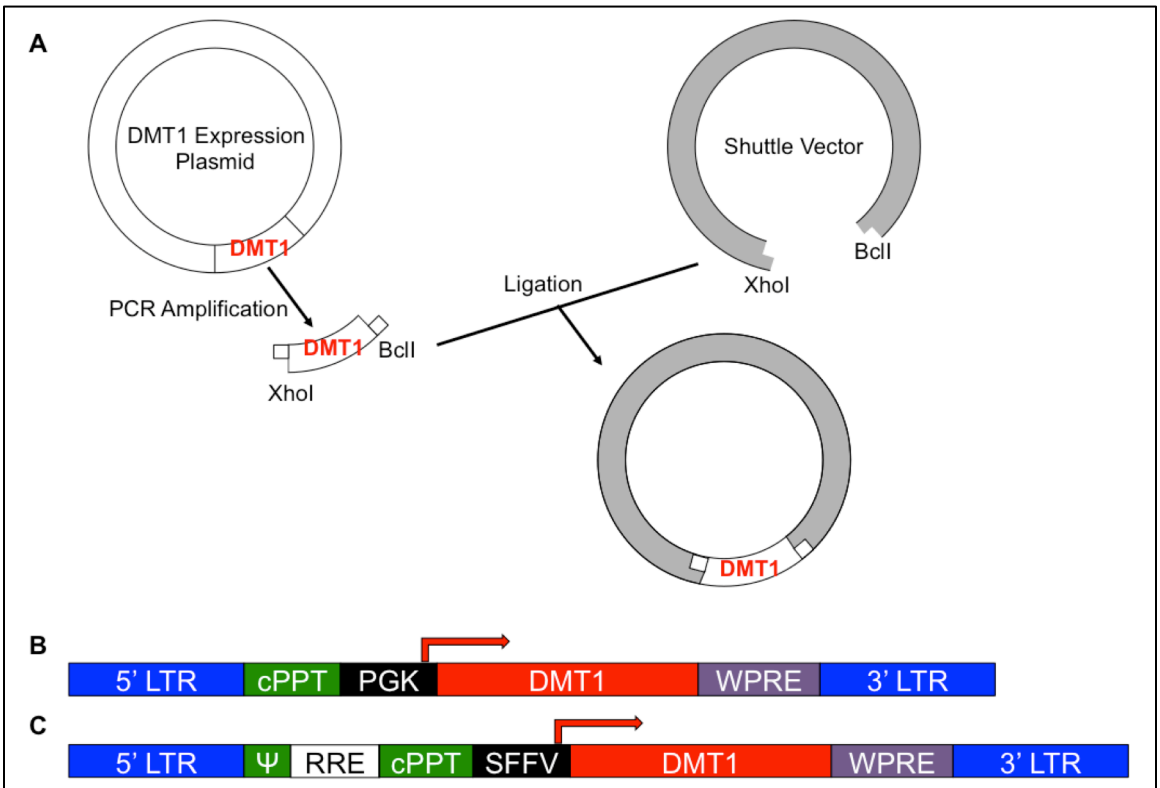

Figure 6.1: Cloning approach and shuttle vector designs for DMT1 lentiviruses. (A) To clone the DMT1 insert into the shuttle vector, PCR amplification was used to add XhoI and BclI restriction sites to the DMT1 insert. After cutting the shuttle vector with those same restriction enzymes, the DMT1 insert was ligated into the shuttle vector and packaged into (B) LV-DMT1-CS. (C) LV-DMT1-Imanis consisted of an alternate expression vector design, including the SFFV promoter. PGK: constitutive mouse phosphoglycerate kinase 1 promoter, WPRE: woodchuck posttranslational regulatory element, LTR: long terminal repeat, cPPT: central polypurine tract, Ψ: RNA packaging signal, RRE: Rev response element, SFFV: spleen focus-forming virus promoter.

For infection with LVs, cells between passage 21-38 were dissociated via treatment with TrypLE for 15 minutes (Life Technologies). After counting, the

cells were diluted to a concentration of 1000 cells/μL in filtered conditioned media mixed with LV-DMT1-CS or LV-DMT1-Imanis at a range of concentrations [17]. For LV-DMT1-CS, cells were supplemented with virus to a concentration of 20, 40, and 75 multiplicity of infection (MOI). For LV-DMT1-Imanis, cells were supplemented with virus to concentrations of 1, 3 and 10 MOI. The differences in LV concentration used were a result of recommendation from virus providers and reflect, to an extent, the efficiently of viral packaging and quality of LV production. After infection, cells were continually maintained and passaged as described above for experimentation.

At least 2-3 weeks after LV infection, $hNPC^{WT}$ and $hNPC^{DMT1}$ were plated and stained using immunocytochemistry (ICC) in order to examine protein expression and cell morphology. Following dissociation, cells were plated on glass cover slips coated with poly-ornathine and poly-L-laminin (Sigma-Aldrich) at a concentration of 1000 cells/μL. Twenty-four hours after plating, cells were fixed with 4% paraformaldehyde (PFA), washed with PBS, and then stained for DMT1. Following a thirty-minute incubation with blocking buffer (PBS, 5% normal donkey serum (NDS), 0.2% Triton X-100), a primary antibody against DMT1 (mouse monoclonal, Sigma-Aldrich) diluted 1:500 in blocking buffer was applied to the cells for one hour at room temperature. Cells were then washed with PBS. An anti-mouse secondary antibody was diluted 1:1000 in blocking buffer and applied for 30 minutes (donkey anti-mouse IgG antibody conjugated with Alexa Fluor 488; Jackson ImmunoResearch Laboratories, West Grove, PA, USA). Cell nuclei were then stained with Hoescht 33258 nuclear stain (Sigma-Aldrich) for

five minutes before mounting cover slips on slides with Fluoromount (Southern Biotech, Birmingham, AL, USA). Images were collected using a Nikon Eclipse fluorescence microscope, a Nikon Intensilight camera, and NIS Element D software (Nikon, Tokyo, Japan). For each expression time point, at least five fields of view on each of 2-3 coverslips were analyzed for percent of cells over-expressing DMT1.

6.3.3 *In vitro* imaging

Cells were imaged *in vitro* following incubation with Mn-based contrast agents to test contrast agent uptake for imaging. For MRI, $hNPC^{WT}$ and $hNPC^{DMT1}$ ($1.5\text{-}3\times10^6$ dissociated cells) were incubated with 0-200 μM $MnCl_2$ for either one or 24 hours prior to being spun down and washed with fresh media three times. After washing, cells were spun down in 0.2 mL PCR tubes, which were then stabilized in 4% agarose gel for imaging. Imaging was performed on a 4.7T preclinical MRI (Agilent Technologies, Santa Clara, CA, USA). T_1 mapping was performed using a series of 3D spoiled gradient echo acquisitions with gradient and RF spoiling, flip angles varying from three to 25°, TR = 7.29 ms, and TE = 2.91 ms [153, 175]. *In vitro* scanning field of view, resolution, dimensions varied depending on the number of samples to be scanned. Actual flip-angle imaging was also performed to estimate a flip angle map to improve accuracy of T_1 estimates [166]. T_1 was estimated using weighted linear least squares fitting [167].

For gamma counting of ^{52}Mn uptake, approximately 3×10^5 dissociated cells of each cell type were incubated with 0-1.8 uCi for one or 24 hours prior to

being spun down and washed with fresh media three times. Activity uptake was measured by automatic gamma counting on a PerkinElmer Wizard 2480 (Waltham, MA, USA) using a 60 second measurement period, with an energy window centered on the 744 keV gamma peak. Gamma counting results were corrected for decay time, machine dead time, and detection efficiency.

6.3.4 Animal studies

All animal studies were performed in accordance with protocols approved by the University of Wisconsin Institutional Animal Care and Use Committee. Adult female Sprague-Dawley rats were used for cell transplantation and *in vivo* imaging experiments. Rats were housed under controlled temperature and illumination conditions, with unrestricted access to food and water. Cyclosporine (10 mg/kg body weight, Novartis, Basel, Switzerland) was administered to rats intraperitoneally (i.p.) beginning one day prior to cell transplantation until sacrifice to minimize the likelihood of immune rejection of human cell transplants. Following imaging studies, animals were sacrificed either by CO_2 asphyxiation or by administration of 0.2 mL pentobarbital prior to transcardial perfusion. Perfusion was performed with 0.9% NaCl followed by 4% PFA, after which the brain was removed and submerged in PFA for 24 hours.

6.3.5 Cell transplantation

Cell transplantation was performed with $hNPC^{WT}$ and $hNPC^{DMT1}$ after separately collecting and resuspending each cell type at a concentration of 150,000 cells/μL in transplantation media. Media for transplantation consisted of

Leibovitz L15 medium (Life Technologies) and PBS at a 1:1 ratio, supplemented with 2% B27 (Life Technologies) and 0.6% glucose [13].

Isoflurane (2-5%) was used to anesthetize rats prior to being secured in a stereotaxic frame for transplantation procedures. Cells were injected in two sites per side in the striatum, with $hNPC^{DMT1}$ transplanted in the two sites on the right side and $hNPC^{WT}$ on the left. Cell transplantation coordinates were anterior/posterior +0.5 mm and -0.1 mm and medial/lateral ±3.3 mm and ±2.8mm with respect to the bregma, and dorsal/ventral -4.5 mm with respect to the outer surface of the neocortex. A 10 µL Hamilton syringe with a 30-gauge sharp tip needle secured to the stereotaxic frame was used for needle insertion and cell injection. After slow needle insertion, the needle was allowed to rest for two minutes prior to cell injection. At each injection site, 2-3 µL of cells (300,000-450,000 total cells) were injected at a rate of 1 µL/min, the needle was left in place for two additional minutes, then the needle was slowly removed [19]. Due to slow cell growth and therefore low cell numbers, two rats were transplanted with $hNPC^{DMT1\text{-}1}$ and imaged with MEMRI, and six rats were transplanted with $hNPC^{DMT1\text{-}2}$ and imaged with MEMRI (*N*=3) and ^{52}Mn PET (*N*=3).

6.3.6 *In vivo* MRI and PET

Manganese contrast agent delivery and Mn^{2+}-based MRI and PET imaging protocols developed in Chapters 4 and 5 of this work were used for *in vivo* imaging of transplanted stem cells. For MRI contrast agent delivery, animals were anesthetized with 1% isoflurane in oxygen and placed on a warm water pad to maintain body temperature. $MnCl_2$ solution (66.7 mM in bicine buffer, 60 mg/kg

body weight) was delivered intravenously using a slow infusion pump at a rate of 2 mL/hr. Following an infusion line flush with heparinized saline, animals were delivered saline subcutaneously to minimize dehydration. Both prior to and 48 hours following contrast administration, animals underwent *in vivo* MRI on a 4.7T preclinical scanner. T_1 mapping was performed with 3D variable flip angle SPGR acquisitions, as described in the *in vitro* imaging section. Flip angles used were 2° and 12° with 8 averages each, selected using the flip angle selection approach developed in Chapter 5. For comparison, acquisitions at 2°, 7°, 12°, and 18° with 4 averages each were also acquired. T_1 maps were calculated using weighted linear least squares fitting [167].

PET imaging was performed 4 and 48 hours following administration of no-carrier-added $^{52}Mn^{2+}$. Contrast was delivered via tail vein infusion of 2 mCi/kg formulated in saline at 1.5 mCi/mL. PET acquisitions consisted of a 30-minute timing window with a single static frame. Because we were focused on imaging cells transplanted into the brain, full-body scans were not acquired. Reconstruction was performed with a vendor-provided 2D ordered subset expectation maximization algorithm, using attenuation correction but no scatter correction due to the relatively low signal expected in the brain.

6.3.7 Immunohistochemistry

Perfusion and histological analysis could only be performed in rats that were not delivered $^{52}Mn^{2+}$ due to the long radioactive half-life of the tracer. Rat brain samples were stored for one day in PFA following perfusion after MRI studies, and were then moved to 30% sucrose solution in preparation for

sectioning. A frozen stage microtome was used to prepare 35 μm brain sections for immunohistochemistry. A primary antibody against human glial fibrillary acidic protein (hGFAP, catalog number 123, StemCells Inc, Newark, CA, USA) was used to detect the presence and survival of transplanted human cells. A primary against human DMT1 (hDMT1, catalog number 4891M1, Sigma-Aldrich) was used to determine whether hNPC^{DMT1} continued to over-express the protein following transplantation. Sections were washed in PBS (3×5 minutes) then blocked in buffer (PBS, 3% NDS, 0.25% Triton X-100) for 1 hour at room temperature. Next, the primary antibody diluted 1:200 in blocking buffer was applied to sections and incubated overnight at RT. PBS washes (3×5 minutes) were performed before secondary antibody incubation (donkey anti-mouse Alexa Fluor 488 antibody 1:500 in blocking buffer) for 1 hour. Sections were mounted on glass slides with DAPI mounting medium and examined with a Nikon fluorescence microscope.

6.4 Results

6.4.1 DMT1 expression

Approximately four weeks following infection of hNPC with both LV-DMT1-CS and LV-DMT1-Imanis, cells were plated and ICC was performed to observe and evaluate resulting DMT1 expression. In both cases, we observed larger percentages of cells over-expressing DMT1 with increasing LV concentration (**Figure 6.2A**). To quantify protein expression, the number of cells over-expressing DMT1 was counted and compared to the total number of cells in 5-6 fields of view on 3 cover slips per level of infection. In contrast, infection of hNPC

with varying viral titers (10-75 multiplicity of infection, MOI) of LV-DMT1-CS resulted in DMT1 over-expression in up to 72.1% of cells. Infection with much lower levels of LV-DMT1-Imanis (1-10 MOI) resulted in up to 90.0% over-expression (**Figure 6.2B**). Additionally, the stable expression of DMT1 was verified by plating and staining cells 4 and 12 weeks following infection. LV-DMT1-CS infected hNPC showed a slight increase in DMT1 over-expression from 4 to 12 weeks following infection, and in no cases did we observe a decrease in expression over time.

To gain a preliminary understanding of the effect of DMT1 over-expression on cell growth, the approximate time of cell sphere doubling was observed by daily gross observation of sphere cultures under a microscope. The cell cultures in which greater than 50% of cells over-expressed DMT1 had slower growth and increased doubling time (from approximately 10-14 days for normal cell cultures compared to 21-28 days for slow-growth cultures). The effect on cell growth was observed in cells infected with either LV-DMT1-CS or LV-DMT1-Imanis. To balance protein expression with cell viability and growth, two populations of cells were maintained for imaging experiments for each virus. In the case of LV-DMT1-CS, cells infected with 40 MOI (47% over-expression) and 75 MOI (72% over-expression) were used for *in vitro* and *in vivo* imaging experiments, respectively. In the case of LV-DMT1-Imanis, cells infected with 1 MOI (50% over-expression) and 3 MOI (79% over-expression) were used for *in vitro* and *in vivo* imaging experiments, respectively. Due to slow growth and challenges of maintaining the cell lines in which 70-80% of cells were over-expressing DMT1,

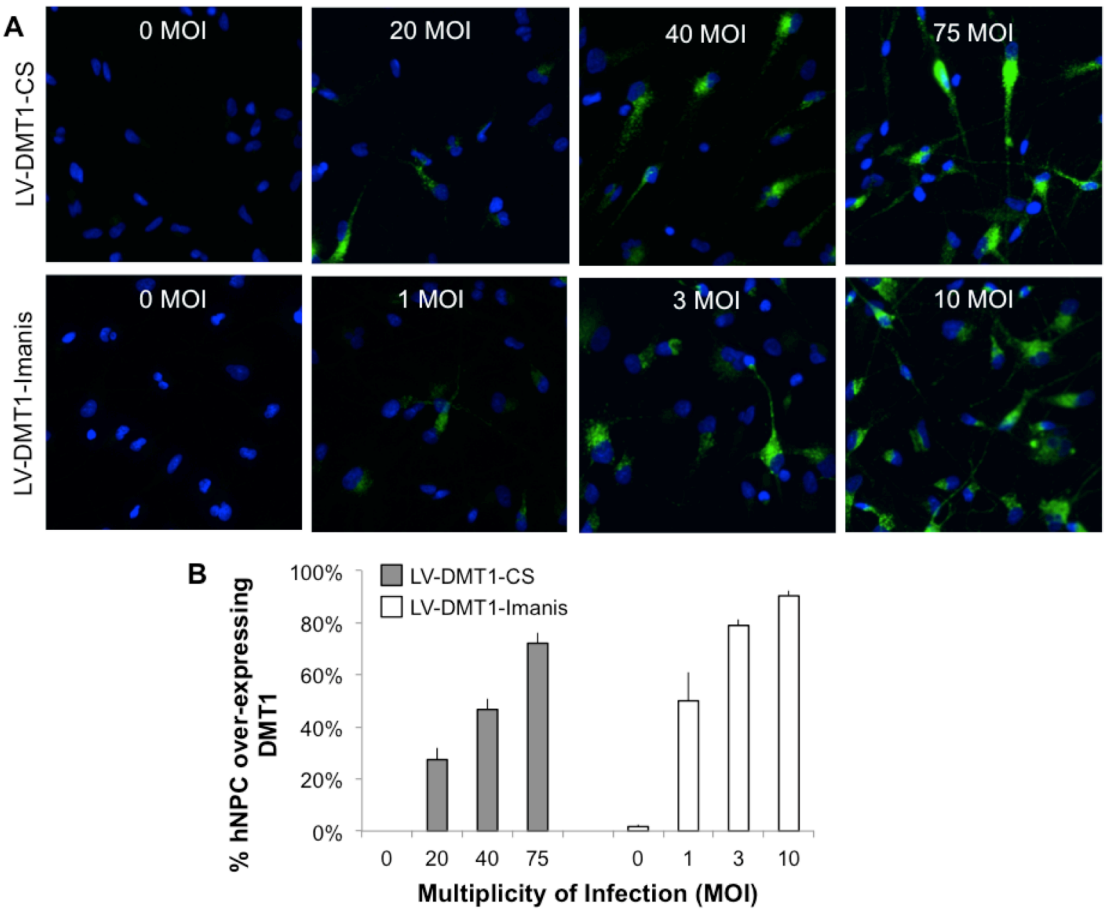

Figure 6.2: Stable *in vitro* expression of DMT1 following infection with LV-DMT1-CS and LV-DMT1-Imanis. (A) At least four weeks following infection, cells were plated and stained for human DMT1 protein. Higher LV concentration resulted in increased DMT1 over-expression. (B) When plated, stained cells were counted for protein expression, and we observed up to 90% over-expression. LV-DMT1-Imanis produced higher over-expression levels at lower MOIs used.

their use was primarily reserved for *in vivo* imaging, where it was presumed increased Mn uptake in hNPC^{DMT1} may be more challenging to detect.

6.4.2 *In vitro* imaging

Upon establishment of DMT1 over-expression in LV-infected hNPC lines (termed hNPC^{DMT1}), we aimed to determine whether this over-expression would increase uptake of Mn^{2+} and ^{52}Mn *in vitro* for imaging. As experiments were performed first on hNPC^{DMT1} established using LV-DMT1-CS, followed by those

established using LV-DMT1-Imanis, the results will be presented in that order ($hNPC^{DMT1-1}$ and $hNPC^{DMT1-2}$, respectively).

For *in vitro* MRI following Mn supplementation, $hNPC^{DMT1-1}$ and $hNPC^{WT}$ were incubated for one hour with 0-200 μM $MnCl_2$ (**Figure 6.3A**). When no differences were observed between the two cell lines, the experimented was repeated with increased incubation time of 24 hours (**Figure 6.3B**). In this second trial, cells were also allowed to rest one day following dissociation prior to $MnCl_2$ supplementation, as was the case for transiently-expressing cells (Chapter 3). Under these conditions, an increase in R_1 relaxation time of $hNPC^{DMT1-1}$ compared to $hNPC^{WT}$ was observed, although this difference was less striking than that observed in Chapter 3 in cells transiently over-expressing DMT1, even when supplemented with lower concentrations of $MnCl_2$. Additionally, *in vitro* gamma counting of ^{52}Mn uptake was performed by incubating $hNPC^{DMT1-1}$ with varying levels of activity, and a linear relationship between activity supplemented and activity retained was observed (**Figure 6.3C**). Unfortunately, due to an accidental and unexpected loss of cells, these numbers could not be directly compared to uptake of ^{52}Mn in $hNPC^{WT}$.

After preparation of another DMT1-expressing cell line, $hNPC^{DMT1-2}$, *in vitro* MRI and gamma counting were repeated. For MRI, $hNPC^{DMT1-2}$ and $hNPC^{WT}$ were incubated with 0-200 μM $MnCl_2$ for either one or 24 hours prior to *in vitro* imaging. A slight difference in uptake was observed between the cell lines incubated 24 hours (**Figure 6.4A**). *In vitro* uptake of ^{52}Mn in $hNPC^{DMT1-2}$ was higher than that in $hNPC^{WT}$ after both one and 24-hour incubations (**Figure**

6.4B). The percent increase was consistent between the two incubation times, with hNPC^{DMT1-2} taking up approximately 60% more $^{52}Mn^{2+}$ than hNPC^{WT}. For both cell types, the 24-hour incubation resulted in approximately 3.5 times higher uptake than the one-hour incubation.

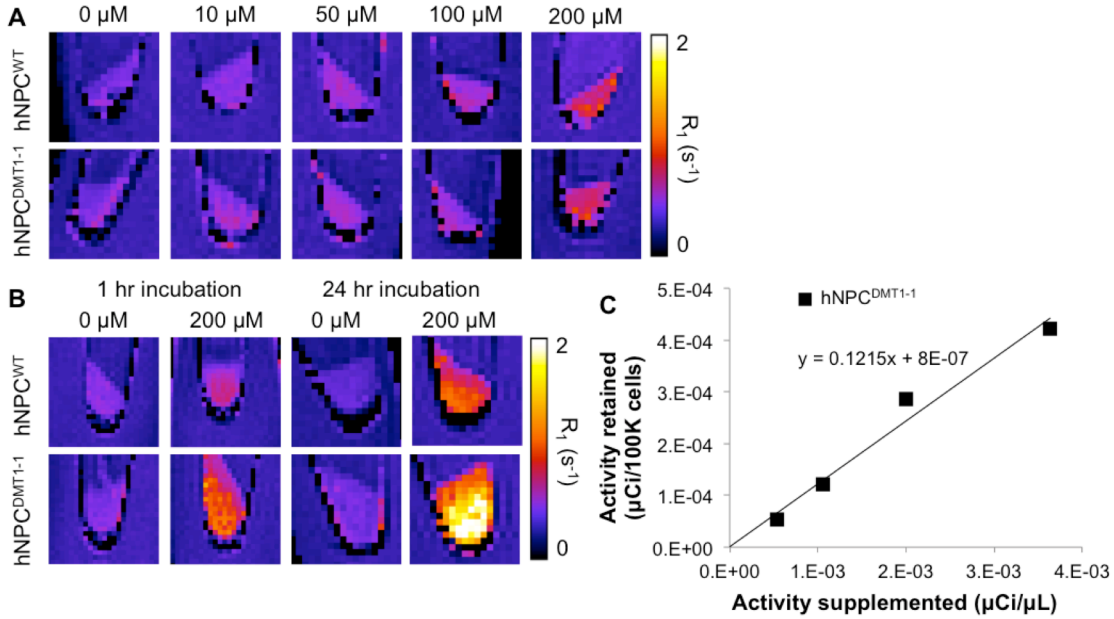

Figure 6.3: *In vitro* imaging and ^{52}Mn uptake measurement in hNPC^{DMT1-1} and hNPC^{WT}. (A) No differences in Mn^{2+} uptake were observed between hNPC^{DMT1-1} and hNPC^{WT} with *in vitro* MRI after 1 hour incubation with 0-200 μM $MnCl_2$. (B) Increased Mn uptake was observed in hNPC^{DMT1-1} in a second *in vitro* imaging experiment, particularly after 24 hour incubation with $MnCl_2$. However, the R_1 increase observed in hNPC^{DMT1-1} compared to hNPC^{WT} was less than that observed in transiently over-expressing cells in Chapter 3. (C) A linear relationship between ^{52}Mn activity supplemented and activity retained indicates ^{52}Mn uptake in hNPC^{DMT1-1}.

6.4.3 *In vivo* imaging and histology

In spite of the less striking uptake of Mn^{2+} in hNPC^{DMT1-1} compared to transiently over-expressing cells, we next tested whether hNPC^{DMT1-1} could be detected *in vivo* with MEMRI. In these experiments, we used the Mn delivery and imaging protocols developed in Chapters 4 and 5 of this work. Six days following transplantation of hNPC^{WT} into the left striatum and hNPC^{DMT1-1} into the right

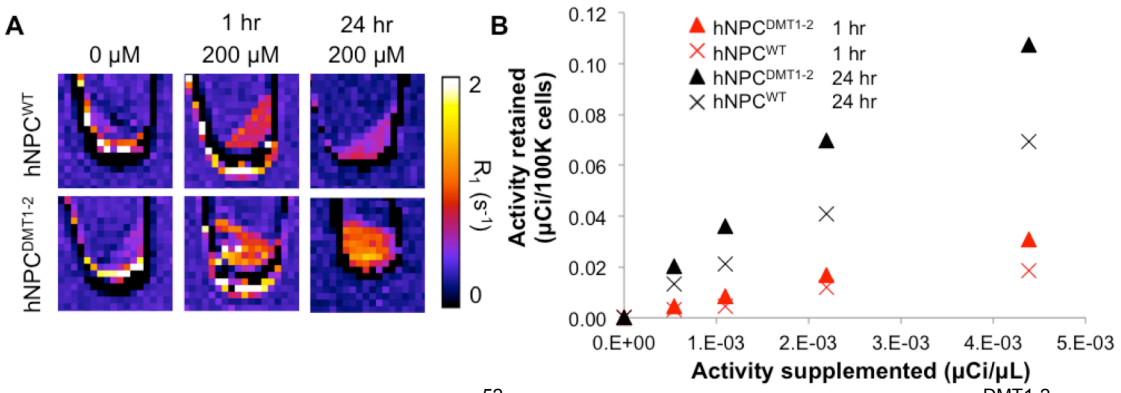

Figure 6.4: *In vitro* imaging and ^{52}Mn uptake measurement in $hNPC^{DMT1-2}$ and $hNPC^{WT}$. (A) Moderately increased uptake of Mn^{2+} in $hNPC^{DMT1-2}$ compared to $hNPC^{WT}$ is observable with MEMRI, particularly after a 24-hour incubation of cells with $MnCl_2$. (B) In both cell types, uptake of ^{52}Mn increased linearly with supplemented activity. For both one hour and 24 hour incubation times, uptake in $hNPC^{DMT1-2}$ was approximately 60% higher than uptake in $hNPC^{WT}$. A longer incubation of 24 hours compared to one hour increased total ^{52}Mn uptake by a factor of approximately 3.5 in both cell types.

striatum of two rats, both subjects underwent MR imaging using quantitative T_1 mapping. One day following pre-contrast imaging, $MnCl_2$ was delivered systemically via tail vein infusion, and then imaging was repeated 48 hours following contrast administration. Although general brain enhancement was observed in both subjects, no specific uptake in the vicinity of transplanted $hNPC^{DMT1-1}$ was observed in either subject (**Figure 6.5A and B**). To verify that this was not due to transplanted cell death or a reduction in DMT1 over-expression, histology was performed. Sections were stained for human GFAP to investigate survival of both $hNPC^{WT}$ and $hNPC^{DMT1-1}$ and for human DMT1 protein to verify that $hNPC^{DMT1-1}$ protein over-expression was maintained following transplantation (**Figure 6.5C and D**). Positive hGFAP staining in both striata indicated survival of both cell types following transplantation, while positive hDMT1 staining on the right side indicated that DMT1 over-expression was

maintained. Due to the lack of success of *in vivo* MEMRI detection of hNPC^{DMT1-1} and the challenges we anticipated facing with low ^{52}Mn brain uptake (Chapter 5), neither *in vivo* imaging of hNPC^{DMT1-1} with ^{52}Mn PET nor long-term *in vivo* imaging with MEMRI were not pursued at this time.

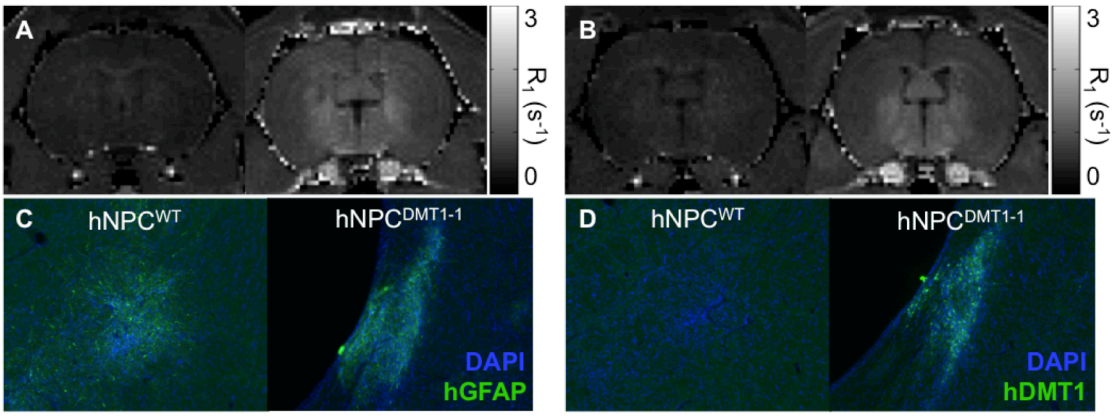

Figure 6.5: *In vivo* MEMRI and histology of transplanted hNPC^{WT} and hNPC^{DMT1-1}. (A and B) Pre-contrast (left) and 48 hour post-contrast (right) images of the rat brain after transplantation of hNPC^{WT} in the left striatum and hNPC^{DMT1-1} in the right striatum. Specific enhancement in the vicinity of hNPC^{DMT1-1} due to increased Mn^{2+} was not observed in either subject. (C) Positive staining for hGFAP on both sides indicated that both cell types survived transplantation and imaging. (D) Positive staining for hDMT1 on the right side indicated that hNPC^{DMT1-1} continued to over-express DMT1 following transplantation, but nevertheless did not show sufficient Mn uptake for detectability with *in vivo* MEMRI.

A second line of cells over-expressing DMT1, hNPC^{DMT1-2}, was also imaged *in vivo* after transplantation in the rat striatum. Cells were transplanted into the left (hNPC^{WT}) and right (hNPC^{DMT1-2}) striatum of six rats, and then *in vivo* PET and MRI were performed (*N*=3 per modality). For subjects undergoing MRI, T_1 mapping in the brain was performed prior to and at 48 hours following delivery of $MnCl_2$. Specific enhancement was observed in the vicinity of neither hNPC^{DMT1-2} nor hNPC^{WT} despite generalized uptake of Mn^{2+} in the brain (**Figure 6.6A**). Histological analysis on brain tissues following *in vivo* MR imaging

revealed that cells survived the transplantation and imaging procedure and that hNPC^{DMT1-2} continued to over-express DMT1 (**Figure 6.6C**).

Three subjects underwent PET/CT following cell transplantation. At 4 and 48 hours after intravenous delivery of ^{52}Mn, PET/CT of the upper body and head were acquired. Reconstructed images showed low uptake in the brain, with no observable increase in activity in the vicinity of transplanted hNPC (**Figure 6.6B**). Activity uptake was also observed in resected brain tissue with autoradiography, but there was not an increase in activity in the vicinity of hNPC^{DMT1-2} (data not shown).

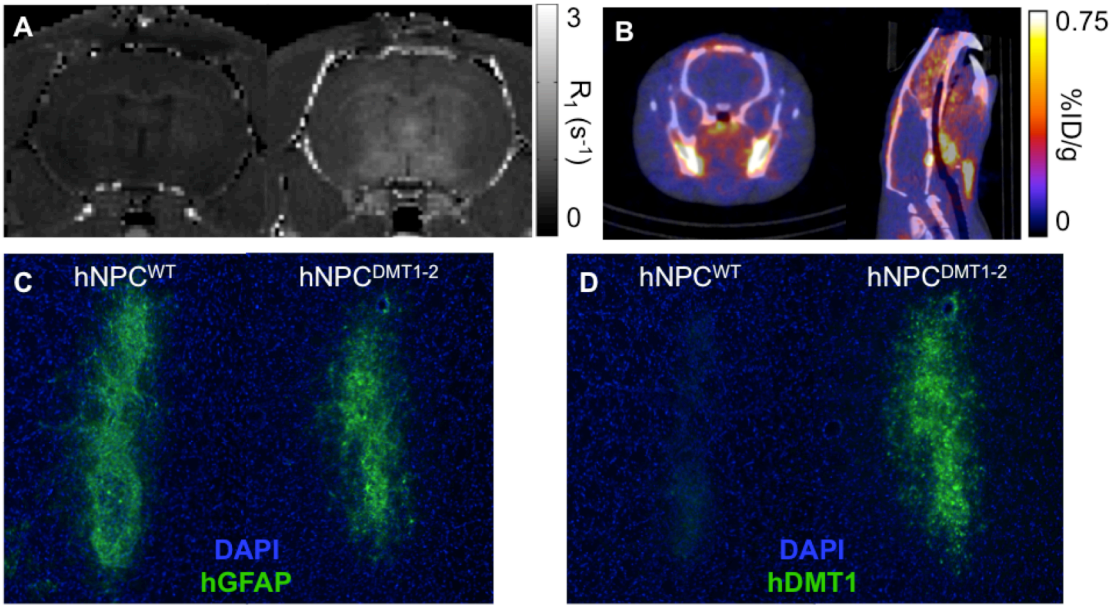

Figure 6.6: MEMRI, PET/CT, and histology of transplanted hNPC^{WT} and hNPC^{DMT1-2}. Despite transplanted cell survival and high DMT1 over-expression in hNPC^{DMT1-2} (C, D), transplanted cells were not detected with (A) MEMRI or (B) PET/CT. Expected Mn^{2+} and ^{52}Mn brain uptake levels were achieved, but Mn^{2+} uptake was not sufficiently high in hNPC^{DMT1-2} for contrast with respect to background tissue.

6.5 Discussion

In this chapter, we have established two lines of cells stably over-expressing the DMT1 protein to test for *in vivo* stem cell tracking in the rat brain. After initial lack of success imaging $hNPC^{DMT1\text{-}1}$, we pursued the establishment of an additional cell line, $hNPC^{DMT1\text{-}2}$, with a modified expression vector construct as an alternative approach.

Although we initially encountered challenges in cloning the DMT1 construct into an appropriate shuttle vector, successful SV-DMT1 preparation was achieved and the construct was packaged into a lentivirus for infection of hNPC and establishment of $hNPC^{DMT1\text{-}1}$. We observed high levels of DMT1 over-expression in infected hNPC, with up to 70% of cells over-expressing the reporter protein. However, the notably slower growth of cell lines over-expressing DMT1 at a rate of greater than approximately 50% indicated that, if successful for imaging, the balance between expression levels for imaging and cell viability would have to be optimized. Several serial analyses of protein over-expression in $hNPC^{DMT1\text{-}1}$ indicated that protein over-expression was indeed stable over the course of three months. In $hNPC^{DMT1\text{-}2}$, we observed similar DMT1 over-expression as in $hNPC^{DMT1\text{-}1}$, although a much lower viral titer was required to reach similar expression levels. Again, although very high over-expression could be achieved, levels of near 50% seemed preferable as a balance between cell growth rate and high DMT1 over-expression for imaging.

We initially tested *in vitro* uptake of Mn^{2+} in $hNPC^{DMT1\text{-}1}$ with MRI, using an identical supplementation and imaging protocol as used for cells in Chapter 3

(**Figure 3.4**). The lack of observable R_1 differences of the two cell types prompted protocol modification with a longer period of time between cell dissociation and $MnCl_2$ supplementation, higher concentrations of $MnCl_2$ applied, and longer incubation. With these modifications, we observed differences in Mn^{2+} uptake between $hNPC^{WT}$ and $hNPC^{DMT1-1}$. However, the high $MnCl_2$ concentration required for this observable difference may not be safely achievable *in vivo*, where we expect to observe concentrations of less than 100 μM after intravenous delivery of 60 mg $MnCl_2$ per kg body weight [155]. On the other hand, the longer incubation time may be more biologically relevant compared to a one hour incubation, as we observed high Mn^{2+} brain uptake in rats sustained for 1-4 days following systemic delivery (Chapter 4). *In vitro* imaging of $hNPC^{DMT1-2}$ yielded similar results, with observable, but not striking, differences in Mn^{2+} and $^{52}Mn^{2+}$ uptake compared to $hNPC^{WT}$. Following observation of these *in vitro* imaging results, it was necessary to test whether this moderately enhanced Mn^{2+} uptake in $hNPC^{DMT1}$ could still facilitate transplanted cell detectability with *in vivo* Mn-based MRI and PET.

Due to low cell numbers and slow growth, *in vivo* imaging of transplanted $hNPC^{DMT1}$ could be tested in a limited number of subjects. In an initial trial of imaging cells in two rats with MEMRI, $hNPC^{DMT1-1}$ did not show sufficiently increased Mn^{2+} uptake to provide contrast compared to background uptake levels. Additionally, no discernable R_1 difference was observed between $hNPC^{DMT1-1}$ and $hNPC^{WT}$. Positive histological staining in these subjects against hGFAP and hDMT1 indicated that the cells indeed survived the transplantation

and imaging process, so cell death or reduction in DMT1 over-expression did not appear to be the cause of lack of cell detection. Furthermore, no T_2* signal dropout was observed near the cell transplants as in Chapter 4, so that did not explain the lack of R_1 enhancement. Similarly, increased uptake of neither Mn^{2+} nor $^{52}Mn^{2+}$ was observed in $hNPC^{DMT1-2}$. On T_1 maps and PET/CT images, transplanted cells could not be distinguished from background tissue, as hypothesized, despite cell survival and continued DMT1 over-expression.

The challenges encountered in imaging $hNPC^{DMT1}$ in this chapter could be due to a variety of factors. First, a notable difference in the character of DMT1 over-expression was observed between transiently over-expressing cells (hNPC-DMT1, which were successfully detected *in vivo* in Chapter 3 of this work) and stably over-expressing cells ($hNPC^{DMT1}$). Although DMT1 over-expression was limited to a maximum of approximately 40% of cells one day following transfection, transiently expressing cells showed extremely high DMT1 expression in DMT1+ cells. On the other hand, in $hNPC^{DMT1}$, though expression was more widespread, the level of expression was more moderate in DMT1+ cells. This could reduce overall Mn^{2+} uptake in DMT1+ cells, resulting in reduced contrast between $hNPC^{WT}$ and $hNPC^{DMT1}$.

In addition to reduced levels of DMT1 expression in DMT1+ cells, it is also possible that the DMT1 protein in $hNPC^{DMT1}$ had different biological activity and function compared to hNPC-DMT1. At endogenous expression levels, DMT1 activity has been shown to be dependent on intracellular iron concentrations, extracellular pH, transferrin protein, membrane potential, and extracellular

calcium [29, 101, 105]. Although it is out of the scope of this study to interrogate the impact of these variables on Mn^{2+} internalization by DMT1, we hypothesize that such mediators of DMT1 activity may be more faithfully conserved in $hNPC^{DMT1}$ than in hNPC-DMT1, possibly reducing the amount of Mn^{2+} that can be transported into the cell.

The motivation in pursuing the cell tracking approach tested in this chapter was to retain the favorable imaging features of hNPC-DMT1 while making possible long-term monitoring of the location and survival transplanted cells and their progeny. However, due to reduced uptake of Mn-based contrast agents in $hNPC^{DMT1}$ compared to hNPC-DMT1, contrast accumulation was insufficient for contrast between transplanted cells and background tissue. Therefore, in this chapter we were unable to reach our objective of long-term *in vivo* imaging of hNPC over-expressing DMT1. Despite the lack of success of this specific approach, some variations of this cell tracking method still hold potential. Pre-labeling cells transiently over-expressing DMT1 with Mn^{2+} or $^{52}Mn^{2+}$ could allow cell tracking over the course of several weeks, for initial evaluation of cell location and migration post-transplantation. In addition, the level of DMT1 over-expression, effect of expression on cells, and DMT1 protein function may prove to be dependent upon cell type. Therefore, other cell types stably over-expressing DMT1, such as mesenchymal stem cells or skeletal muscle progenitor cells, may hold potential for *in vivo* imaging in peripheral tissues or the brain.

6.6 Conclusion

In conclusion, in this chapter we have established two lines of hNPC stably over-expressing DMT1 and tested them for Mn^{2+} contrast agent uptake and *in vivo* imaging potential. Increased uptake of Mn^{2+} and $^{52}Mn^{2+}$ was observed in $hNPC^{DMT1}$, but this increase was insufficient for MR and PET image contrast with respect to background tissue following cell transplantation. For this reason, this specific approach was not further pursued for long-term imaging and not further investigated for functional effects of this imaging technique on hNPC. However, in future investigations, variations on the approach developed and investigated in this dissertation may hold for transplanted stem cell imaging.

Chapter 7: Characterization of a broad-spectrum cancer targeting MRI contrast agent

7.1 Preface/Abstract

In this chapter, we apply the quantitative imaging methods and knowledge developed in our work imaging stem cells with MRI and PET to characterization of a novel MRI contrast agent. T_1 mapping and contrast-enhanced imaging is used to characterize Gd-DO3A-404, an alkylphosphocholine (APC) analog labeled with DOTA-conjugated Gd^{3+}. Analysis of the relaxivity of Gd-DO3A-404 using T_1 mapping revealed that it has favorable r_1 relaxivity at 4.7T, as high as 5.84 s^{-1}/mM. *In vivo* T_1-weighted imaging and T_1-mapping was used to detect specific and sustained tumor uptake in human cancer cell lines of non-small cell lung cancer and glioma. In comparison to the uptake of the non-targeted DOTA-conjugated Gd^{3+} agent Dotarem®, Gd-DO3A-404 was found to have significantly higher tumor to muscle uptake ratios. Additionally, uptake was maintained for a longer period of time following Gd-DO3A-404 administration (4-7 days compared to 60 minutes). Initial testing of Gd-DO3A-404 in an orthotopic human glioblastoma stem cell line showed striking uptake in a minority of brain tumors. In all, these results indicate that with favorable relaxation characteristics and sustained signal-enhancing uptake in multiple tumor models, Gd-DO3A-404 has great potential as a tumor-targeting MR contrast agent. As part of a library of APC analogs labeled with PET/optical tracers and therapeutic radionuclides, Gd-DO3A-404 further expands theranostic capabilities for a variety of applications.

7.2 Introduction

Phospholipids and their analogs have been investigated in recent years as tumor-targeting agents for molecular imaging, optical surgical navigation, and targeted radionuclide therapy [5, 143, 144, 146, 148-150, 197]. A primary strength of phospholipid analogs is their broad tumor-targeting capabilities and, if well designed, their high tumor specificity compared to normal healthy tissues, particularly in the liver and kidney [5, 148]. These characteristics facilitate safe and highly specific imaging of primary tumors and detection of metastases. This capability was clearly illustrated in one of the first in-human trials of the radioiodine-labeled alkylphosphocholine (APC) analog ^{124}I-CLR1404, in which three previously unknown ^{18}F-FDG-negative brain lesions were detected [5]. Investigations of additional applications of APC analogs, such as fluorescence imaging, ^{131}I particle therapy, and optical surgical navigation, have displayed their broad functional applicability and established a strong multi-modality foundation [5, 149, 150, 198].

Although targeted cancer imaging with APC analogs has been successful with PET and optical agents, this suite of imaging agents is subject to a historical mismatch between the spatial resolution of an imaging modality and the biologic resolution of an imaging agent. An agent for high-resolution imaging with radiography, CT, or MRI would provide potential for higher-resolution imaging better matched to the sub-cellular biological resolution of APC analogs. In addition, a targeted agent could more accurately represent the underlying biological characteristics of the tumor of interest than traditional contrast agents

for these modalities, for which uptake depends more on vascularity and physical tissue characteristics.

In this work, an APC analog labeled with the T_1-shortening MRI contrast agent Gd^{3+} is characterized. The design of this agent, Gd-DO3A-404, was motivated by a wide variety of potential applications. The higher resolution of MRI compared to PET and optical imaging would allow more precise tumor delineation for surgical planning. In comparison to traditional, biologically inert Gd^{3+}-labeled MR contrast agents, Gd-DO3A-404 may be used to more accurately observe tumor progression by eliminating the complications in contrast-enhancement caused by inflammation, radiation necrosis, and pseudo-progression [199]. APC analogs labeled with PET and MRI contrast agents may be used in concert to take advantage of the complementary strengths of PET and MRI and the recently increased availability of PET/MRI technology [41]. Finally, due to the high neutron capture cross-section of gadolinium, Gd-DO3A-404 may have applications in targeted neutron capture therapy of cancer [200].

Prior to investigation of this variety of applications, thorough characterization of Gd-DO3A-404 is required. The objective of the work described in this chapter is to investigate the MR relaxation characteristics, biodistribution, and tumor uptake of Gd-DO3A-404. We aim to determine whether, like other APC analogs labeled with imaging agents, Gd-DO3A-404 targets multiple cancer cell types, in particular including human cancer cell lines and *in situ* (orthotopic) models.

7.3 Methods

7.3.1 Relaxivity measurement

Gd-DO3A-404 was formulated in saline, excipient, and human plasma for *in vitro* imaging and relaxivity measurement. Serial dilutions of 0, 0.125, 0.25, 0.5, and 1 mM agent (molecular weight 1067 g/mol) were imaged in syringes with a 4.7T preclinical MRI scanner (Agilent Technologies, Santa Clara, CA). Sample temperature was monitored and maintained between 20-21°C. T_1 estimation was performed using a series of inversion recovery (IR) spin echo (SE) scans with the following scan parameters: TR = 6000 ms, TE = 13.21 ms, slice thickness = 1 mm, TI (in ms) = 8, 20, 45, 82, 130, 215, 350, 570, 928, 1500, 2500, 4000. T_1 values were then estimated using Matlab to fit the acquired data to the model for T_1 inversion recovery, $S = \left|M_0 - 2M_o e^{TI/T_1}\right|$, via nonlinear least squares fitting (Matlab R2014b, MathWorks, Natick, MA). T_2 estimation was performed using a multi-echo SE scan with the following scan parameters: TR = 2000 ms, TE (in ms) = 10, 20, 30, 40, 50, 60, 70, 80, 90, 100, 110, 120, 130, 140, 150, 160, number of excitations (NEX) = 3, slice thickness = 1 mm. T_2 values were then estimated using Matlab to fit the acquired data to the model for T_2 decay, $S = M_0 e^{-TE/T_2} + r$.

7.3.2 Animal studies

All animal studies were performed in compliance with protocols approved by the University of Wisconsin-Madison Institutional Animal Care and Use Committee. Mice had unrestricted access to food and water. Two flank xenograft tumor models were developed by injection of tumor cells in the right flank of

female nude athymic mice. Injections of 1×10^6 tumor cells in 50-100 μL PBS were performed 3-4 weeks (U87, glioma) or 4-6 weeks (A549, non-small cell lung cancer) prior to imaging [5]. An orthotopic glioblastoma model was established by stereotactic injection of 2×10^6 glioblastoma stem cells (line 12.1) in the right striatum of immunodeficient NOD/SCID mice [201].

The two contrast agents tested in this study, Gd-DO3A-404 or Dotarem®, were both delivered at a total dose of 2.34 μmol per subject. Gd-DO3A-404 (2.5 mg) was formulated in 250 μL excipient and delivered in a bolus tail vein injection to alert mice prior to imaging. For three of the six mice with orthotopic glioma xenografts, the dose was increased to 3.7 mg Gd-DO3A-404. Dotarem® was formulated in 112 μL saline. Due to its more rapid uptake and washout dynamics, Dotarem® was delivered via tail vein bolus to anesthetized animals within the magnet. This delivery permitted imaging of Dotarem® uptake immediately following delivery. For imaging procedures, anesthesia was induced with 2% isoflurane in oxygen and maintained with 1-1.5% isoflurane in oxygen. Respiration was monitored throughout the procedure, and body temperature was maintained using an external temperature probe and warm air blower.

7.3.3 *In vivo* imaging

Prior to contrast delivery and at various time points following administration, T_1-weighted images and T_1 maps were acquired of xenografts for comparison of signal intensity. In addition, for mice bearing flank xenografts, T_1-weighted images were acquired of the abdomen for comparison of signal in the liver, kidneys, and blood (in the heart). For mice bearing flank xenografts, the

imaging paradigm was as follows: T_1-weighted tumor images were collected at seven imaging time points (pre-contrast, 1 hr, 24 hr, 48 hr, 72 hr, 4 day, 7 day); T_1 mapping was performed at pre-contrast and 48 hr time points; T_1-weighted abdomen images were collected at five imaging time points (pre-contrast, 1 hr, 24 hr, 4 day, 7 day). For mice bearing orthotopic xenografts, imaging was performed pre-contrast and at 24, 48, and 72 hours post-contrast (N=3, delivered 2.5 mg Gd-DO3A-404) or at a single time point 48 hours post-contrast (N=3, delivered 3.7 mg Gd-DO3A-404).

All *in vivo* scans were acquired on the same 4.7T preclinical MRI scanner. Some variations in scan parameters between flank and orthotopic xenografts are due to a scanner upgrade between the two sets of experiments. T_1-weighted fast spin echo scan parameters were as follows for flank/orthotopic xenografts: TR = 206/176 ms, echo spacing = 8.94/7.31 ms, echo train length = 2/2, effective TE = 8.94/7.31 ms, NEX = 10/20, matrix size = 192×192/128×128, field of view (FOV) = 40×40/27×27 mm^2, number of slices = 10/10, slice thickness = 1/0.75 mm. T_1-weighted abdomen imaging was performed using a fast spoiled gradient echo (SPGR) scan with the following parameters: TR = 8.66 ms, TE = 3.6 ms, TE2 = 6.03 ms, NEX = 4, flip angle (FA) = 40°, matrix = 128×128×96, volumetric FOV = 30×30×22.5 mm^3. T_1 mapping was performed using variable flip angle SPGR scans, with actual flip imaging (AFI) for flip angle mapping [153, 166]. Scan parameters were as follows for T_1 mapping of flank/orthotopic xenografts: TR = 4.62/4.77 ms, TE = 1.58/1.65 ms, TE2 = 2.02/2.02 ms, NEX = 3/6, FA = 2°, 3°, 10°, 13° (both tumor types), matrix = 32×128×128/32×96×96, volumetric FOV =

10×40×40/10×25×25 mm^3. T_1 estimation was performed via weighted linear least squares fitting with flip angle correction [167].

7.4 Results

7.4.1 Relaxivity measurement

The relaxation properties of Gd-DO3A-404 were investigated on a 4.7T preclinical MR scanner. Serial dilutions of the agent prepared in saline, excipient, and human plasma were scanned. An inversion recovery sequence was used for T_1 quantification, while a spin echo scan with multiple echo times was used for T_2 quantification. Representative R_1 and R_2 maps ($R_1=1/T_1$, $R_2=1/T_2$) of Gd-DO3A-404 prepared in plasma, along with the corresponding linear fitting of the data for relaxation quantification, are shown in **Figure 7.1**. At 4.7T, the measured longitudinal relaxivity (r_1) was between 5.6-5.9 s^{-1}/mM for all preparations, while transverse relaxivity (r_2) varied from 11-21 s^{-1}/mM (**Table 7.1**). In comparison, clinically available T_1-shortening contrast agents such as Magnevist, Prohance, MultiHance, and Dotarem have r_1 values ranging from 2.8-4.0 s^{-1}/mM at 4.7T [126]. The higher r_1 of Gd-DO3A-404 indicates that at the same concentration as the previously mentioned agents, it has more rapid longitudinal relaxation and therefore greater potential for T_1-weighted signal enhancement.

Table 7.1
Relaxivity of Gd-DO3A-404 in saline, excipient, and human plasma at 4.7T

	Relaxivity of Gd-DO3A-404 (s^{-1}/mM)		
	In saline	In excipient	In plasma
r_1	5.68	5.84	5.74
r_2	16.14	11.31	20.36

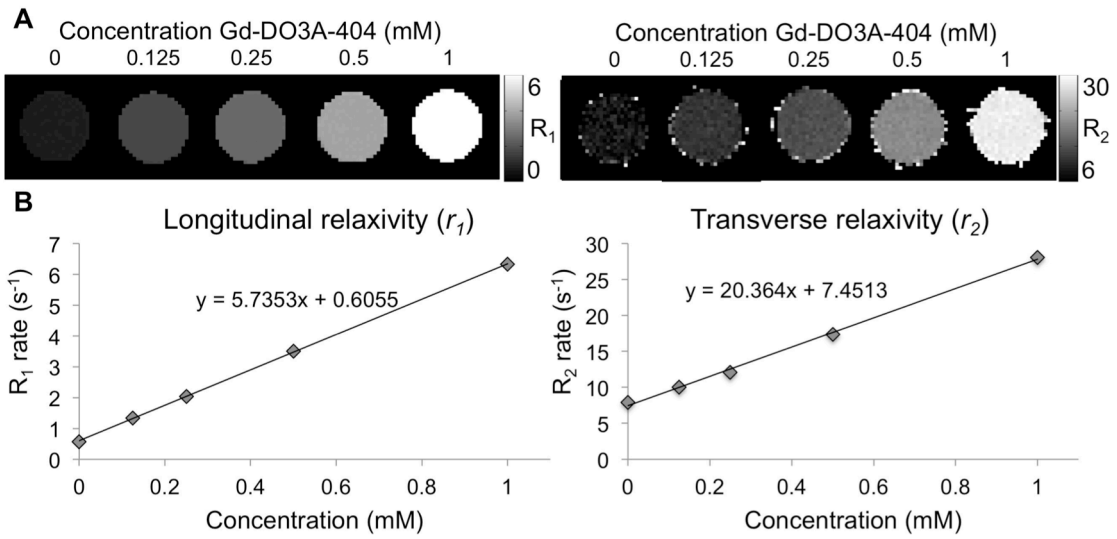

Figure 7.1: Relaxation characteristics of Gd-DO3A-404 in plasma at 4.7T. (A) R1 and R2 relaxation rates increased linearly with concentration of Gd-DO3A-404. (B) Longitudinal and transverse relaxivities of Gd-DO3A-404 were found to be 5.74 and 20.4 s^{-1}/mM, respectively. The increased r1 relaxivity of Gd-DO3A-404 compared to Dotarem (r_1=3.3, r_2=4.7) indicates that at the same concentration, Gd-DO3A-404 has a higher R1 relaxation rate and therefore greater T1-weighted signal enhancement potential.

7.4.2 Flank xenograft imaging

In vivo uptake of Gd-DO3A-404 was initially tested in flank xenografts of two human cancer cell lines, A549 (non-small cell lung cancer) and U87 (glioma). For each tumor model, three nude athymic mice were inoculated with tumor cells in the hind flank and imaging was performed after sufficient tumor growth, 3-6 weeks following inoculation. T_1-weighted MR images and T_1 maps were acquired in all subjects prior to intravenous contrast administration, and imaging was repeated at multiple time points up to seven days. Flank tumors of both models showed tumor-specific enhancement over the course of 24-48 hours following contrast administration (**Figure 7.2**). Significantly sustained enhancement, quantified by tumor to muscle signal ratio, was maintained for up to 4 and 7 days in A549 and U87, respectively. T_1 maps acquired at pre-contrast and 48 hour

time points confirmed that a significant increase in R_1 relaxation rate was observed at 48 hours post-contrast in both tumor models.

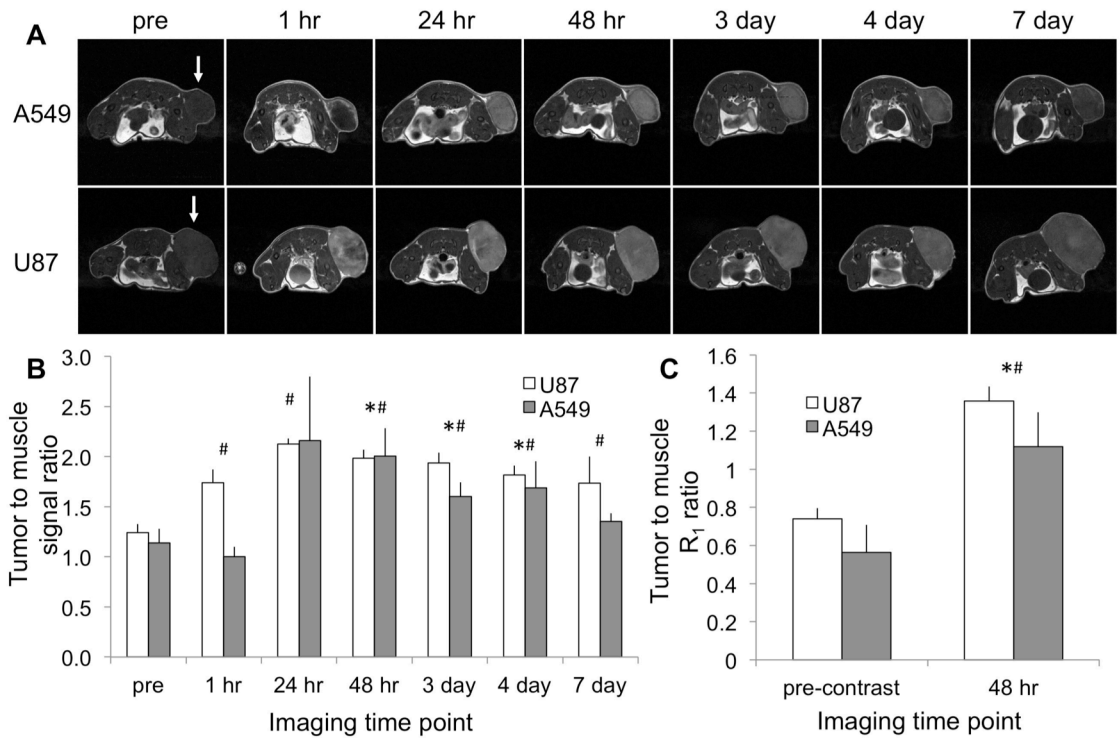

Figure 7.2: Tumor uptake of Gd-DO3A-404 in flank xenografts. (A) Representative T1-weighted images of two tumor models pre-contrast and at multiple time points up to 2 days post-contrast. Tumor location indicated by white arrow. (B) Tumor to muscle ratio of T1-weighted signal increased over the course of 24-48 hours and remained significantly enhanced compared to pre-contrast for up to 4 and 7 days for A549 and U87 xenografts, respectively. Error bars reflect standard deviation among three subjects (*p<0.05 compared to pre-contrast, A549; #p<0.05 compared to pre-contrast, U87). (C) Quantification of R1 relaxation rate revealed a significant increase in R1 time in both tumor models 48 hours after contrast administration.

T_1-weighted imaging volumes of the abdomen were also acquired to observe the uptake of Gd-DO3A-404 in the liver, kidneys, and circulation in the blood. Twenty-four hours following contrast administration, little observable agent remained in circulation (**Figure 7.3A**). High uptake in the liver and kidneys was observed, with maximum liver uptake 24 hours and maximum kidney uptake one hour following contrast administration (**Figure 7.3B and C**). Increased T_1-

weighted signal in the liver (compared to baseline) was maintained until the last imaging time point. In the kidney cortex, increased T_1-weighted signal remained until 4 days post-contrast.

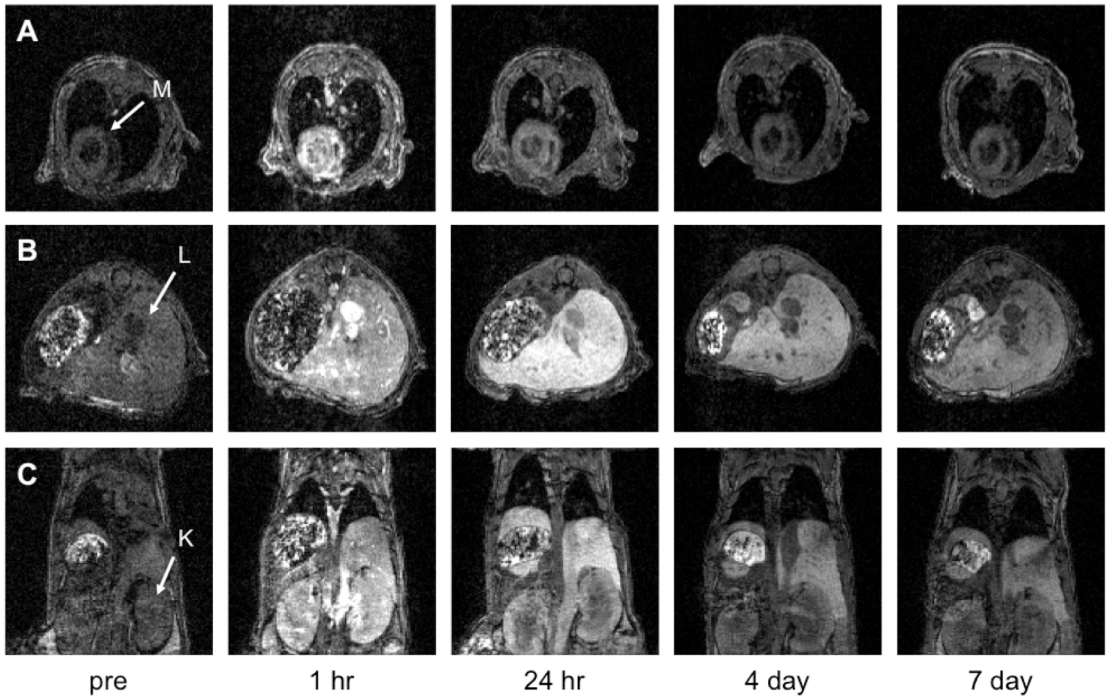

Figure 7.3: Temporal evolution of T_1-weighted signal in the abdomen following administration of Gd-DO3A-404. (A) High signal in the blood is observed one hour post-contrast, with washout by 4 days (M = myocardium). (B) Liver signal enhancement is observed at all time points, with maximum signal observed at 24 hours (L = liver). (C) Kidney signal is enhanced one and 24 hours post-contrast, with more sustained signal enhancement observed in the kidney cortex (K = kidney).

7.4.3 Comparison with Dotarem®

The uptake of Dotarem® (gadoterate meglumine), Gd^{3+} chelated by DOTA, was investigated in mouse hindlimb tumors to compare the temporal dynamics of MRI signal enhancement to those of Gd-DO3A-404. Three nude athymic mice with U87 flank xenografts were scanned with a T_1-weighted sequence prior to administration of Dotarem®, immediately following contrast administration, and at multiple time points up to 24 hours. We observed rapid

tumor uptake of Dotarem® over the course of five minutes, then rapidly reduced T_1-weighted tumor to muscle signal ratio over the course of one hour (**Figure 7.4**). Dotarem® administration increased ratio of tumor to muscle T_1-weighted signal from 1.15 pre-contrast to 1.67 five minutes post-contrast (average of three subjects). In comparison, as a result of Gd-DO3A-404 administration, tumor to muscle signal ratio increased from 1.24 pre-contrast to 2.12 at 24 hours post-contrast.

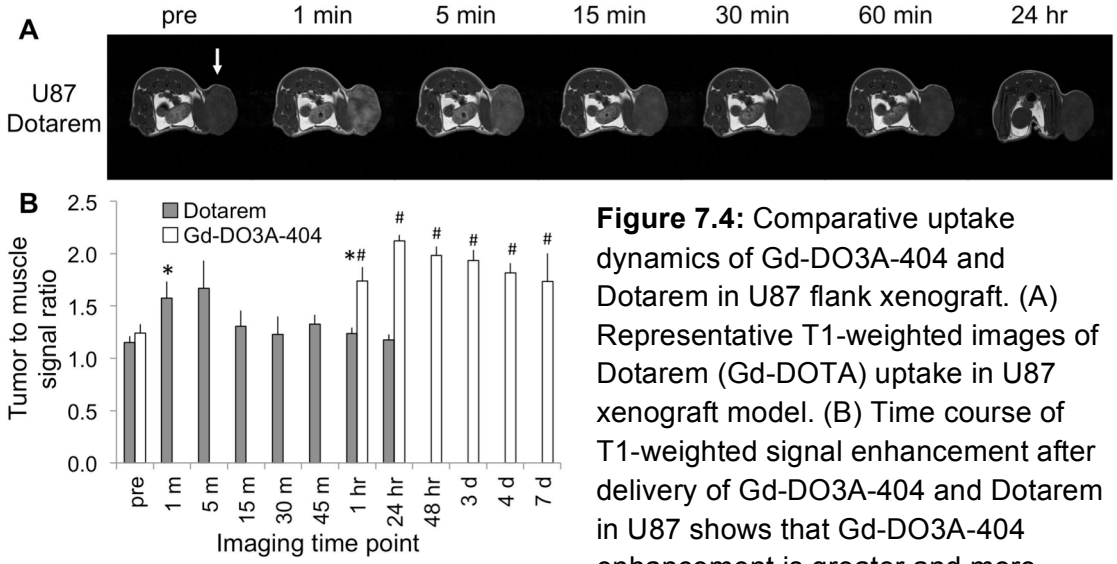

Figure 7.4: Comparative uptake dynamics of Gd-DO3A-404 and Dotarem in U87 flank xenograft. (A) Representative T1-weighted images of Dotarem (Gd-DOTA) uptake in U87 xenograft model. (B) Time course of T1-weighted signal enhancement after delivery of Gd-DO3A-404 and Dotarem in U87 shows that Gd-DO3A-404 enhancement is greater and more prolonged, indicating that uptake reflects specific targeting and incorporation of the contrast agent in cancer cells. (*p<0.05 compared to pre-contrast, Dotarem; $^{\#}p$<0.05 compared to pre-contrast, Gd-DO3A-404.)

7.4.4 Uptake in orthotopic glioma

After observing uptake of Gd-DO3A-404 in two flank tumor xenograft models, we next aimed to observe uptake in an orthotopic glioblastoma model. Glioblastoma stem cells were transplanted into the right striatum of eight NOD/SCID mice. After monitoring tumor growth with T_2-weighted MRI, six subjects were selected for testing Gd-DO3A-404 uptake based on observed

tumor size. In three subjects, 2.5 mg Gd-DO3A-404 was administered via tail vein. T_1-weighted images were acquired and T_1 mapping was performed pre-contrast and at 24, 48, and 72 hours following administration. In these subjects, no uptake was observed in the vicinity of orthotopic tumors (**Figure 4.5A**). Three additional subjects were then administered a higher dose of 3.7 mg Gd-DO3A-404. In one of these three subjects, striking uptake of the agent was observed in a large tumor volume (**Figure 4.6B**).

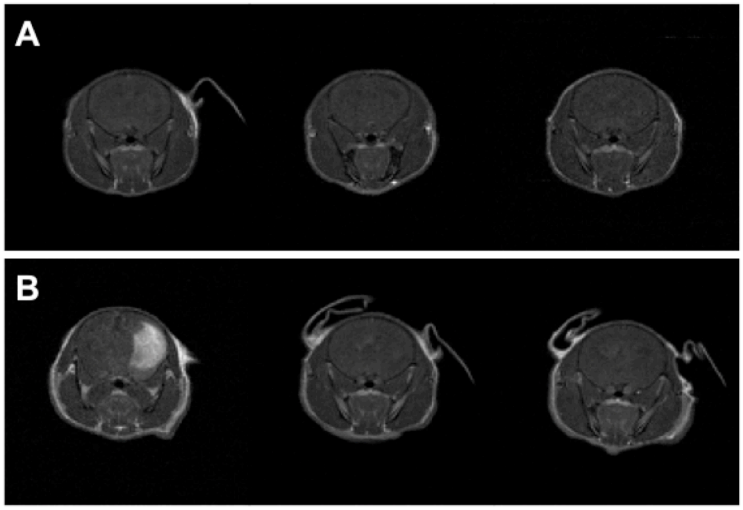

Figure 4.5: Uptake of Gd-DO3A-404 in orthotopic xenografts. Subjects were delivered (A) 2.5 mg or (B) 3.7 mg agent. In only one subject out of six, orthotopic brain tumor xenograft uptake was observed following administration of Gd-DO3A-404. Notably, this was the subject with the largest tumor volume, indicating that blood-brain barrier disruption may be necessary for uptake in brain tumors.

7.5 Discussion

In this work, we have characterized the relaxivity characteristics and *in vivo* targeted uptake of Gd-DO3A-404, a new cancer-targeting MR contrast agent based on APC analog technology [5]. We observed that that with favorable relaxation characteristics and sustained signal-enhancing uptake in multiple tumor models, Gd-DO3A-404 has great potential as a tumor-targeting MR contrast agent.

The effect of Gd-DO3A-404 on relaxation properties of surrounding water protons was characterized at 4.7T with *in vitro* relaxivity measurement of the agent in three formulations (saline, excipient, human plasma). The longitudinal relaxivity of Gd-DO3A-404 at this field strength (5.6-5.9 s^{-1}/mM) is higher than that of clinically available MR contrast agents (2.8-4.0 s^{-1}/mM), indicating that its T_1-weighted signal-enhancing properties may be observable with imaging at lower concentrations [126]. Due to the challenges of delivering high concentrations of targeted agents to tumor cells, this high r_1 may improve likelihood of success of detecting uptake of this targeted agent in tumors. In general, most T_1-shortening contrast agents show improved performance at lower field strengths due to the fact that T_1 time increases with field strength [126]. Therefore, we hypothesize that further characterization of Gd-DO3A-404 at 1.5T and 3.0T field strengths will reveal even more favorable relaxation characteristics at more clinically relevant field strengths.

The transverse relaxivity of Gd-DO3A-404 was also found to be high relative to many clinical T_1-shortening MR contrast agents (11-21 s^{-1}/mM compared to 5-11 s^{-1}/mM) [126]. This indicates that for T_1-weighted imaging of Gd-DO3A-404 uptake, a short echo time (TE) should be used to minimize T_2 relaxation prior to data acquisition. If the agent is in sufficiently high concentration in the imaging volume of interest, and with too long an imaging TE, high r_2 could result in reduced signal. If this challenge is encountered and cannot be resolved with a reduced TE, T_1 mapping could also be used to eliminate the effect of T_2 shortening on observation of Gd-DO3A-404 uptake.

The circulation, organ uptake, and tumor uptake of Gd-DO3A-404 was observed in nude mice with two human tumor models: non-small cell lung cancer (A549) and glioma (U87) flank xenograft. In both tumor models, uptake over a period of 24 hours was observed by T_1-weighted imaging. Additionally, a significant increase in tumor to muscle T_1-weighted signal ratio was observed at multiple time points compared to baseline, from 1 hour to 7 days post-contrast in U87 and from 48 hours to 4 days post-contrast in A549. This slow uptake and prolonged retention of Gd-DO3A-404, compared to the rapid uptake and efflux of Dotarem® observed in U87 flank xenograft, indicates that Gd-DO3A-404 has tumor-targeted and tumor-specific uptake in multiple tumor types. The percent signal enhancement, duration of signal enhancement, and gross observability of Gd-DO3A-404 uptake in these tumor models was striking compared to other tumor-targeted MRI contrast agents in the literature [131-133, 202]. Even in comparison to other reported agents with more notable uptake, this agent uniquely was shown to target more than one tumor type [134-136].

For this agent, along with the tumor-targeting capabilities of APC analogs, specific uptake is further made possible by the 1-2 day circulation time and slow liver and kidney elimination of Gd-DO3A-404, as observed in abdominal T_1-weighted imaging. Due to this long circulation time, in the future it will be essential to experimentally verify high stability of the agent to minimize potential safety concerns of Gd^{3+} deposition.

In initial testing of Gd-DO3A-404 uptake in an orthotopic xenograft model of glioblastoma, mixed results were observed. In only one of six subjects was

signal enhancement observed, but in this subject uptake was striking and covered a large area. Further investigation of the characteristics mediating uptake *in situ*, including tumor size, blood-brain-barrier penetration, and agent dose are required and will be performed in the near future via histology and experimentation with additional orthotopic models.

Thus far, the results of these experiments characterizing the relaxation, uptake, and imaging characteristics of Gd-DO3A-404 indicate great potential for broad-spectrum, high-resolution cancer imaging. However, several essential questions remain to be answered prior to clinical testing of this agent. As previously mentioned, Gd-DO3A-404 relaxivity has yet to be measured at 1.5T and 3.0T. These measurements will be made in the near future, pending availability of sufficient quantities of the prepared agent. In addition, we will measure the stability of the agent at 37°C in plasma. This measurement is essential given the long circulation time of the agent and the potential safety concerns related to dissociation of Gd^{3+} from chelating agents [138-141]. The factors mediating uptake in orthotopic models will be further investigated using histology and, if necessary, additional models (e.g. U87 glioma). Finally, the feasibility of and advantages of simultaneous PET/MR with Gd-DO3A-404 and ^{124}I-CLR1404 will be explored in a large rodent tumor model.

7.6 Conclusion

In conclusion, in this chapter we have performed experiments to test whether targeted contrast-enhanced MR imaging of a variety of tumor types is feasible with Gd-DO3A-404. We have observed relaxation characteristics and, in

particular, tumor-targeting properties that are favorable in comparison with previously proposed targeted MR contrast agents for cancer imaging. In addition, as part of a library of APC analogs labeled with PET/optical tracers and therapeutic radionuclides, Gd-DO3A-404 further expands theranostic capabilities. In all, this agent shows great potential to address current barriers in targeted imaging of cancer.

Chapter 8: Chapters summary and future perspectives

8.1 Chapters summary

This dissertation presents a body of work that establishes new methods and improves on previous methods for quantitative and multi-modal imaging approaches to detecting transplanted stem cells and cancer. In it, an imaging reporter gene system for stem cell tracking with PET and MRI is proposed and tested. This stem cell imaging approach is facilitated by the development of new methods for manganese-based PET and MRI in the rat brain and quantitative MRI experimental design. Finally, molecular and quantitative MRI methods developed and used for stem cell tracking are then applied to the characterization and initial testing of a novel cancer-targeting MRI contrast agent.

The work presented in this dissertation is original research published, submitted for publication, or in preparation for submission in peer-reviewed journals. Chapters 3-7 are original work performed at the University of Wisconsin-Madison between the years of 2012 and 2016. The work presented in chapters 3 and 5 has been published in peer-reviewed journals [34, 175], while that in chapters 4 and 7 are under review and in preparation for submission, respectively.

In the first stage of this work, a new reporter gene system for imaging transplanted stem cells was proposed and tested. Human neural progenitor cells (hNPC) were genetically modified to transiently over-express divalent metal transporter 1 (DMT1) for PET and MRI of specific manganese uptake in labeled cells. In this proof-of-concept work, we observed strikingly increased Mn^{2+} uptake

in DMT1 over-expressing hNPC, and were able to detect stem cells in the rat brain after transplantation (Chapter 3). Next, due to minor challenges encountered in *in vivo* manganese-enhanced MRI and ^{52}Mn PET in Chapter 3, we turned our attention to imaging protocol development. New methods for neuroimaging with ^{52}Mn were developed and tested, and we established safe and effective protocols for manganese enhancement with MRI and PET (Chapter 4). In addition, a method for MRI parameter selection for quantitative T_1 mapping using an error propagation approach was derived and tested with simulations and *ex vivo* T_1 mapping in the brain (Chapter 5). Once these methods had been established, two lines of hNPC stably over-expressing DMT1 ($hNPC^{DMT1}$) were developed and tested for long-term stem cell imaging in the rat brain. These $hNPC^{DMT1}$ lines showed modestly increased Mn^{2+} uptake compared to unmodified hNPC, but this increased uptake was insufficient for *in vivo* stem cell detection (Chapter 6). Last, the protocols and expertise developed throughout this work were applied to the characterization and testing of a newly developed cancer-targeting MRI contrast agent, Gd-DO3A-404 (Chapter 7).

8.2 Knowledge obtained and future perspectives

The work described within this dissertation was pursued in order to address a variety of barriers, challenges, and knowledge gaps in the fields of molecular and quantitative imaging in stem cell therapy and cancer. The results described and conclusions reached have newly addressed some of these gaps and barriers while also posing subsequent hypotheses to be tested.

8.2.1 PET/MRI of hNPC over-expressing DMT1 (Chapters 3 and 6)

The work described in Chapters 3 and 6 was motivated by the need for an effective long-term *in vivo* imaging technique for imaging live stem cells and their progeny after transplantation for treatment of neurodegenerative diseases. If applicable in humans, an effective stem cell imaging method could improve the interpretation of the results of clinical trials currently underway. However, there does not currently exist a safe method for stem cell imaging that is applicable in humans and specific to live cells. The approach described in these chapters aimed to develop a method that (1) was specific to live cells, hence the use of a reporter gene rather than a direct label, (2) was applicable in humans, hence the use of ^{52}Mn for reduced bulk Mn^{2+} dose compared to MRI, (3) was safe, hence the use of a mammalian, ubiquitously expressed reporter protein, and (4) provided the complementary strengths of two clinically applicable imaging modalities.

Our hypothesis that hNPC over-expressing DMT1 take up higher levels of Mn^{2+} and $^{52}Mn^{2+}$ contrast agents was confirmed in these chapters. However, although this increased uptake was sufficient for *in vivo* imaging of hNPC transiently over-expressing DMT1, it was not so in the cells stably over-expressing the reporter protein ($hNPC^{DMT1}$). We hypothesize that this may be due to altered protein structure, expression profile, expression level, or protein function in $hNPC^{DMT1}$. However, the work presented in Chapters 3 and 6 do indicate that, if the level of Mn^{2+} uptake in $hNPC^{DMT1}$ was closer to that of hNPC-DMT1, this approach may successfully address the goals described above.

Although it is outside the scope of this work to investigate the structure and function of DMT1 in $hNPC^{DMT1}$, the further investigation and resolution of this functional difference could allow for the continued development of this stem cell imaging approach. Without this resolution, this *in vivo* cell tracking approach is unlikely to be applicable and translatable as proposed. However, the further investigation of this approach in other stem cell types, such as mesenchymal stem cells or induced pluripotent stem cells, may reveal more broad capabilities and applicability of the approach pursued herein.

Other modifications to this approach may also be worthy of additional investigation. Due to the more rapid Mn^{2+} uptake into cells compared to efflux, pre-labeling of hNPC transiently over-expressing DMT1 with Mn^{2+} or $^{52}Mn^{2+}$ prior to transplantation could permit cell visualization for 1-2 weeks following transplantation [102]. Although this approach is less specific to live cells than the approach pursued in Chapters 3 and 6 of this work, it provides several advantages, including (1) eliminating the need for systemic Mn^{2+} delivery, (2) higher contrast-to-noise ratio (CNR) due to reduced background signal in both MRI and PET, and (3) positive contrast at the location of cells, preferable over the negative contrast provided by nanoparticles commonly used for cell labeling, such as super-paramagnetic iron oxide [73].

Within the field of stem cell tracking, this work presents one of many proposed methods for detecting stem cell location and survival following transplantation. The continued study of direct labeling indicates that non-specific contrast is a confounding factor for cell monitoring [64]. However, our work

illustrates the tradeoff between the technical challenges of and functional information provided by reporter genes for stem cell imaging. The highly specific uptake of Mn^{2+} in hNPC-DMT1 indicates the strong functional information provided by this technique. On the other hand, the challenges encountered in establishing a line of $hNPC^{DMT1}$ with high Mn^{2+} uptake illustrate the more complicated nature of reporter gene-based imaging. Overall, the work presented in this dissertation, along with previous work in our lab, indicates that reporter genes are favorable cell labeling methods [19, 34, 73]. Importantly, their ease of use and clinical applicability is highly dependent on thoughtful selection of safe and translatable imaging methods.

8.2.2 Development of MEMRI, ^{52}Mn PET, and quantitative imaging protocols (Chapters 4 and 5)

The work described in Chapters 4 and 5 was motivated by our need for appropriate, well-established imaging protocols for quantitative MEMRI and ^{52}Mn PET for use in stem cell imaging experiments. In addition, this work aimed to more broadly contribute to the fields of quantitative, molecular, and multimodal imaging by testing new imaging approaches and protocols in a variety of imaging settings.

Although several research groups have described the production and initial application of ^{52}Mn for PET imaging, few have presented work investigating the biodistribution and temporal dynamics of uptake after systemic delivery [33, 35-37]. Our study in Chapter 4 described ^{52}Mn PET in the rat and directly compared the brain uptake of Mn^{2+} contrast agents for MRI and PET. It further

revealed a variety of potentially interesting applications of PET with carrier-added and no carrier-added ^{52}Mn, including imaging of the pancreas, submandibular gland, and joints. The low brain uptake of ^{52}Mn observed after systemic delivery indicated reduced potential for neuroimaging than originally hypothesized. However, these results indicated that alternate delivery methods such as pharmaceutical blood-brain barrier disruption or intrathecal delivery could be worthy of investigation, particularly for preclinical imaging applications. Within the field of novel radiotracer development, this work helps to establish a baseline of knowledge regarding ^{52}Mn applications and limitations, and may be particularly useful for investigators developing ^{52}Mn labeling and targeting strategies [35].

Quantitative T_1 mapping from variable flip angle spoiled gradient echo acquisitions has been investigated in a variety of contexts, but few previous works address experimental design for precise and accurate T_1 estimates in a realistic imaging setting [186-188]. The work described in Chapter 5 aimed to approach experimental design from the theoretical framework of error propagation to minimize T_1 variance. In particular, we aimed to develop an approach that was broadly applicable to any T_1 distribution with any number of acquisition flip angles. The angle selection method proposed and tested in Chapter 5 was found to reduce both the variance and bias of T_1 estimates in simulations and experiments. Interestingly, we found that the flip angles selected using our proposed approach were very similar to those proposed by other researchers using a different selection method [153]. Due to the more involved implementation of our proposed selection technique, we found that the more

simple selection criteria described in [153] was sufficient for the majority of biological imaging tasks. However, the work described in Chapter 5 is highly flexible and applicable to more specialized imaging tasks in which a normal distribution of T_1 values cannot be assumed, and may therefore be particularly useful for unique imaging tasks in a research setting.

8.2.3 Characterization of a broad-spectrum cancer targeting MRI contrast agent (Chapter 7)

The work described in Chapter 7 was motivated by the clinical need for a broad-spectrum cancer targeting MRI contrast agent. Such an agent could facilitate tumor boundary delineation with high spatial resolution, aid in the identification of true tumor progression with MRI, and provide a complementary contrast agent for simultaneous targeted contrast-enhanced PET/MR of cancer. As part of a suite of cancer-targeting agents for *in vivo* imaging, targeted therapy, and surgical guidance, it could greatly expand the capabilities of the APC analog theranostic platform [5].

In Chapter 7, we observed favorable relaxation and tumor-targeting characteristics of Gd-DO3A-404. Specific, sustained uptake of Gd-DO3A-404 was observed in three xenograft models, indicating that this APC analog, like its PET and optical counterparts, is capable of targeted imaging in a wide variety of cancer types. Despite these early successes, the clinical translation of this agent is dependent on several essential studies, which will be performed in the near future. First, although the long circulation time of Gd-DO3A-404 allows for targeted tumor uptake, it could be a safety hazard if the Gd^{3+} is not stably

chelated by the agent. Therefore, agent stability studies will be performed to investigate safety concerns related to the biological consequences of free Gd^{3+} circulation. In addition, we will investigate the application of Gd-DO3A-404 with ^{124}I-CLR1404 for simultaneous PET/MR imaging of cancer. In all, the work in Chapter 7 indicates the great potential of Gd-DO3A-404 for targeted imaging of cancer as part of a multimodality theranostic suite of agents. In comparison with a variety of other targeted MR agents in preclinical development, this agent in particular shows much more striking uptake and retention in tumor models [131-136]. Considering the current clinical testing of APC analogs for imaging and therapy, this strong performance may support rapid clinical translation for theranostic applications [5].

8.3 Conclusions

In this dissertation, novel methods for stem cell detection, cancer imaging, quantitative imaging, and molecular imaging are proposed and tested. This work characterizes improved methods for these applications and contributes to the growing field of *in vivo* imaging of biological and molecular function. The advances described in this work may be widely applicable to a variety of pre-clinical and clinical imaging tasks, and future work will continue to examine the safety, feasibility, and utility of their application in new settings.

Bibliography

1. Lewis CM, Suzuki M. Therapeutic applications of mesenchymal stem cells for amyotrophic lateral sclerosis. Stem Cell Res Ther. 2014; 5: 32.

2. Tadesse T, Gearing M, Senitzer D, et al. Analysis of graft survival in a trial of stem cell transplant in ALS. Ann Clin Transl Neurol. 2014; 1: 900-908.

3. Walczak P, Bulte JW. The role of noninvasive cellular imaging in developing cell-based therapies for neurodegenerative disorders. Neurodegener Dis. 2007; 4: 306-313.

4. Goldstein LS. New frontiers in human cell biology and medicine: can pluripotent stem cells deliver? J Cell Biol. 2012; 199: 577-581.

5. Weichert JP, Clark PA, Kandela IK, et al. Alkylphosphocholine analogs for broad-spectrum cancer imaging and therapy. Sci Transl Med. 2014; 6: 240ra275.

6. Makkar RR, Smith RR, Cheng K, et al. Intracoronary cardiosphere-derived cells for heart regeneration after myocardial infarction (CADUCEUS): a prospective, randomised phase 1 trial. Lancet. 2012; 379: 895-904.

7. Feldman EL, Boulis NM, Hur J, et al. Intraspinal neural stem cell transplantation in amyotrophic lateral sclerosis: phase 1 trial outcomes. Ann Neurol. 2014; 75: 363-373.

8. Mazzini L, Gelati M, Profico DC, et al. Human neural stem cell transplantation in ALS: initial results from a phase I trial. J Transl Med. 2015; 13: 17.

9. Chen H, Qian K, Chen W, et al. Human-derived neural progenitors functionally replace astrocytes in adult mice. J Clin Invest. 2015; 125: 1033-1042.

10. Kang X, Xu H, Teng S, et al. Dopamine release from transplanted neural stem cells in Parkinsonian rat striatum in vivo. Proc Natl Acad Sci U S A. 2014; 111: 15804-15809.

11. Lee HJ, Kim KS, Ahn J, et al. Human motor neurons generated from neural stem cells delay clinical onset and prolong life in ALS mouse model. PLoS One. 2014; 9: e97518.

12. Redmond DE, Jr., Bjugstad KB, Teng YD, et al. Behavioral improvement in a primate Parkinson's model is associated with multiple homeostatic effects of human neural stem cells. Proc Natl Acad Sci U S A. 2007; 104: 12175-12180.

13. Suzuki M, McHugh J, Tork C, et al. GDNF secreting human neural progenitor cells protect dying motor neurons, but not their projection to muscle, in a rat model of familial ALS. PLoS One. 2007; 2: e689.

14. Suzuki M, McHugh J, Tork C, et al. Direct muscle delivery of GDNF with human mesenchymal stem cells improves motor neuron survival and function in a rat model of familial ALS. Mol Ther. 2008; 16: 2002-2010.

15. Krakora D, Mulcrone P, Meyer M, et al. Synergistic Effects of GDNF and VEGF on Lifespan and Disease Progression in a Familial ALS Rat Model. Mol Ther. 2013; 21: 1602-1610.

16. Svendsen CN, ter Borg MG, Armstrong RJ, et al. A new method for the rapid and long term growth of human neural precursor cells. J Neurosci Methods. 1998; 85: 141-152.

17. Capowski EE, Schneider BL, Ebert AD, et al. Lentiviral vector-mediated genetic modification of human neural progenitor cells for ex vivo gene therapy. J Neurosci Methods. 2007; 163: 338-349.

18. Behrstock S, Ebert AD, Klein S, et al. Lesion-induced increase in survival and migration of human neural progenitor cells releasing GDNF. Cell Transplant. 2008; 17: 753-762.

19. Bernau K, Lewis CM, Petelinsek AM, et al. In vivo tracking of human neural progenitor cells in the rat brain using bioluminescence imaging. J Neurosci Methods. 2014; 228: 67-78.

20. Hassani Z, O'Reilly J, Pearse Y, et al. Human neural progenitor cell engraftment increases neurogenesis and microglial recruitment in the brain of rats with stroke. PLoS One. 2012; 7: e50444.

21. Ahrens ET, Helfer BM, O'Hanlon CF, et al. Clinical cell therapy imaging using a perfluorocarbon tracer and fluorine-19 MRI. Magn Reson Med. 2014; 72: 1696-1701.

22. Janowski M, Walczak P, Kropiwnicki T, et al. Long-term MRI cell tracking after intraventricular delivery in a patient with global cerebral ischemia and prospects for magnetic navigation of stem cells within the CSF. PLoS One. 2014; 9: e97631.

23. Mattis VB, Wakeman DR, Tom C, et al. Neonatal immune-tolerance in mice does not prevent xenograft rejection. Exp Neurol. 2014; 254: 90-98.

24. Regge D, Cirillo S, Macera A, et al. Mangafodipir trisodium: review of its use as an injectable contrast medium for magnetic resonance imaging. Rep Med Imaging. 2009; 2: 55-68.

25. Massaad CA, Pautler RG. Manganese-enhanced magnetic resonance imaging (MEMRI). Methods Mol Biol. 2011; 711: 145-174.

26. Suero-Abreu GA, Praveen Raju G, Aristizabal O, et al. In vivo Mn-enhanced MRI for early tumor detection and growth rate analysis in a mouse medulloblastoma model. Neoplasia. 2014; 16: 993-1006.

27. Kim PJ, Mahmoudi M, Ge X, et al. Direct evaluation of myocardial viability and stem cell engraftment demonstrates salvage of the injured myocardium. Circ Res. 2015; 116: e40-50.

28. Pan D, Caruthers SD, Senpan A, et al. Revisiting an old friend: manganese-based MRI contrast agents. Wiley Interdiscip Rev Nanomed Nanobiotechnol. 2011; 3: 162-173.

29. Au C, Benedetto A, Aschner M. Manganese transport in eukaryotes: the role of DMT1. Neurotoxicology. 2008; 29: 569-576.

30. Nordhoy W, Anthonsen HW, Bruvold M, et al. Manganese ions as intracellular contrast agents: proton relaxation and calcium interactions in rat myocardium. NMR Biomed. 2003; 16: 82-95.

31. Bruvold M, Nordhoy W, Anthonsen HW, et al. Manganese-calcium interactions with contrast media for cardiac magnetic resonance imaging: a study of manganese chloride supplemented with calcium gluconate in isolated Guinea pig hearts. Invest Radiol. 2005; 40: 117-125.

32. Silva AC, Lee JH, Aoki I, et al. Manganese-enhanced magnetic resonance imaging (MEMRI): methodological and practical considerations. NMR Biomed. 2004; 17: 532-543.

33. Topping GJ, Schaffer P, Hoehr C, et al. Manganese-52 positron emission tomography tracer characterization and initial results in phantoms and in vivo. Med Phys. 2013; 40: 042502.

34. Lewis CM, Graves SA, Hernandez R, et al. (52)Mn Production for PET/MRI Tracking Of Human Stem Cells Expressing Divalent Metal Transporter 1 (DMT1). Theranostics. 2015; 5: 227-239.

35. Graves SA, Hernandez R, Fonslet J, et al. Novel Preparation Methods of (52)Mn for ImmunoPET Imaging. Bioconjug Chem. 2015; 26: 2118-2124.

36. Wooten AL, Lewis BC, Lapi SE. Cross-sections for (p,x) reactions on natural chromium for the production of (52,52m,54)Mn radioisotopes. Appl Radiat Isot. 2015; 96: 154-161.

37. Daube ME, Nickles RJ. Development of myocardial perfusion tracers for positron emission tomography. Int J Nucl Med Biol. 1985; 12: 303-314.

38. Buchholz M, Spahn I, Coenen HH. Optimized separation procedure for production of no-carrier-added radiomanganese for positron emission tomography. Radiochimica Acta. 2015; 103: 893-899.

39. Deri MA, Zeglis BM, Francesconi LC, et al. PET imaging with (8)(9)Zr: from radiochemistry to the clinic. Nucl Med Biol. 2013; 40: 3-14.

40. Shokeen M, Wadas TJ. The development of copper radiopharmaceuticals for imaging and therapy. Med Chem. 2011; 7: 413-429.

41. Torigian DA, Zaidi H, Kwee TC, et al. PET/MR imaging: technical aspects and potential clinical applications. Radiology. 2013; 267: 26-44.

42. Guillet-Nicolas R, Laprise-Pelletier M, Nair MM, et al. Manganese-impregnated mesoporous silica nanoparticles for signal enhancement in MRI cell labelling studies. Nanoscale. 2013; 5: 11499-11511.

43. Yamada M, Gurney PT, Chung J, et al. Manganese-guided cellular MRI of human embryonic stem cell and human bone marrow stromal cell viability. Magn Reson Med. 2009; 62: 1047-1054.

44. Odaka K, Aoki I, Moriya J, et al. In vivo tracking of transplanted mononuclear cells using manganese-enhanced magnetic resonance imaging (MEMRI). PLoS One. 2011; 6: e25487.

45. Jaffray DA, Chung C, Coolens C, et al. Quantitative Imaging in Radiation Oncology: An Emerging Science and Clinical Service. Semin Radiat Oncol. 2015; 25: 292-304.

46. Maeda H. Tumor-selective delivery of macromolecular drugs via the EPR effect: background and future prospects. Bioconjug Chem. 2010; 21: 797-802.

47. James ML, Gambhir SS. A molecular imaging primer: modalities, imaging agents, and applications. Physiol Rev. 2012; 92: 897-965.

48. Sipkins DA, Cheresh DA, Kazemi MR, et al. Detection of tumor angiogenesis in vivo by alphaVbeta3-targeted magnetic resonance imaging. Nat Med. 1998; 4: 623-626.

49. Xue S, Yang H, Qiao J, et al. Protein MRI contrast agent with unprecedented metal selectivity and sensitivity for liver cancer imaging. Proc Natl Acad Sci U S A. 2015; 112: 6607-6612.

50. Park JA, Lee JJ, Jung JC, et al. Gd-DOTA conjugate of RGD as a potential tumor-targeting MRI contrast agent. Chembiochem. 2008; 9: 2811-2813.

51. Ye F, Wu X, Jeong EK, et al. A peptide targeted contrast agent specific to fibrin-fibronectin complexes for cancer molecular imaging with MRI. Bioconjug Chem. 2008; 19: 2300-2303.

52. Tennstaedt A, Aswendt M, Adamczak J, et al. Human neural stem cell intracerebral grafts show spontaneous early neuronal differentiation after several weeks. Biomaterials. 2015; 44: 143-154.

53. Naumova AV, Modo M, Moore A, et al. Clinical imaging in regenerative medicine. Nat Biotechnol. 2014; 32: 804-818.

54. Richards JM, Shaw CA, Lang NN, et al. In vivo mononuclear cell tracking using superparamagnetic particles of iron oxide: feasibility and safety in humans. Circ Cardiovasc Imaging. 2012; 5: 509-517.

55. Li L, Jiang W, Luo K, et al. Superparamagnetic iron oxide nanoparticles as MRI contrast agents for non-invasive stem cell labeling and tracking. Theranostics. 2013; 3: 595-615.

56. Lee S, Chen X. Dual-modality probes for in vivo molecular imaging. Mol Imaging. 2009; 8: 87-100.

57. Chen YC, Wen S, Shang SA, et al. Magnetic resonance and near-infrared imaging using a novel dual-modality nano-probe for dendritic cell tracking in vivo. Cytotherapy. 2014; 16: 699-710.

58. Lang C, Lehner S, Todica A, et al. Positron emission tomography based in-vivo imaging of early phase stem cell retention after intramyocardial delivery in the mouse model. Eur J Nucl Med Mol Imaging. 2013; 40: 1730-1738.

59. Arbab AS, Thiffault C, Navia B, et al. Tracking of In-111-labeled human umbilical tissue-derived cells (hUTC) in a rat model of cerebral ischemia using SPECT imaging. BMC Med Imaging. 2012; 12: 33.

60. Bansal A, Pandey MK, Demirhan YE, et al. Novel (89)Zr cell labeling approach for PET-based cell trafficking studies. EJNMMI Res. 2015; 5: 19.

61. Sato N, Wu H, Asiedu KO, et al. (89)Zr-Oxine Complex PET Cell Imaging in Monitoring Cell-based Therapies. Radiology. 2015; 275: 490-500.

62. Huang Z, Li C, Yang S, et al. Magnetic resonance hypointensive signal primarily originates from extracellular iron particles in the long-term tracking of mesenchymal stem cells transplanted in the infarcted myocardium. Int J Nanomedicine. 2015; 10: 1679-1690.

63. Ma N, Cheng H, Lu M, et al. Magnetic resonance imaging with superparamagnetic iron oxide fails to track the long-term fate of mesenchymal stem cells transplanted into heart. Sci Rep. 2015; 5: 9058.

64. Cianciaruso C, Pagani A, Martelli C, et al. Cellular magnetic resonance with iron oxide nanoparticles: long-term persistence of SPIO signal in the CNS after transplanted cell death. Nanomedicine (Lond). 2014: 1-18.

65. Ahn BC, Parashurama N, Patel M, et al. Noninvasive Reporter Gene Imaging of Human Oct4 (Pluripotency) Dynamics During the Differentiation of Embryonic Stem Cells in Living Subjects. Mol Imaging Biol. 2014.

66. Perin EC, Tian M, Marini FC, 3rd, et al. Imaging long-term fate of intramyocardially implanted mesenchymal stem cells in a porcine myocardial infarction model. PLoS One. 2011; 6: e22949.

67. Niu G, Chen X. Molecular imaging with activatable reporter systems. Theranostics. 2012; 2: 413-423.

68. Nguyen PK, Riegler J, Wu JC. Stem cell imaging: from bench to bedside. Cell Stem Cell. 2014; 14: 431-444.

69. Yang H, Wang H, Shivalila CS, et al. One-step generation of mice carrying reporter and conditional alleles by CRISPR/Cas-mediated genome engineering. Cell. 2013; 154: 1370-1379.

70. Cormode DP, Naha PC, Fayad ZA. Nanoparticle contrast agents for computed tomography: a focus on micelles. Contrast Media Mol Imaging. 2014; 9: 37-52.

71. Betzer O, Shwartz A, Motiei M, et al. Nanoparticle-based CT imaging technique for longitudinal and quantitative stem cell tracking within the brain: application in neuropsychiatric disorders. ACS Nano. 2014; 8: 9274-9285.

72. Mallidi SW, B.; Mehrmohammadi, M.; Qu, M.; Chen, Y.-S.; Joshi, P.; Kim, S.; Homan, K.A.; Karpiouk, A.B.; Smalling, R.W.; Skolov, K.; Emelianov, S.Y. Ultrasound-based imaging of nanoparticles: From molecular and cellular

imaging to therapy guidance. IEEE International Ultrasonics Symposium Proceedings. 2009; 8: 28-36.

73. Bernau K, Lewis CM, Petelinsek AM, et al. In Vivo Tracking of Human Neural Progenitor Cells in the Rat Brain Using Magnetic Resonance Imaging is Not Enhanced by Ferritin Expression. Cell Transplant. 2015.

74. Gaudet JM, Ribot EJ, Chen Y, et al. Tracking the fate of stem cell implants with fluorine-19 MRI. PLoS One. 2015; 10: e0118544.

75. Chung J, Yamada M, Yang PC. Magnetic resonance imaging of human embryonic stem cells. Curr Protoc Stem Cell Biol. 2009; Chapter 5: Unit 5A 3.

76. Makela T, Takalo R, Arvola O, et al. Safety and biodistribution study of bone marrow-derived mesenchymal stromal cells and mononuclear cells and the impact of the administration route in an intact porcine model. Cytotherapy. 2015; 17: 392-402.

77. Charoenphun P, Meszaros LK, Chuamsaamarkkee K, et al. [(89)Zr]oxinate4 for long-term in vivo cell tracking by positron emission tomography. Eur J Nucl Med Mol Imaging. 2015; 42: 278-287.

78. Aswendt M, Adamczak J, Couillard-Despres S, et al. Boosting bioluminescence neuroimaging: an optimized protocol for brain studies. PLoS One. 2013; 8: e55662.

79. Oh HJ, Hwang do W, Youn H, et al. In vivo bioluminescence reporter gene imaging for the activation of neuronal differentiation induced by the neuronal activator neurogenin 1 (Ngn1) in neuronal precursor cells. Eur J Nucl Med Mol Imaging. 2013; 40: 1607-1617.

80. Pan Y, Yin H, Lv J, et al. A novel hybrid baculovirus-adeno-associated viral vector-mediated radionuclide reporter gene imaging system for stem cells transplantation monitoring. Appl Microbiol Biotechnol. 2015; 99: 1415-1426.

81. Goethals LR, Bos TJ, Baeyens L, et al. Camelid reporter gene imaging: a generic method for in vivo cell tracking. EJNMMI Res. 2014; 4: 32.

82. Levin RA, Felsen CN, Yang J, et al. An optimized triple modality reporter for quantitative in vivo tumor imaging and therapy evaluation. PLoS One. 2014; 9: e97415.

83. Cho IK, Moran SP, Paudyal R, et al. Longitudinal monitoring of stem cell grafts in vivo using magnetic resonance imaging with inducible maga as a genetic reporter. Theranostics. 2014; 4: 972-989.

84. Kim HS, Woo J, Choi Y, et al. Noninvasive MRI and multilineage differentiation capability of ferritin-transduced human mesenchymal stem cells. NMR Biomed. 2015; 28: 168-179.

85. Kim HS, Woo J, Lee JH, et al. In vivo Tracking of Dendritic Cell using MRI Reporter Gene, Ferritin. PLoS One. 2015; 10: e0125291.

86. Deans AE, Wadghiri YZ, Bernas LM, et al. Cellular MRI contrast via coexpression of transferrin receptor and ferritin. Magn Reson Med. 2006; 56: 51-59.

87. Patrick PS, Rodrigues TB, Kettunen MI, et al. Development of Timd2 as a reporter gene for MRI. Magn Reson Med. 2015.

88. Bartelle BB, Szulc KU, Suero-Abreu GA, et al. Divalent metal transporter, DMT1: A novel MRI reporter protein. Magn Reson Med. 2012.

89. Bartelle BB, Mana MD, Suero-Abreu GA, et al. Engineering an effective Mn-binding MRI reporter protein by subcellular targeting. Magn Reson Med. 2014.

90. Sherry AD, Woods M. Chemical exchange saturation transfer contrast agents for magnetic resonance imaging. Annu Rev Biomed Eng. 2008; 10: 391-411.

91. Gilad AA, McMahon MT, Walczak P, et al. Artificial reporter gene providing MRI contrast based on proton exchange. Nat Biotechnol. 2007; 25: 217-219.

92. Bar-Shir A, Liu G, Greenberg MM, et al. Synthesis of a probe for monitoring HSV1-tk reporter gene expression using chemical exchange saturation transfer MRI. Nat Protoc. 2013; 8: 2380-2391.

93. Bar-Shir A, Liu G, Chan KW, et al. Human protamine-1 as an MRI reporter gene based on chemical exchange. ACS Chem Biol. 2014; 9: 134-138.

94. Minn I, Bar-Shir A, Yarlagadda K, et al. Tumor-specific expression and detection of a CEST reporter gene. Magn Reson Med. 2015.

95. Hickey RD, Mao SA, Amiot B, et al. Noninvasive 3-dimensional imaging of liver regeneration in a mouse model of hereditary tyrosinemia type 1 using the sodium iodide symporter gene. Liver Transpl. 2015; 21: 442-453.

96. Yaghoubi SS, Jensen MC, Satyamurthy N, et al. Noninvasive detection of therapeutic cytolytic T cells with 18F-FHBG PET in a patient with glioma. Nat Clin Pract Oncol. 2009; 6: 53-58.

97. Qin C, Lan X, He J, et al. An in vitro and in vivo evaluation of a reporter gene/probe system hERL/(18)F-FES. PLoS One. 2013; 8: e61911.

98. Schonitzer V, Haasters F, Kasbauer S, et al. In Vivo Mesenchymal Stem Cell Tracking with PET Using the Dopamine Type 2 Receptor and 18F-Fallypride. J Nucl Med. 2014; 55: 1342-1347.

99. Patrick PS, Hammersley J, Loizou L, et al. Dual-modality gene reporter for in vivo imaging. Proc Natl Acad Sci U S A. 2014; 111: 415-420.

100. Nejadnik H, Ye D, Lenkov OD, et al. Magnetic resonance imaging of stem cell apoptosis in arthritic joints with a caspase activatable contrast agent. ACS Nano. 2015; 9: 1150-1160.

101. Illing AC, Shawki A, Cunningham CL, et al. Substrate profile and metal-ion selectivity of human divalent metal-ion transporter-1. J Biol Chem. 2012; 287: 30485-30496.

102. Tuschl K, Mills PB, Clayton PT. Manganese and the brain. Int Rev Neurobiol. 2013; 110: 277-312.

103. Garrick MD, Dolan KG, Horbinski C, et al. DMT1: a mammalian transporter for multiple metals. Biometals. 2003; 16: 41-54.

104. Gruenheid S, Canonne-Hergaux F, Gauthier S, et al. The iron transport protein NRAMP2 is an integral membrane glycoprotein that colocalizes with transferrin in recycling endosomes. J Exp Med. 1999; 189: 831-841.

105. Shawki A, Knight PB, Maliken BD, et al. H(+)-coupled divalent metal-ion transporter-1: functional properties, physiological roles and therapeutics. Curr Top Membr. 2012; 70: 169-214.

106. Garcia SJ, Gellein K, Syversen T, et al. A manganese-enhanced diet alters brain metals and transporters in the developing rat. Toxicol Sci. 2006; 92: 516-525.

107. Tamm C, Sabri F, Ceccatelli S. Mitochondrial-mediated apoptosis in neural stem cells exposed to manganese. Toxicol Sci. 2008; 101: 310-320.

108. Ba LA, Doering M, Burkholz T, et al. Metal trafficking: from maintaining the metal homeostasis to future drug design. Metallomics. 2009; 1: 292-311.

109. Salazar J, Mena N, Hunot S, et al. Divalent metal transporter 1 (DMT1) contributes to neurodegeneration in animal models of Parkinson's disease. Proc Natl Acad Sci U S A. 2008; 105: 18578-18583.

110. Aoki I, Wu YJ, Silva AC, et al. In vivo detection of neuroarchitecture in the rodent brain using manganese-enhanced MRI. Neuroimage. 2004; 22: 1046-1059.

111. Lin YJ, Koretsky AP. Manganese ion enhances T1-weighted MRI during brain activation: an approach to direct imaging of brain function. Magn Reson Med. 1997; 38: 378-388.

112. Pautler RG, Silva AC, Koretsky AP. In vivo neuronal tract tracing using manganese-enhanced magnetic resonance imaging. Magn Reson Med. 1998; 40: 740-748.

113. Kikuta S, Nakamura Y, Yamamura Y, et al. Quantitative activation-induced manganese-enhanced MRI reveals severity of Parkinson's disease in mice. Sci Rep. 2015; 5: 12800.

114. Jiang Y, Zheng W. Cardiovascular toxicities upon manganese exposure. Cardiovasc Toxicol. 2005; 5: 345-354.

115. Wendland MF. Applications of manganese-enhanced magnetic resonance imaging (MEMRI) to imaging of the heart. NMR Biomed. 2004; 17: 581-594.

116. Eschenko O, Canals S, Simanova I, et al. Behavioral, electrophysiological and histopathological consequences of systemic manganese administration in MEMRI. Magn Reson Imaging. 2010; 28: 1165-1174.

117. Chen P, Chakraborty S, Peres TV, et al. Manganese-induced Neurotoxicity: From C. Elegans to Humans. Toxicol Res (Camb). 2015; 4: 191-202.

118. Crossgrove J, Zheng W. Manganese toxicity upon overexposure. NMR Biomed. 2004; 17: 544-553.

119. Weissleder R, Pittet MJ. Imaging in the era of molecular oncology. Nature. 2008; 452: 580-589.

120. Lohrke J, Frenzel T, Endrikat J, et al. 25 Years of Contrast-Enhanced MRI: Developments, Current Challenges and Future Perspectives. Adv Ther. 2016; 33: 1-28.

121. Claussen C, Laniado M, Schorner W, et al. Gadolinium-DTPA in MR imaging of glioblastomas and intracranial metastases. AJNR Am J Neuroradiol. 1985; 6: 669-674.

122. Creasy JL, Price RR, Presbrey T, et al. Gadolinium-enhanced MR angiography. Radiology. 1990; 175: 280-283.

123. Knopp MV, Giesel FL, Marcos H, et al. Dynamic contrast-enhanced magnetic resonance imaging in oncology. Top Magn Reson Imaging. 2001; 12: 301-308.

124. Huppertz A, Balzer T, Blakeborough A, et al. Improved detection of focal liver lesions at MR imaging: multicenter comparison of gadoxetic acid-enhanced MR images with intraoperative findings. Radiology. 2004; 230: 266-275.

125. Toy R, Bauer L, Hoimes C, et al. Targeted nanotechnology for cancer imaging. Adv Drug Deliv Rev. 2014; 76: 79-97.

126. Rohrer M, Bauer H, Mintorovitch J, et al. Comparison of magnetic properties of MRI contrast media solutions at different magnetic field strengths. Invest Radiol. 2005; 40: 715-724.

127. Zarrin A, Sadighian S, Rostamizadeh K, et al. Design, preparation, and in vitro characterization of a trimodally-targeted nanomagnetic onco-theranostic system for cancer diagnosis and therapy. Int J Pharm. 2016; 500: 62-76.

128. Haribabu V, Farook AS, Goswami N, et al. Optimized Mn-doped iron oxide nanoparticles entrapped in dendrimer for dual contrasting role in MRI. J Biomed Mater Res B Appl Biomater. 2015.

129. Zhang K, Liu M, Tong X, et al. Aptamer-Modified Temperature-Sensitive Liposomal Contrast Agent for Magnetic Resonance Imaging. Biomacromolecules. 2015; 16: 2618-2623.

130. Wu M, Zhang D, Zeng Y, et al. Nanocluster of superparamagnetic iron oxide nanoparticles coated with poly (dopamine) for magnetic field-targeting, highly sensitive MRI and photothermal cancer therapy. Nanotechnology. 2015; 26: 115102.

131. Abakumova T, Abakumov M, Shein S, et al. Connexin 43-targeted T1 contrast agent for MRI diagnosis of glioma. Contrast Media Mol Imaging. 2016; 11: 15-23.

132. Huang H, Yue T, Xu K, et al. Fabrication and evaluation of tumor-targeted positive MRI contrast agent based on ultrasmall MnO nanoparticles. Colloids Surf B Biointerfaces. 2015; 131: 148-154.

133. Liu X, Madhankumar AB, Miller PA, et al. MRI contrast agent for targeting glioma: interleukin-13 labeled liposome encapsulating gadolinium-DTPA. Neuro Oncol. 2015.

134. Pu F, Qiao J, Xue S, et al. GRPR-targeted Protein Contrast Agents for Molecular Imaging of Receptor Expression in Cancers by MRI. Sci Rep. 2015; 5: 16214.

135. Tong X, Liu M, Zhang K, et al. Oligoethylenimine-grafted chitosan as enhanced T contrast agent for in vivo targeted tumor MRI. J Magn Reson Imaging. 2015.

136. Zhou Z, Qutaish M, Han Z, et al. MRI detection of breast cancer micrometastases with a fibronectin-targeting contrast agent. Nat Commun. 2015; 6: 7984.

137. Chen R, Ling D, Zhao L, et al. Parallel Comparative Studies on Mouse Toxicity of Oxide Nanoparticle- and Gadolinium-Based T1 MRI Contrast Agents. ACS Nano. 2015; 9: 12425-12435.

138. Marckmann P, Skov L, Rossen K, et al. Nephrogenic systemic fibrosis: suspected causative role of gadodiamide used for contrast-enhanced magnetic resonance imaging. J Am Soc Nephrol. 2006; 17: 2359-2362.

139. McDonald RJ, McDonald JS, Kallmes DF, et al. Intracranial Gadolinium Deposition after Contrast-enhanced MR Imaging. Radiology. 2015; 275: 772-782.

140. Morcos SK. Extracellular gadolinium contrast agents: differences in stability. Eur J Radiol. 2008; 66: 175-179.

141. Frenzel T, Lengsfeld P, Schirmer H, et al. Stability of gadolinium-based magnetic resonance imaging contrast agents in human serum at 37 degrees C. Invest Radiol. 2008; 43: 817-828.

142. Snyder F, Wood R. Alkyl and alk-1-enyl ethers of glycerol in lipids from normal and neoplastic human tissues. Cancer Res. 1969; 29: 251-257.

143. Counsell RE, Schwendner SW, Meyer KL, et al. Tumor visualization with a radioiodinated phospholipid ether. J Nucl Med. 1990; 31: 332-336.

144. Gajate C, Mollinedo F. Biological activities, mechanisms of action and biomedical prospect of the antitumor ether phospholipid ET-18-OCH(3) (edelfosine), a proapoptotic agent in tumor cells. Curr Drug Metab. 2002; 3: 491-525.

145. Kuerschner L, Richter D, Hannibal-Bach HK, et al. Exogenous ether lipids predominantly target mitochondria. PLoS One. 2012; 7: e31342.

146. van Blitterswijk WJ, Verheij M. Anticancer mechanisms and clinical application of alkylphospholipids. Biochim Biophys Acta. 2013; 1831: 663-674.

147. Li YC, Park MJ, Ye SK, et al. Elevated levels of cholesterol-rich lipid rafts in cancer cells are correlated with apoptosis sensitivity induced by cholesterol-depleting agents. Am J Pathol. 2006; 168: 1107-1118; quiz 1404-1105.

148. Pinchuk AN, Rampy MA, Longino MA, et al. Synthesis and structure-activity relationship effects on the tumor avidity of radioiodinated phospholipid ether analogues. J Med Chem. 2006; 49: 2155-2165.

149. Korb ML, Warram JM, Grudzinski J, et al. Breast Cancer Imaging Using the Near-Infrared Fluorescent Agent, CLR1502. Molecular imaging. 2014; 13: 1-9.

150. Swanson KI, Clark PA, Zhang RR, et al. Fluorescent Cancer-Selective Alkylphosphocholine Analogs for Intraoperative Glioma Detection. Neurosurgery. 2015; 76: 115-124.

151. Boretius S, Frahm J. Manganese-enhanced magnetic resonance imaging. Methods Mol Biol. 2011; 771: 531-568.

152. Wooten AL, Lewis BC, Laforest R, et al. Cyclotron production and PET/MR imaging of 52Mn. Proceedings of the 15th International Workshop on Targetry and Target Chemistry. 2014.

153. Deoni SC, Rutt BK, Peters TM. Rapid combined T1 and T2 mapping using gradient recalled acquisition in the steady state. Magn Reson Med. 2003; 49: 515-526.

154. Rivera-Mancia S, Rios C, Montes S. Manganese accumulation in the CNS and associated pathologies. Biometals. 2011; 24: 811-825.

155. Chuang KH, Koretsky AP, Sotak CH. Temporal changes in the T1 and T2 relaxation rates (DeltaR1 and DeltaR2) in the rat brain are consistent with

the tissue-clearance rates of elemental manganese. Magn Reson Med. 2009; 61: 1528-1532.

156. Koretsky AP, Silva AC. Manganese-enhanced magnetic resonance imaging (MEMRI). NMR Biomed. 2004; 17: 527-531.

157. Bade AN, Zhou B, McMillan J, et al. Potential of N-acetylated-para-aminosalicylic acid to accelerate manganese enhancement decline for long-term MEMRI in rodent brain. J Neurosci Methods. 2015; 251: 92-98.

158. Liu CH, D'Arceuil HE, de Crespigny AJ. Direct CSF injection of MnCl(2) for dynamic manganese-enhanced MRI. Magn Reson Med. 2004; 51: 978-987.

159. Canals S, Beyerlein M, Keller AL, et al. Magnetic resonance imaging of cortical connectivity in vivo. Neuroimage. 2008; 40: 458-472.

160. Lee JH, Silva AC, Merkle H, et al. Manganese-enhanced magnetic resonance imaging of mouse brain after systemic administration of MnCl2: dose-dependent and temporal evolution of T1 contrast. Magn Reson Med. 2005; 53: 640-648.

161. Ni Y, Petre C, Bosmans H, et al. Comparison of manganese biodistribution and MR contrast enhancement in rats after intravenous injection of MnDPDP and MnCl2. Acta Radiol. 1997; 38: 700-707.

162. Crossgrove JS, Allen DD, Bukaveckas BL, et al. Manganese distribution across the blood-brain barrier. I. Evidence for carrier-mediated influx of managanese citrate as well as manganese and manganese transferrin. Neurotoxicology. 2003; 24: 3-13.

163. Aschner M. The transport of manganese across the blood-brain barrier. Neurotoxicology. 2006; 27: 311-314.

164. Yokel RA. Manganese flux across the blood-brain barrier. Neuromolecular Med. 2009; 11: 297-310.

165. Murphy VA, Wadhwani KC, Smith QR, et al. Saturable transport of manganese(II) across the rat blood-brain barrier. J Neurochem. 1991; 57: 948-954.

166. Yarnykh VL. Actual flip-angle imaging in the pulsed steady state: a method for rapid three-dimensional mapping of the transmitted radiofrequency field. Magn Reson Med. 2007; 57: 192-200.

167. Chang LC, Koay CG, Basser PJ, et al. Linear least-squares method for unbiased estimation of T1 from SPGR signals. Magn Reson Med. 2008; 60: 496-501.

168. Jenkinson M, Smith S. A global optimisation method for robust affine registration of brain images. Med Image Anal. 2001; 5: 143-156.

169. Jenkinson M, Bannister P, Brady M, et al. Improved optimization for the robust and accurate linear registration and motion correction of brain images. Neuroimage. 2002; 17: 825-841.

170. Papp EA, Leergaard TB, Calabrese E, et al. Waxholm Space atlas of the Sprague Dawley rat brain. Neuroimage. 2014; 97: 374-386.

171. Kjonigsen LJ, Lillehaug S, Bjaalie JG, et al. Waxholm Space atlas of the rat brain hippocampal region: three-dimensional delineations based on magnetic resonance and diffusion tensor imaging. Neuroimage. 2015; 108: 441-449.

172. Sergejeva M, Papp EA, Bakker R, et al. Anatomical landmarks for registration of experimental image data to volumetric rodent brain atlasing templates. J Neurosci Methods. 2015; 240: 161-169.

173. Zaidi H, Koral KF. Scatter modelling and compensation in emission tomography. Eur J Nucl Med Mol Imaging. 2004; 31: 761-782.

174. Takeda A, Sawashita J, Okada S. Biological half-lives of zinc and manganese in rat brain. Brain Res. 1995; 695: 53-58.

175. Lewis CM, Hurley SA, Meyerand ME, et al. Data-driven optimized flip angle selection for T estimation from spoiled gradient echo acquisitions. Magn Reson Med. 2015.

176. Lutti A, Dick F, Sereno MI, et al. Using high-resolution quantitative mapping of R1 as an index of cortical myelination. Neuroimage. 2014; 93: 176-188.

177. Baudrexel S, Nurnberger L, Rub U, et al. Quantitative mapping of T1 and T2* discloses nigral and brainstem pathology in early Parkinson's disease. Neuroimage. 2010; 51: 512-520.

178. Salerno M, Kramer CM. Advances in parametric mapping with CMR imaging. JACC Cardiovasc Imaging. 2013; 6: 806-822.

179. Stikov N, Boudreau M, Levesque IR, et al. On the accuracy of T1 mapping: searching for common ground. Magn Reson Med. 2015; 73: 514-522.

180. Fram EK, Herfkens RJ, Johnson GA, et al. Rapid calculation of T1 using variable flip angle gradient refocused imaging. Magn Reson Imaging. 1987; 5: 201-208.

181. Hurley SA, Yarnykh VL, Johnson KM, et al. Simultaneous variable flip angle-actual flip angle imaging method for improved accuracy and precision of three-dimensional T1 and B1 measurements. Magn Reson Med. 2012; 68: 54-64.

182. Heule R, Ganter C, Bieri O. Variable flip angle T1 mapping in the human brain with reduced T2 sensitivity using fast radiofrequency-spoiled gradient echo imaging. Magn Reson Med. 2015.

183. Wang HZ, Riederer SJ, Lee JN. Optimizing the precision in T1 relaxation estimation using limited flip angles. Magn Reson Med. 1987; 5: 399-416.

184. Imran J, Langevin F, Saint-Jalmes H. Two-point method for T1 estimation with optimized gradient-echo sequence. Magn Reson Imaging. 1999; 17: 1347-1356.

185. Deoni SC, Peters TM, Rutt BK. Determination of optimal angles for variable nutation proton magnetic spin-lattice, T1, and spin-spin, T2, relaxation times measurement. Magn Reson Med. 2004; 51: 194-199.

186. Cheng HL, Wright GA. Rapid high-resolution T(1) mapping by variable flip angles: accurate and precise measurements in the presence of radiofrequency field inhomogeneity. Magn Reson Med. 2006; 55: 566-574.

187. Schabel MC, Morrell GR. Uncertainty in T(1) mapping using the variable flip angle method with two flip angles. Phys Med Biol. 2009; 54: N1-8.

188. Samsonov A, Alexander AL, Jung Y, et al. Practical optimum experimental designs for fast T1 relaxometry with SPGR sequences. Proc Intl Soc Mag Reson Med. 2008; 16.

189. Koay CG, Chang LC, Denoi S, et al. An optimal framework for T1 estimation in an SPGR acquisition. Joint Annual Meeting ISMRM-ESMRMB. Berlin, Germany; 2007. p. 360.

190. Koay CG, Chang LC, Pierpaoli C, et al. Error propagation framework for diffusion tensor imaging via diffusion tensor representations. IEEE Trans Med Imaging. 2007; 26: 1017-1034.

191. Wood TC. Improved formulas for the two optimum VFA flip-angles. Magn Reson Med. 2015.

192. Marquardt DW. An algorithm for least-squares estimation of nonlinear parameters. J Soc Ind Appl Math. 1963; 11: 431-441.

193. Smith SM. Fast robust automated brain extraction. Hum Brain Mapp. 2002; 17: 143-155.

194. Liu F, Chaudhary R, Hurley SA, et al. Rapid multicomponent T2 analysis of the articular cartilage of the human knee joint at 3.0T. J Magn Reson Imaging. 2014; 39: 1191-1197.

195. Pineda FD, Medved M, Fan X, et al. B and T mapping of the breast with a reference tissue method. Magn Reson Med. 2015.

196. Nelson TJ, Martinez-Fernandez A, Yamada S, et al. Induced pluripotent reprogramming from promiscuous human stemness related factors. Clin Transl Sci. 2009; 2: 118-126.

197. Deming DA, Maher ME, Leystra AA, et al. Phospholipid Ether Analogs for the Detection of Colorectal Tumors. PLoS ONE. 2014; 9: e109668.

198. Stummer W, Pichlmeier U, Meinel T, et al. Fluorescence-guided surgery with 5-aminolevulinic acid for resection of malignant glioma: a randomised controlled multicentre phase III trial. The Lancet Oncology. 2006; 7: 392-401.

199. Zhou Z, Lu ZR. Gadolinium-based contrast agents for magnetic resonance cancer imaging. Wiley Interdiscip Rev Nanomed Nanobiotechnol. 2013; 5: 1-18.

200. Shih JL, Brugger RM. Gadolinium as a neutron capture therapy agent. Med Phys. 1992; 19: 733-744.

201. Clark PA, Iida M, Treisman DM, et al. Activation of multiple ERBB family receptors mediates glioblastoma cancer stem-like cell resistance to EGFR-targeted inhibition. Neoplasia. 2012; 14: 420-428.

202. Zhou Z, Han Z, Lu ZR. A targeted nanoglobular contrast agent from host-guest self-assembly for MR cancer molecular imaging. Biomaterials. 2016; 85: 168-179.

Appendix 1: List of abbreviations and shorthand terms

A549: human non-small cell lung cancer cell line
ALS: amyotrophic lateral sclerosis
AP: anterior-posterior
APC: alkylphosphocholine analog
BLI: bioluminescence imaging
CA: carrier added (bulk tracer added to positron-emitting tracer)
Ca^{2+}: divalent calcium
Cd^{2+}: divalent cadmium
CEST: chemical exchange saturation transfer
CLR-1404: cancer-targeted chemotherapy agent based on NM-404 technology
CLR-1502: cancer-targeted optical imaging agent based on NM-404 technology
CNS: central nervous system
Co^{2+}: divalent cobalt
CT: computed tomography
DMEM: Dulbecco's modified Eagle's medium
(h)DMT1: (human) divalent metal transporter 1
DAPI: 4',6-diamidino-2-phenylindole
DCE-MRI: dynamic contrast-enhanced MRI
DV: dorsal-ventral
EGF: epidermal growth factor
EPR: enhanced permeability and retention
ex vivo: in tissue; following experimentation on and sacrifice of a living subject
^{18}F: positron-emitting isotope of fluorine
^{19}F: MR active isotope of fluorine
FA: flip angle
FDG: fluorodeoxyglucose
Fe^{2+}: divalent iron
FGF: fibroblast growth factor
FLIRT: FMRIB's Linear Image Registration Tool
fLuc: firefly luciferase enzyme
FOV: field of view
G010: line of hNPC used in this work
Gd: gadolinium (generic)
Gd^{3+}: trivalent gadolinium
Gd-DO3A-404:
(h)GFAP: (human) glial fibrillary acidic protein
HD: Huntington's disease
hNPC: human neural progenitor cells
hNPC-DMT1: hNPC transiently over-expressing DMT1
$hNPC^{DMT1}$: hNPC stably over-expressing DMT1
$hNPC^{DMT1\text{-}1}$: hNPC stably over-expressing DMT1 after infection with LV-DMT1-CS

$hNPC^{DMT1-2}$: hNPC stably over-expressing DMT1 after infection with LV-DMT1-Imanis
hNPC-WT: wild-type hNPC used as controls for hNPC-DMT1
$hNPC^{WT}$: wild-type hNPC used as controls for $hNPC^{DMT1}$
HSV1-tk: herpes simplex virus 1 thymidine kinase
%ID/g: percent injected dose per gram
i.p.: intraperitoneal
in vitro: in living cell/tissue culture
in vivo: in a living subject
LIF: leukemia inhibitory growth factor
LV: lentivirus
LV-DMT1-CS: DMT1 lentivirus prepared at Cedars-Sinai
LV-DMT1-Imanis: DMT1 lentivirus prepared by Imanis Life Sciences
M_0: equilibrium magnetization
MEMRI: manganese-enhanced MRI
ML: medial-lateral
Mn: manganese (generic)
Mn-DPDP: mangafodipir trisodium
Mn^{2+}: divalent manganese
$MnCl_2$: manganese chloride
^{52}Mn: positron-emitting isotope of Mn
MOI: multiplicity of infection
MR: magnetic resonance
MRI: magnetic resonance imaging
NaCl: sodium chloride
NCA: no carrier added (no bulk tracer added to positron-emitting tracer)
NEX: number of excitations
Ni^{2+}: divalent nickel
NIS: sodium iodide symporter
NDS: normal donkey serum
NLS: nonlinear least squares
NM-404: phospholipid ether analog for cancer-targeted PET imaging after labeling with ^{124}I
OSEM: ordered subset expectation maximization
PBS: phosphate-buffered saline
PCR: polymerase chain reaction
PD: Parkinson's disease
PET: positron emission tomography
PET/CT: combined PET and computed tomography
PET/MRI: combined PET and MRI
PFA: paraformaldehyde
PLE: phospholipid ether
PSA: penicillin/streptomycin/amphotericin
PolyHEMA: poly-2-hydroxyethyl methacrylate
PSA: peniciliin/streptomycin/amphotericin
QMAP: quantitative MRI analysis package

R_1: spin-lattice/longitudinal relaxation rate
r_1: longitudinal relaxivity (s^{-1}/mM)
R_2: spin-spin/transverse relaxation rate
r_2: transverse relaxivity (s^{-1}/mM)
RF: radiofrequency
RMSE: root mean squared error
ROI: region of interest
RPM: rotations per minute
RT: room temperature
SFFV: spleen focus-forming virus promoter
SNR: signal-to-noise ratio
SPECT: single photon emission computed tomography
SPIO: super-paramagnetic iron oxide (nanoparticles)
SPGR: spoiled gradient echo
SV: shuttle vector
T_1: spin-lattice/longitudinal relaxation time
T_2: spin-spin/transverse relaxation time
TE: echo time
TOA: trioctylamine
TR: repetition time
US: ultrasound
U87: human glioblastoma cell line
VFA: variable flip angle
WT: wild-type, not modified or engineered
Zn^{2+}: divalent zinc
^{89}Zr: positron-emitting isotope of zirconium

Appendix 2: Derivation of the determinant of $\boldsymbol{J}_{\gamma}^{T}(\boldsymbol{r})\boldsymbol{J}_{\gamma}(\boldsymbol{r})$

From Eq. 7-8, the Jacobian matrix can be written as

$$\boldsymbol{J}_{\gamma}(\boldsymbol{r}) = \begin{bmatrix} {\partial r_1}/{\partial \gamma_1} & {\partial r_1}/{\partial \gamma_2} \\ \vdots & \vdots \\ {\partial r_n}/{\partial \gamma_1} & {\partial r_n}/{\partial \gamma_2} \end{bmatrix}$$

where ${\partial r_i}/{\partial \gamma_1} \equiv {\partial r_i}/{\partial M_0}$ and ${\partial r_i}/{\partial \gamma_2} \equiv {\partial r_i}/{\partial T_1}$. Therefore,

$$\boldsymbol{J}_{\gamma}^{T}(\boldsymbol{r})\boldsymbol{J}_{\gamma}(\boldsymbol{r}) = \begin{bmatrix} \sum_{i=1}^{n} (\partial r_i/\partial \gamma_1)^2 & \sum_{i=1}^{n} (\partial r_i/\partial \gamma_1)\,(\partial r_i/\partial \gamma_2) \\ \sum_{i=1}^{n} (\partial r_i/\partial \gamma_1)\,(\partial r_i/\partial \gamma_2) & \sum_{i=1}^{n} (\partial r_i/\partial \gamma_2)^2 \end{bmatrix}$$

By defining $E = \exp\,(TR/T_1)$, Eq. 7-8 can be rewritten as follows:

$$\frac{\partial r_i}{\partial \gamma_1} = \frac{(1-E)\sin\,(\alpha_i)}{E - \cos\,(\alpha_i)}$$

and

$$\frac{\partial r_i}{\partial \gamma_2} = \frac{M_0 \cdot TR \cdot E(1-\cos(\alpha_i))\sin\,(\alpha_i)}{T_1^2 (E - \cos\,(\alpha_i))^2}$$

so that

$$\left(\frac{\partial r_i}{\partial \gamma_1}\right)^2 = \frac{(1-E)^2 \sin^2(\alpha_i)}{(E - \cos\,(\alpha_i))^2}$$

$$\left(\frac{\partial r_i}{\partial \gamma_2}\right)^2 = \frac{M_0^2 TR^2 E^2 (1-\cos\,(\alpha_i))^2 \sin^2(\alpha_i)}{T_1^4 (E - \cos\,(\alpha_i))^4}$$

and

$$\left(\frac{\partial r_i}{\partial \gamma_1}\right)\left(\frac{\partial r_i}{\partial \gamma_2}\right) = \frac{M_0 \cdot TR \cdot E(1-E)(1-\cos(\alpha_i))\sin^2(\alpha_i)}{T_1^2 (E - \cos\,(\alpha_i))^3}$$

The determinant of $\boldsymbol{J}_{\gamma}^{T}(\boldsymbol{r})\boldsymbol{J}_{\gamma}(\boldsymbol{r})$ can then be written as a double summation:

$$\det\left(\boldsymbol{J}_{\gamma}^{\boldsymbol{T}}(\boldsymbol{r})\boldsymbol{J}_{\gamma}(\boldsymbol{r})\right)$$

$$= \left(\sum_{i=1}^{n}(\partial r_i/\partial\gamma_1)^2\right)\left(\sum_{i=1}^{n}(\partial r_i/\partial\gamma_2)^2\right)$$

$$-\left(\sum_{i=1}^{n}(\partial r_i/\partial\gamma_1)\,(\partial r_i/\partial\gamma_2)\right)\left(\sum_{i=1}^{n}(\partial r_i/\partial\gamma_1)\,(\partial r_i/\partial\gamma_2)\right)$$

$$= \sum_{i=1}^{n}\sum_{j=1}^{n}(\partial r_i/\partial\gamma_1)^2\left(\partial r_j/\partial\gamma_2\right)^2 - (\partial r_i/\partial\gamma_1)(\partial r_i/\partial\gamma_2)(\partial r_j/\partial\gamma_1)(\partial r_j/\partial\gamma_2)$$

$$= \frac{M_0^2TR^2E^2(1-E)^2}{T_1^4}\sum_{i=1}^{n}\sum_{j=1}^{n}\left(\frac{\sin^2(\alpha_i)\sin^2(\alpha_j)\,(1-\cos\,(\alpha_j))^2}{(E-\cos(\alpha_j))^4(E-\cos(\alpha_i))^2}\right.$$

$$\left.-\frac{\sin^2(\alpha_i)\sin^2(\alpha_j)\,(1-\cos\,(\alpha_i))(1-\cos\,(\alpha_j))}{(E-\cos(\alpha_j))^3(E-\cos(\alpha_i))^3}\right)$$

$$= \frac{M_0^2TR^2E^2(1-E)^2}{T_1^4}\sum_{i=1}^{n}\sum_{j=1}^{n}\frac{\sin^2(\alpha_i)\sin^2(\alpha_j)\,(1-\cos\,(\alpha_j))}{(E-\cos(\alpha_j))^4(E-\cos(\alpha_i))^3}\{(1-\cos(\alpha_j))(E$$

$$-\cos(\alpha_i)) - (E-\cos(\alpha_j))(1-\cos\,(\alpha_i))\}$$

$$= \frac{M_0^2TR^2E^2(1-E)^2}{T_1^4}\sum_{i=1}^{n}\sum_{j=1}^{n}\frac{\sin^2(\alpha_i)\sin^2(\alpha_j)\,(1-\cos\,(\alpha_j))}{(E-\cos(\alpha_j))^4(E-\cos(\alpha_i))^3}\{(1-E)(\cos(\alpha_j)$$

$$-\cos\,(\alpha_i))\}$$

$$= \frac{M_0^2TR^2E^2(1-E)^3}{T_1^4}\sum_{i=1}^{n}\sum_{j=1}^{n}\frac{\sin^2(\alpha_i)\sin^2(\alpha_j)\,(1-\cos\,(\alpha_j))(\cos(\alpha_j)-\cos\,(\alpha_i))}{(E-\cos(\alpha_j))^4(E-\cos(\alpha_i))^3}$$

Once the determinant of $\boldsymbol{J}_{\gamma}^{\boldsymbol{T}}(\boldsymbol{r})\boldsymbol{J}_{\gamma}(\boldsymbol{r})$ is obtained, the covariance matrix can be computed quite easily; therefore, the derivation will not be shown here.